

**HIERARCHICAL STATISTICAL MODELING OF RATES AND
VARIABILITY OF SEA LEVEL**

BY ERICA L. ASHE

**A dissertation submitted to the
School of Graduate Studies
Rutgers, The State University of New Jersey
in partial fulfillment of the requirements
for the degree of
Doctor of Philosophy
Graduate Program in Statistics and Biostatistics**

Written under the direction of

Robert E. Kopp

and approved by

New Brunswick, New Jersey

May 2018

ABSTRACT OF THE DISSERTATION

HIERARCHICAL STATISTICAL MODELING OF RATES AND VARIABILITY OF SEA LEVEL

by Erica L. Ashe

Dissertation Director: Robert E. Kopp

Climate change is driving sea-level change around the world. Understanding the physical mechanisms behind global and regional sea-level variations requires historical reconstructions. Prior to the instrumental period – over which tide gauges, beginning about 2-3 centuries ago, and satellites, over the last three decades, record relative sea level (RSL) and sea-surface height (SSH), respectively – the sea-level record depends upon proxy-based reconstructions. Proxy data contain vertical and temporal uncertainties that create challenges to modeling paleo-sea levels. One specific problem in interpreting these proxy data is parsing the complex spatial and temporal patterns of RSL and its rates of change from sparse data of different resolutions from distinct locations and sources. Another challenge is accounting for known uncertainties in a consistent and realistic manner. Making use of data that do not adhere to normality assumptions poses additional challenges to models of RSL.

This dissertation employs several methods to handle these challenges in order to quantify past rates of RSL change probabilistically. Hierarchical models are central to model clarity. They explicitly distinguish between a process level, which characterizes the spatio-temporal sea-level field, and a data level, which characterizes the way in which sparse proxy data and noise are recorded. A parameter level depicts prior expectations about the structure of variability in the spatio-temporal field.

Many past statistical models have not included a spatial component; here, we demonstrate methods for incorporating sparse data from disparate locations that share information over space and time through covariance functions that describe Gaussian process (GP) priors in spatio-temporal empirical hierarchical models (STEHMs). An analysis of several techniques recently implemented in the literature with both instrumental and proxy data illustrates the transparency and flexibility of hierarchical statistical modeling frameworks for sea-level studies. Non-parametric methods, such as the Kalman smoother and hierarchical models with GP priors, incorporate physical prior information into the process levels and provide flexible and robust ways to model the spatio-temporal RSL field and GMSL. Empirical Bayesian analyses provide a good approximation for large datasets and require fewer computational resources than fully Bayesian analyses; conversely, fully Bayesian analyses include parameter uncertainties to more thoroughly characterize known uncertainties.

Whereas past models frequently assumed Gaussian uncertainties in RSL proxy data, or excluded data that cannot be approximated with a normal distribution, this dissertation presents an approach, within a Bayesian hierarchical framework with GP priors, that incorporates non-Gaussian uncertainties through Markov Chain Monte Carlo (MCMC) sampling. This approach readily accommodates parametric and non-parametric likelihood distributions; in our case study of south Florida coral and sedimentary archives, non-parametric likelihoods are more robust to geographical distribution differences. Incorporating non-Gaussian likelihoods allows the inclusion of a variety of coral taxa with distinct empirical depth distributions, as illustrated here, as well as many other types of RSL proxy data that have previously been excluded or estimated improperly.

We also introduce a new method of modeling high-resolution proxy data, and illustrate it using mid-Holocene sites in Southeast Asia. This approach incorporates a periodic process term in the modeling, based on analysis of the modern processes, as well as methods for optimizing temporal shifts due to age uncertainties. It reveals ~ 0.6 m fluctuations in RSL, as well as a peak rate of RSL rise of 9.6 ± 4.2 mm/yr and a peak rate of RSL fall of 12.6 ± 4.2 mm/yr. These fluctuations may have been driven by dynamic, steric, or eustatic effects, and they are unprecedented in the region in modern times. . Although each dataset has unique characteristics, this method can be extended to other high-resolution proxy records of RSL around the globe.

Acknowledgements

I have numerous friends, colleagues, and educators to thank, without whom I would not be submitting this dissertation (with 99.999% probability). I owe so much to my advisor, Dr. Robert Kopp, who is absolutely brilliant and an inspiration in many ways. Bob has dedicated countless hours to my education and training. He has known when to step in to assist me and when to step back to let me struggle toward knowledge and confidence. His comments, critiques, revisions, support, and insight have challenged me to think and write as a scientist. I thought I was a grammarian before I received edits from Bob, and his attention to detail in this and so many things is impeccable. Even as his time has become more precious with his increasing success and obligations, he has never shorted me on time or attention. I would have given up before even beginning my research without Bob's support, academically, personally, and professionally.

Dr. Ben Horton has encouraged me from the day we met. He introduced me to many collaborators, in addition to being a pleasure to work with, himself. His expertise and support have been indispensable. Dr. Harold Sackrowitz seemed to have confidence in me when I could not think of a single reason for it. His ability as an educator, his patience, and his kindness are admirable. I hope to be half the teacher that he has been to me. I would never have begun at Rutgers if not for Dr. John Kolassa. His support, sincere concern, and advocacy have not wavered since I met him. Dr. Kolassa puts others before himself; he is generous with his time, his thoughts, and his experience. He has helped me to solve non-academic problems that seemed insurmountable, and I cannot imagine being where I am without him. Dr. Tami Carpenter was always more than just my fellowship advisor. She made herself available for advice on many other subjects, as well. She helped me find solutions to several obstacles I encountered at Rutgers, in addition to introducing me to my advisor, encouraging my research interests, and helping me navigate summer internships. Tami was always there, without judgment or hesitation.

In addition to being an incredible mentor, I gained a close friend and confidant in Dr. Nicole

Khan. She was a pleasure to work with from our first meeting, and she has become a part of my life. From project collaborations to work and personal advice, her insight and knowledge have been invaluable. I owe her so much. She also introduced me to an additional collaborator, Dr. Lauren Toth, who has become more than just a colleague, but also a friend. Together, these two have supported me in my research and emotionally. They make me laugh and inspire me.

I began my statistics journey long before Rutgers: way back in undergraduate school at University of Kansas, where my sister's example led me to become a statistics teaching assistant. Aside from Rachel leading me into the world of statistics, she has always believed in me. She has confidence in my abilities when I have none, and her knowledge that I would succeed in completing my doctorate helped me to believe in myself. The support I received at Baruch led me to pursue my PhD, and for that I have to thank Dr. Shulamith Gross, Dr. Arie Harel, and Dr. Lawrence Tatum. They gave me a foundation in graduate statistics as well as faith in my ability to continue further with my studies. Dr. Ann Brandwein has also been an unwavering supporter, encouraging me to persevere and checking in on my progress.

Thank you to my supportive, amazing friends, who have seen my moods swing with my work, but have not ditched me, who have made me laugh and let me cry. I am especially grateful for the friendship of Christine Swedowsky, Jenn Kantor, Elyse Britton, Eric Havlik, Zoe Allen, Hecker, Matt Polacheck, and Laura Kavanaugh. I cannot imagine getting through this without you people. You have listened to me gripe, made fun of my nerdiness, and loved and supported me through it all.

My mom and dad, and my family, David, Baila, and Gavin, have never understood what I do or why I do it, but that never stopped them from believing in me. I could have made them proud without this, and maybe it would have been less stressful and easier. We quite possibly could have been happier, but they knew I would not quit, even when I thought I would, and that is all the difference. Thanks for putting up with me, even when I am at my worst. And more importantly, thanks for loving me in spite of it all.

And finally, to my husband, who is my perfect. I am sorry for putting you through hell. I love you, and you make me a better person (almost) every day. Thanks for always being on my side (even if I am wrong), for your support in every way, for your never-ending patience, and for the

kids and the beer. I appreciate you.

The chapters of this dissertation were collaborative works with many people.

Chapter 2: This chapter was co-authored with Niamh Cahill, Carling Hay, Nicole Khan, Andrew Kemp, Simon Engelhart, Benjamin P. Horton, Andrew Parnell, and Robert E. Kopp. We thank HOLSEA (Geographic Variability Of Holocene Relative Sea Level) and PALSEA2 (Paleo-Constraints on Sea-Level Rise), which are INQUA (International Union for Quaternary Research) working groups as well as the PAGES (Past Global Changes) project. It was supported by NSF grants OCE-1458921, OCE-1458903, OCE-1458904, OCE-1458904 and OCE-1702587.

Chapter 3: This chapter was co-authored with Nicole Khan, Lauren Toth, Andrea Dutton, and Robert E. Kopp. We thank Ben Horton for comments and discussions. It was supported by NSF grants OCE-1702587 and OCE-1702740, Nicole Khan and Lauren Toth by the Coastal and Marine Geology and Land Change Science programs of the U.S. Geological Survey. Any use of trade names herein was for descriptive purposes only and does not imply endorsement by the U.S. Government.

Chapter 4: This chapter was co-authored with Aron Meltzner, Adam Switzer, Benjamin P. Horton, Qiang Qiu, David F. Hill, Sarah L. Bradley, Robert E. Kopp, Emma M. Hill, Jędrzej M. Majewski, Danny H. Natawidjaja, and Bambang W. Suwargadi. It is an edited abridgment of Meltzner et al., 2017, which appeared in Nature Communications. We thank A.D. Hawkes, D. Prayudi and I. Suprihanto for field support; A. Ritch, G. Lee, and B. Jonnalagadda for slab analysis; D.T. Pham and D. Warrick for tide analysis; J. Pile and K.E. Bradley for GIS assistance; K. Sieh for early discussions; M. Sim and C. Prior for discussions on radiocarbon dating; and A. Thomas for reviews. Primary funding for this work came from the National Research Foundation Singapore and the Singapore Ministry of Education under the Research Centres of Excellence initiative. This research was also partially supported by the National Research Foundation Singapore under its Singapore NRF Fellowship scheme (award numbers NRF-RF2010-04 and NRF-NRFF2010-064, NSF ARC-1203415 and OCE-1458904 as well as by the Netherlands Earth System Science Centre (NESSC), which is financially supported by the Ministry of Education, Culture and Science (OCW).

Table of Contents

Abstract	ii
Acknowledgements	iv
1. Introduction	1
Global mean sea level (GMSL)	2
Static equilibrium	3
Dynamic sea level (DSL)	4
Glacial isostatic adjustment (GIA)	5
Dissertation organization	6
Additional Contributions	7
2. Statistical modeling of rates and trends in Holocene sea level	10
2.1. Introduction	10
2.2. Sea-level processes and data	12
2.2.1. Sea-level processes	12
2.2.2. Sea-level data	13
2.3. Hierarchical statistical model framework	14
2.3.1. Definition of relevant notation for hierarchical statistical framework	15
2.3.2. Analysis & modeling choices	16
2.4. Implementing the data level	16
2.5. Modeling the temporal sea-level process	19
2.5.1. Temporally linear models	19
2.5.2. Change-point models	20
2.5.3. Gaussian process models	21

2.6.	Modeling the spatio-temporal sea-level process	23
2.6.1.	RSL represented with single or multiple GP priors	24
2.6.2.	Empirical orthogonal functions	25
2.6.3.	Incorporating physics-based models	25
2.7.	Analysis choices	26
2.7.1.	Least squares	27
2.7.2.	Ad hoc approaches: regional averaging, virtual stations, pre-processing	27
2.7.3.	Empirical Bayesian analysis	29
2.7.4.	Fully Bayesian analysis	30
2.7.5.	Kalman smoother techniques	31
2.8.	Illustrative analyses	31
2.8.1.	Estimating rates of RSL change from continuous cores (Common Era to present)	32
	Models and implementations	32
	Results and discussion of temporal models during the Common Era from continuous cores	33
2.8.2.	Characterizing spatial and temporal variability in RSL change from proxy data (Holocene to present)	37
	Models and implementations	38
	Results and discussion of empirical spatio-temporal GP (EST-GP) and temporal- only Bayesian EIV-IGP models for full Holocene	38
2.8.3.	Estimating spatio-temporal RSL and GMSL from instrumental data (1900 to present)	41
	Models and implementations	41
	Results and discussion of KS and EST-GP from 1900 to present	42
2.9.	Conclusions	44
2.10.	Glossary	47
3.	A statistical framework for integrating non-Gaussian proxy distributions into geological reconstructions of relative sea level	51

3.1. Introduction	51
3.2. Methods	53
3.2.1. Statistical model structure	55
Data level	56
Process level	59
Parameter level	59
3.2.2. Statistical model implementation	60
Distribution-fitting module	60
Sampling module	61
Sample-wise prediction module	61
3.2.3. Case study using Holocene data from south Florida	62
3.3. Results	63
3.3.1. Distributions of living Caribbean corals	63
3.3.2. Comparison of different proxy data and their interpretation in the model framework	64
3.4. Discussion	66
3.5. Conclusions	69
4. Half-meter sea-level fluctuations on centennial timescales from mid-Holocene corals of Southeast Asia	70
4.1. Introduction	70
4.2. Data	72
4.2.1. Chronological constraints and uncertainties	75
4.2.2. Vertical uncertainties of microatoll data	77
4.3. Statistical methods	79
4.3.1. Reinterpretation of published data from southern China	84
4.3.2. Model cross-validation	86
4.4. Results	87
4.4.1. Common signal	88

4.4.2. Site-specific offset between TKUB and TBAT	90
4.4.3. Comparison to distal records	90
4.5. Discussion	90
5. Conclusions and further work	93
Appendix A. Supplement to Chapter 2	95
A.1. Covariance functions	95
A.2. Analysis choice details	97
A.2.1. Regional averaging	97
A.2.2. Kalman smoother	97
A.3. Details of implementations	99
A.4. Data	99
Appendix B. Supplement to Chapter 3	101
B.1. Parametric distributions of living Caribbean corals	101
B.1.1. Local variability of coral distributions	101
B.1.2. Caribbean-wide coral depth distributions	102
B.1.3. Florida-specific depth distributions	103
B.2. Model implementation	103
B.2.1. Noisy-input Gaussian process (NIGP) method	103
B.2.2. Markov Chain Monte Carlo (MCMC) sampling	104
B.3. Results	106
B.4. Simulation and synthetic analysis	106
B.4.1. Synthetic tests	106
B.4.2. Synthetic data generation	108
B.4.3. Synthetic test results	109
B.5. Evaluation of proxy and model performance using synthetic data	109
B.6. Results and discussion of synthetic analyses	110
B.6.1. Sample size:	111

B.6.2. Percent Log-normal: 114

B.6.3. Normal uncertainty: 115

B.6.4. Log-normal uncertainty: 115

B.6.5. Evaluating the results of synthetic coverage ratios 116

B.6.6. Case study data 117

 Corals 117

 Sedimentary records 118

 Dating 118

 Measurement uncertainties 119

B.6.7. Discussion of biases 120

Chapter 1

Introduction

Around the globe, sea levels are rising at an accelerating rate, and this acceleration is likely to continue into the future (Church et al., 2013a). Rising sea levels are causing serious impacts, including increased flood risk, and will continue to do so even in the most optimistic projections. Understanding sea-level change in the past is vital to projecting future sea-level change, as it contextualizes current changes and constrains physics-based models of the processes used to project future changes.

Only a short history of sea-level data exists from the instrumental record. Since sea-level variations occur over a broad range of temporal and spatial scales, this short temporal record only provides so much insight into the mechanisms behind these variations. As a result, it is necessary to reconstruct sea level over longer time periods from sources that are proxies for sea level, which have both temporal and vertical uncertainty. This creates a non-trivial problem, particularly when the spatial field is brought into the picture. The paleo record from past periods can provide insight into the magnitude of change as well as the mechanisms that create this change, but only if analyzed objectively to arrive at estimates, with uncertainties, through space and time. Using spatio-temporal hierarchical models, it is possible to constrain the uncertainty in and reconstruct the entire relative sea level (RSL) field and its rates of change from such noisy data.

Many processes contribute to sea-level change at a given time and location, with variability on distinct temporal and spatial scales. Sea-surface height (SSH) is the height of the ocean above a known reference ellipsoid, while relative sea level (RSL) is the difference between the sea surface height and the height of the solid Earth. Global mean sea level (GMSL) is the average of RSL or SSH over the surface of the ocean. This dissertation focuses on RSL proxies that give insight into changes over time scales of thousands of years, for the period beginning with the Last Glacial Maximum (LGM), which occurred between 26 and 19 ka (e.g., Walker et al., 2009; Clark et al.,

2009; Milne et al., 2009; Khan et al., 2015), when ice sheets reached their greatest extent, sufficient to draw down global mean sea level by about 120 to 135 m (e.g., Clark and Mix, 2002). The last glacial period ended with the beginning of the current interglacial stage, the Holocene epoch (past ~11,700 years; Walker et al., 2009; Milne et al., 2009), also a prime focus period for paleo-sea level research. The Last Interglacial (LIG) stage, also known as marine isotope stage 5e (MIS5e) or the Eemian, occurred about 130,000 to 115,000 years ago (130 ka to 115 ka) and had peak global average surface temperatures comparable to, or slightly higher than, present levels (Hoffman et al., 2017); it is another period of primary interest for the paleo-sea level community.

Global mean sea level (GMSL)

GMSL changes occur due to changes in volume of the oceans or to alterations in the shape of the ocean basin, and thus to the relationship between volume and sea-surface height. Land-based ice sheets shrink (or grow), increasing (or decreasing) the mass and volume of water in the oceans. This is known as glacio-eustasy and occurs on hundred-meter scales over tens of thousands of years. Redistribution of water between different hydrological reservoirs, hydro-eustasy (Rovere et al., 2016), also alters the mass of the oceans, which could result in sea-level changes of meters over tens of thousands of years (Hay and Leslie, 1990). Ocean temperatures and salinity, thermohaline and halosteric changes, result in density, and therefore volume, changes of the ocean water (Church et al., 2013a). Global mean thermal expansion produces rates of sea-level change on meter scales over hundreds to thousands of years (and smaller variability over shorter time periods). In addition, continental movement and visco-elastic Earth deformation alter the boundaries of the oceans (van Andel, 1994; Mitrovica and Milne, 2003), which changes their capacity. Convective mantle flow drives vertical deflections of the crust, which causes alterations in bedrock elevation (Hays and Pitman, 1973). This geological process, known as mantle dynamic topography (Braun, 2010), may affect sea levels on meter scales over hundreds of thousands of years (Austermann et al., 2017; Conrad and Husson, 2009). At active continental margins, tectonic plate movement also causes vertical and horizontal movement of ocean floors, which results in tectonic subsidence or uplift. Tectonics and sediment compaction may cause a few hundred meters of GMSL change in 10-100 million years (Flemming and Roberts, 1973). The combination of all of these processes influence

GMSL on a continuum of time scales, spanning years to hundreds of millions of years (Morrow, 2014), and could therefore be separated by their characteristic temporal scales or be estimated by physical process models.

Many analyses have concluded that GMSL has risen at rates between 1.6 and 1.9 mm/yr over the twentieth century (e.g., Holgate, 2007; Jevrejeva et al., 2008; Church and White, 2011; Church et al., 2013a), whereas Hay et al. (2015) and Dangendorf et al. (2017) estimate the rate of rise prior to 1990 averaging 1.2 ± 0.2 and 1.1 ± 0.3 mm/yr, respectively, increasing to an average 3.0 ± 0.7 and 3.1 ± 1.4 mm/yr, respectively after 1993. GMSL levels have varied during the Common Era (Kopp et al., 2016) and the last deglaciation. Dutton and Lambeck (2012) estimated GMSL peaked between 5.5 and 9 m higher than present, and Kopp et al. (2009) concluded (with 67% probability) that GMSL exceeded 8 m higher than present.

Static equilibrium

Several underlying processes affect sea level on various time scales as mass is redistributed across the surface of the Earth due to changes in the dispersment of ice and water. Static equilibrium sea-level change refers to the unique pattern of sea level that is produced as a close-to-instantaneous response to melting of land ice (Kopp et al., 2015a). The sea-level response created by gravitational, rotational, and deformational changes on these time-scales is also sometimes called ‘contemporary GRD.’ The diminished direct gravitational pull of a shrinking ice sheet results in RSL fall in its vicinity (the near-field) as water migrates away from the ice sheet, resulting in changes in the geoid (the hypothetical shape of an equipotential surface, if the oceans and atmosphere were in equilibrium). RSL rise is enhanced in the far-field of the melting ice, due to the migration of water from the near-field. The weight exerted on the earth by an ice mass causes elastic deformation of the lithosphere, which is the rigid outer part of the earth, comprising the crust and upper mantle. As ice sheets melt, mass is redistributed to oceans, resulting in crustal uplift from the unloading. As well as producing changes in the geoid, redistribution of mass changes the orientation and rate of rotation of the Earth (Kopp et al., 2015a; Mitrovica and Milne, 2003). The unique patterns of sea-level change produced by static-equilibrium processes have come to be known as sea-level “fingerprints.” On the border of a melting ice sheet, RSL can fall at a rate many times greater

than the GMSL rise from the melt event, while far-field RSL rise can be as much as $\sim 30\%$ more than the global average (Mitrovica et al., 2001; Kopp et al., 2015a; Hay et al., 2014).

Dynamic sea level (DSL)

DSL changes are produced by a variety of processes, which can generally be separated into density-driven or mass-driven. Just as thermal expansion creates GMSL rise, density changes in ocean water result in regional differences in sea level. These changes, known as *steric effects*, refer to the way that salinity and temperature affect the expansion or contraction of water, and therefore ocean volume (Antonov et al., 2002): water expands with heat and the addition of fresh water, whereas it contracts as it becomes colder or saltier. Mass changes include the addition of freshwater and redistribution of water due to atmospheric forcing, buoyancy fluxes and ocean circulation, and occur on a range of spatial scales and temporal scales. Ocean currents are continuous and directed movements of ocean water (National Ocean and Atmospheric Administration, 2017), such as the Gulf Stream, and are affected by heat redistribution as well as wind patterns (Church et al., 2013a). Currents occur at various depths, locally and globally (National Ocean and Atmospheric Administration, 2017), and have a continuous effect on sea level. Coupled ocean-atmosphere systems, such as the El Niño Southern Oscillation (ENSO) and the Pacific Decadal Oscillation (PDO), and seasonal cycles affect sea levels seasonally to decadal and reflect different modes and spatial scales of variability. All of these dynamics, which result in distinct spatial patterns of SSH, vary regionally and on seasonal to multi-annual timescales. Additionally, static-equilibrium effects can amplify or reduce changes associated with water-mass redistribution, a process known as self-attraction and loading.

Recent studies have found that wind stress and buoyancy fluxes dominate small-scale geographic variability, while mass redistribution and barotropic adjustments influence larger-scale variability in DSL (Piecuch et al., 2013; Johnson and Chambers, 2013). Thermosteric effects contribute to DSL variability around the world, whereas halosteric effects drive variability closer to the poles (Fukumori and Wang, 2013; Rye et al., 2014; Kohl, 2014). Dominant modes characterize these changes over inter-annual times scales.

Glacial isostatic adjustment (GIA)

Driven by the flow of the mantle, GIA is the result of ongoing land and geoid changes, produced as a visco-elastic response (multi-centennial and longer time scales) to past melting of land-based ice sheets. The rebound of land that was previously depressed under glacial ice and the collapse of the forebulge on the perimeter of the former ice both continue for thousands of years after deglaciation (Farrell and Clark, 1976). Ocean syphoning, the process by which water migrates to the subsiding peripheral forebulge (Rovere et al., 2016), leads to a decrease in SSH in the far-field. Increases in water mass on continental shelves slowly produces a crustal tilt downwards, continental levering (Milne et al., 2009), which raises shorelines, resulting in ~ 0.5 mm/year of sea-level fall in some places (Kopp et al., 2015a).

GIA is a primary process affecting present-day observations of RSL, especially within ~ 3000 km of the center of previous glacial ice. Sea-level change from GIA varies geographically and is approximately linear over shorter time periods (< 3 ka), while over the Holocene (~ 12 ka), the form is non-linear. As an example, the Laurentide ice sheet, which covered most of Canada and the Northern US, disappeared between 6,000 and 9,000 years ago and continues to affect RSL on the east coast of Canada and the United States. In transitional zones, which occur at the margins of ice-sheets from the LGM (e.g., Massachusetts on the U.S. Atlantic coast), glacio-isostatic uplift was followed by subsidence from the migration of the forebulge (Quinlan and Beaumont, 1981). Some models estimate GIA contributing as much as 6 mm/yr to sea-level rise (at the forebulge of the Laurentide Ice Sheet) and 16 mm/yr to sea-level fall (e.g., in the Hudson Bay, the former core of the Laurentide Ice Sheet) regionally (Peltier, 2009).

Other processes

In addition to GIA, other processes, such as tectonics and sediment compaction, also cause vertical land movement (VLM). Tectonics are changes in the structure of the surface of the earth. Near active subduction zones, where collisions of tectonic plates (pieces of Earth's crust) occur, one plate may slip beneath another, causing either uplift or subsidence. Volcanically active regions may also experience abrupt changes in RSL locally. Conversely, passive margin environments (e.g., the Bahamas) are slowly subsiding due to tectonics. Long-term average tectonic subsidence or uplift

rate estimates, since the Last Interglacial at sites included in the analysis of Kopp et al. (2009), range from 1-2 cm/ky (kiloyear) to as much as 28 cm/ky (Kopp et al., 2009), and these effects are a primary cause of RSL change in some regions more recently (e.g., Holocene or century time scales, Shennan and Woodworth, 1992; Rovere et al., 2016). Sediment compaction, which results both from natural loading and from anthropogenic groundwater and hydrocarbon withdrawal (Brain et al., 2015), produces a local rise in sea level, especially in deltas, in some areas contributing more than ~ 9 mm/yr (e.g., Grand Isle, LA; Törnqvist et al., 2015 with characteristic timescales of variability that vary from inter-annual for human-driven processes to millennia for natural loading).

Dissertation organization

This dissertation is divided into three main parts. Chapter 2 reviews the current analytical and modeling choices available in sea-level modeling. Statistical models using instrumental and geological RSL proxy data require consistent and objective methods to comprehensively quantify multiple sources of uncertainty. Although statistical methods have played a major role in reconstructing other paleoclimate variables, such as temperature (e.g., Visser and Molenaar, 1988; Fritts, 1991; Smith et al., 1996; Mann et al., 1998; Dirren and Hakim, 2005; Haslett et al., 2006; Briffa et al., 2008), their application for both instrumental sea level (e.g., Church and White, 2004; Jevrejeva et al., 2006; Hay et al., 2013; Kopp, 2013) and for paleo-sea level (e.g., Parnell, 2005; Kopp et al., 2009; Cahill et al., 2016; Khan et al., 2015) is more recent. Tingley et al. (2012) formalized the spatio-temporal paleo-climate reconstruction problem and unified past innovations in modeling within a hierarchical framework. Similarly, this chapter provides a qualitative background for the formal statistical developments, including hierarchical models, with respect to the reconstruction of sea-level time series and spatio-temporal fields. We define different models representing the data-generation process by which RSL is transformed into a sea-level proxy observation. We describe time-series models for representing RSL at a single site and spatio-temporal models for representing the temporal evolution of sea-level across a regional or global domain. We compare and contrast linear, change-point, Gaussian process, and Kalman Smoother models through their application to common datasets that include tide gauges, continuous cores, and discrete index points at sites along the Atlantic coast of the United States.

Chapter 3 introduces a new statistical framework to estimate past sea-level change using modern depth distributions of individual coral taxa, incorporating non-Gaussian likelihoods of sea-level proxy elevations. Using Gaussian process (GP) priors, we use MCMC sampling to approximate these likelihoods in order to estimate the posterior distribution of sea level over time. We evaluate model performance for an illustrative Holocene dataset of coral and sedimentary proxies from south Florida. This analysis highlights differences in model results from trade-offs between quantity, precision, and temporal distribution of the data within the model, developing robust multi-proxy models of relative sea level.

Chapter 4 introduces new analyses within the hierarchical statistical framework. A process that can affect high-precision proxy sea-level data is the 18.61-year nodal tidal cycle. This chapter presents an innovative technique to incorporate this process and limiting data (which places an upper or lower bound on RSL) into a model of RSL. High-resolution proxy data from coral microatolls in East and Southeast Asia had previously seen limited use in RSL reconstructions. At the data level in our EHM, we simulated coral growth using maximum coral growth rates with various amounts of interannual sea-level variability, using a periodic sinusoidal term for the tidal cycles. We fit the results of the simulations to a GP with a periodic component, and used the optimal GP (with tuned maximum-likelihood parameters) within the EHM at the process level. Also at the data level, we account for three types of chronological uncertainty. Using relative ages of individual coral slabs, we optimize (within the calibrated radiocarbon age errors and localized marine reservoir correction, ΔR) age-shift parameters to maximize the likelihood of the EHM, given the data. Separating a non-linear component, periodic term, and site-specific offset at the process level, we produce probabilistic estimates of RSL change, finding previously unmodeled variability during this era. This section is an abridged variation of the original publication, Meltzner et al. (2017), which includes greater detail on the development of the coral microatoll proxy and the field and laboratory analyses.

Additional Contributions

I have employed numerous statistical techniques to expand and improve upon current methods. Each dataset is unique with uncertainties arising from different dominant processes. In some cases,

these processes are known and adjusted for in the data. In other cases, analytical and modeling choices must be made to appropriately characterize uncertainties.

I began my research applying spatio-temporal empirical hierarchical models (STEHMs) with GP priors to regional models of Holocene RSL in Khan et al. (2015). In that paper, we examined the range of Holocene RSL variability in locations representing a pole-to-pole transect across the Americas and Eurasia/Oceania. We described the spatial variability of RSL on a global scale, not previously done with these non-parametric techniques, revealing spatial and temporal changes caused by varying dominance of eustatic and isostatic factors over the Holocene.

Many sea-level modelers avoid data that may have been influenced by the process of sediment compaction or simply add additional uncertainty to the data. In Khan et al. (2017), I developed a STEHM with a novel method of accounting for sediment compaction through stratigraphic position (overburden thickness). Using GP priors, we conditioned on data that could not have been influenced by sediment compaction and calculated the residuals between predicted RSL and observed data that were likely influenced by compaction. We found a linear correlation between overburden thickness and these residuals, correcting with a shift and addition of bidirectional uncertainty for compacted data in the STEHM. The STEHM included basinal (uniform across the entire Caribbean basin), sub-basinal (exhibiting regional variability), and local (exhibiting little spatial correlation) signals as well as a term for high-frequency variability, and incorporated temporal uncertainty through the noisy input GP (NIGP) methods of McHutchon and Rasmussen (2011). We placed Matérn correlation GP priors on each term, and produced posterior probability distributions over time and space throughout the Caribbean.

In addition, I developed a simple model of the radiocarbon reservoir age correction (ΔR) variability in southern Florida in Toth et al. (2017). These values are critical for precise calibration of ages of marine samples, as evidenced by their use in multiple fields including RSL modeling (e.g., Meltzner et al., 2017). We found significant spatial influence of ΔR , which is used to date marine samples in reconstructions of oceanography and hydrology through the implementation of this STEHM.

In Vacchi et al. (in review), I constructed a STEHM to estimate magnitudes and rates of RSL

change (with associated uncertainty) throughout northeastern Canada. Within this implementation, I interpolated glacial isostatic adjustment (GIA) predictions from the physics-based model of Peltier et al. (2015) throughout the region. I used these predictions as the GP prior mean function in the STEHM by modeling the difference between the sea-level proxy observations and GIA.

Chapter 2

Statistical modeling of rates and trends in Holocene sea level

By Erica L. Ashe¹, Niamh Cahill², Carling Hay³, Nicole Khan⁴, Andrew Kemp⁵, Simon Engelhart⁶, Benjamin P. Horton⁴, Andrew Parnell⁷, and Robert E. Kopp¹

Rutgers University¹, University College Dublin², Boston College³, Nanyang Technological University⁴, Tufts University⁵, University of Rhode Island⁶

Abstract

Statistical modeling of relative sea-level (RSL) change has advanced considerably over the last decade. Formal statistical treatment of RSL data is necessary to consistently account for the uneven distribution of data in time and uncertainties in both time and elevation. Time-series models have adopted more flexible and physically informed specifications with better quantification of uncertainties. Spatio-temporal models have evolved from simple regional averaging to non-parametric, hierarchical frameworks that more richly represent the spatio-temporal correlation structure of sea level. The multiple solutions to both temporal and spatio-temporal analyses range from simple to complex, with more complex approaches enabling separation of the sea-level field into various components, the combination of geographically disparate data, and more rigorous quantification of spatial and temporal variability, even when data are sparse. This chapter reviews the range of statistical modeling and analytical choices, reformulating them in a common statistical hierarchical framework, which separates each model into different levels. The hierarchical framework clearly separates measurement and inferential uncertainty from process variability and highlights both the similarities and differences among choices. We illustrate the implications of analytical choices by comparing the results of their application to common datasets within a hierarchical framework. In any application, the type of data and the scientific question determine appropriate analytical and modeling choices. We make recommendations to use for temporal and spatio-temporal estimates of local, regional, and global scale trends from instrumental and geological proxy data.

2.1 Introduction

Relative sea level (RSL) exhibits complex spatial and temporal patterns arising from a range of underlying processes (e.g., Clark et al., 1978; Farrell and Clark, 1976; Peltier and Fairbanks, 2006; Shennan and Horton, 2002). Interpreting the rates and spatial patterns of RSL change, on timescales ranging from decades to millennia, often involves piecing together instrumental RSL

measurements spanning the past ~ 200 years and/or RSL proxy records that are sparse, noisy (with vertical and/or geochronological error), and unevenly distributed in time and space (e.g., Törnqvist et al., 2015; Piecuch et al., 2017). Statistical models allow RSL records to be fused in a consistent manner that allows rigorous quantification of multiple sources of uncertainty. Although statistical advancements have played a major role for decades in reconstructing other paleoclimate variables, such as temperature (e.g., Visser and Molenaar, 1988; Fritts, 1991; Smith et al., 1996; Mann et al., 1998), their application to both instrumental sea level (e.g., Church and White, 2004; Jevrejeva et al., 2006; Hay et al., 2013; Kopp, 2013), and for paleo RSL (e.g., Parnell, 2005; Kopp et al., 2009; Cahill et al., 2016; Khan et al., 2015), is more recent.

Advanced techniques are needed to answer fundamental questions in sea-level research, such as quantifying rates of RSL change (e.g., Cahill et al., 2015a; Khan et al., 2015), assessing geographic variability (e.g., Khan et al., 2017; Vacchi et al., in review), identifying the global-mean sea-level (GMSL) signal (e.g., Church and White, 2004; Jevrejeva et al., 2006; Kopp et al., 2009; Hay et al., 2015), and improving estimates of the contributions of dominant physical processes (e.g., Milne et al., 2005; Dangendorf et al., 2017; Kopp et al., 2014; Hay et al., 2015). Something these studies all have in common is the potential for use of a hierarchical statistical framework; we present such a framework, which permits a range of analysis choices (i.e., how to implement a model structure) and modeling choices (i.e., how to characterize the relationships between variables). Hierarchical models are flexible, can accommodate missing data, and are probabilistic, enabling probabilistic statements about sea level over time and space. The hierarchy divides the model into levels, enabling construction of the underlying space-time relationships in sea level (process level) separate from the relationship between the type of observation and sea level (data level) as well as a clear distinction between their uncertainties (Cressie and Wikle, 2015; Tingley et al., 2012). Using a hierarchical framework to present modeling choices in a parallel way, we highlight similarities and differences among these choices with an integrated perspective on the temporal and spatio-temporal analysis of RSL data. The appropriate model and analysis depends on the research question to be answered, the type of data being used, and the spatio-temporal scale (i.e., local to global, years to millennia) under consideration.

We briefly introduce sea-level processes and data, providing a qualitative background (Section

2.2) for the formal statistical developments of a hierarchical framework (Section 2.3). We then define different models representing the data-generation process (Section 2.4) by which RSL is transformed into a sea-level proxy record. We describe time-series models (Section 2.5) for representing RSL at a single site and spatio-temporal models (Section 2.6) for representing the temporal evolution of sea level across a regional or global domain. We discuss the advantages and disadvantages of using different analysis techniques (Section 2.7). We illustrate the similarities and differences between linear, change-point, Gaussian process, and Kalman Smoother models by applying these methods to case studies (Section 2.8) using datasets that include tide gauges, continuous core data, and index points at sites along the Atlantic coast of the United States. Finally, we make recommendations on which technique is appropriate to use based on the data being analyzed and the objective of the study (Section 2.9).

2.2 Sea-level processes and data

2.2.1 Sea-level processes

RSL is defined as the difference in elevation between sea-surface height (SSH) and the height of the solid Earth. Both RSL and SSH are typically averaged over a short period (e.g., years to decades to minimize the influence of the 18.6-year tidal cycle; Shennan et al., 2012). Global mean sea level (GMSL) is defined as the average of RSL or SSH over the surface of the ocean. Many processes contribute to sea-level change at a given time and location, with variability on distinct temporal and spatial scales.

GMSL changes occur due to changes in the volume and mass of water in the ocean or to alterations in the shape of the ocean basin, and thus to the relationship between volume and SSH. The processes affecting GMSL include glacio- and hydro-eustasy on hundred-meter and meter scales, respectively, over tens of thousands of years (e.g., Schwartz, 2005; Hay and Leslie, 1990), as well as steric changes (global mean thermal expansion) on meter scales over hundreds to thousands of years (and smaller scales over shorter periods) (Gornitz et al., 1982). Plate tectonic movement, which reshapes the ocean basins, may cause large-scale GMSL change over tens of millions of years (Flemming and Roberts, 1973), but the changes are negligible on time scales that are the focus of this thesis. These different processes influence GMSL on a continuum of time scales, spanning years

to hundreds of millions of years, and can therefore be partially separated by their characteristic temporal scales.

Regional sea-level changes occur due to several distinct processes (Kopp et al., 2015a). Dynamic sea level (DSL) causes distinct spatial patterns of SSH that vary regionally on seasonal to multi-annual timescales (e.g., Gill and Niller, 1973; Stammer et al., 2013). The unique patterns of short-term RSL change produced by static-equilibrium processes, which affect the Earth’s gravitational field, rotation, and lithosphere in response to changing distribution of water and ice mass at Earth’s surface, have come to be known as sea-level “fingerprints.” On the border of a melting ice sheet, RSL can fall at a rate greater than the associated GMSL rise, while far-field RSL rise can be as much as $\sim 30\%$ more than the global average (Farrell and Clark, 1976; Mitrovica and Milne, 2002; Mitrovica et al., 2011). Sea-level change from glacial isostatic adjustment (GIA) is the longer term response to mass redistribution between ice and water. GIA produces approximately linear trends over shorter time periods ($< 3\text{ka}$, e.g., Peltier et al., 2015) and non-linear trends over longer periods (i.e., throughout the Holocene $\sim 12\text{ka}$; Peltier et al., 2015). GIA is largest in the aftermath of a melt event and decays over time (e.g., Farrell and Clark, 1976; Mitrovica and Milne, 2003). Changes as a result of mantle dynamic topography (Hays and Pitman, 1973) affect RSL on meter scales over hundreds of thousands of years (Austermann et al., 2017; Braun, 2010). At a more localized scale, tectonics can drive both slow, steady RSL change (e.g., Vacchi et al., 2012) and abrupt, coseismic change (e.g., Shennan et al., 1996; Dura et al., 2016). Anthropogenic sediment compaction (which can vary interannually in response to fluctuations in groundwater withdrawal; Allison et al., 2016) and natural sediment compaction (which can vary on millennial time scales; Allison et al., 2016) can annually contribute millimeters to tens of millimeters in some deltaic regions (e.g., Grand Isle, LA; Törnqvist et al., 2015).

2.2.2 Sea-level data

Sea-level data include both direct observations of SSH via satellite altimetry and RSL by tide gauges and also indirect inferences of RSL from geological proxies. Direct observations of RSL from tide gauges, the oldest of which date to the 1700s (e.g., Van Veen, 1945; Woodworth, 1999), are available over the last 2-3 centuries. Tide gauges are restricted to coastal sites and measure

RSL with high resolution and small uncertainties. Modern, quality-controlled measurements from Northern Hemisphere sites are available from the early-to-mid 19th century onward and globally from the mid 20th century onward (PSMSL, 2017; Holgate et al., 2013), although their global distribution remains highly uneven (Pugh, 1987), and individual records are often discontinuous.

The instrumental record is short, and RSL proxies are required to infer RSL changes and the contribution of processes that operate over longer timescales (Törnqvist et al., 2008; Lambeck et al., 2014; Toscano et al., 2011; Dutton et al., 2015). Whereas instrumental records are continuous with relatively small vertical error and essentially no age uncertainties, RSL proxy data exhibit sample-specific inferential and measurement uncertainties, as well as age uncertainty associated with the method used to date a sample (e.g., Törnqvist et al., 2015; Woodroffe et al., 2015; Hibbert et al., 2016). Generally, although not ubiquitously (e.g., Meltzner et al., 2017), uncertainty and temporal sparsity increase with the age of the data (Lambeck et al., 2014).

RSL proxy data provide different types of constraints on Holocene RSL. Index points constrain the discrete position of RSL at a given point in time and location and can be treated as independent records in statistical analyses, whereas continuous core records provide a near-continuous history of RSL change through time at a single geographic location (Gehrels et al., 2002; Varekamp et al., 1992). An age model is usually applied to continuous core records, and because all samples may not be directly dated, the points are not independent of one another. Like the distribution of tide gauge measurements, the distribution of RSL proxy data is uneven in time and space with the additional complexity of inherent age and vertical uncertainties. A particular challenge when working with RSL proxy data is the irregular distribution of geochronological uncertainty that arises from the process of radiocarbon calibration (Reimer et al., 2013). Age-depth models (e.g., Parnell et al., 2008) often handle these difficulties of radiocarbon dates for continuous sediment cores, and some return predicted age distributions with approximately normal uncertainties.

2.3 Hierarchical statistical model framework

Hierarchical statistical models are multilevel models that formalize the separation of total uncertainty into measurement error and inferential uncertainty (e.g., from the conversion of a proxy's elevation through indicative meaning to a distribution of likely RSL), and uncertainty in model

parameters (Cressie and Wikle, 2015). The primary goal in statistical analysis of sea-level data is to estimate latent (unobserved) RSL (i.e., the noise-free time series or spatio-temporal field) from observed, noisy data. At least three levels are defined in most sea-level model hierarchies. The data level characterizes the relationship between the observed data (instrumental or proxy) and RSL and incorporates measurement, inferential, and dating uncertainties of proxy data. The process level models true (i.e., noise-free) RSL and in some cases, separates RSL into the underlying processes that comprise it; and the parameter level captures key attributes of the data and process levels through unobserved parameters. Hierarchical models are well-suited to investigating rates of sea-level change because they are flexible and can accommodate missing data. In addition, the posterior probability distribution estimated in fitting a hierarchical model enables probabilistic statements about sea level over time and space (see Cressie and Wikle, 2015, for further details on hierarchical models).

2.3.1 Definition of relevant notation for hierarchical statistical framework

Conditional probability distributions are the basic mechanism for modeling uncertainty in hierarchical models. The *conditional probability distribution* of A, given B, is denoted $p(A|B)$. *Bayes' theorem* allows the inverse calculation of the conditional probability of unknown parameter(s) or process(es) (θ), given data (y) (Bayes, 1763):

$$p(\theta|y) = \frac{p(y|\theta)p(\theta)}{p(y)}. \quad (2.1)$$

The *likelihood* function $p(y|\theta)$ (also known as a sampling or data distribution) is the probability of observing the data y as described by the parameter(s) or process(es) θ of the fitted model. The *prior distribution* $p(\theta)$ expresses a priori beliefs about the unknown parameter(s) or process(es), before data have been observed, and $p(y)$ is the *marginal likelihood* of the data. The *conditional, posterior distribution* $p(\theta|y)$ is the resulting process or parameter distribution. The parameters used to construct the prior distribution $p(\theta)$, known as *hyperparameters*, can be fixed, estimated, or have (hyper)prior distributions themselves. For the remainder of this chapter, we will ignore the marginal likelihood and use the alternative form of Bayes' theorem that states the posterior is proportional to the likelihood times the prior.

In a simple hierarchical statistical model of sea level, the data model $p(y|f, \theta_d)$ expresses the distribution of the sea-level data y given the latent (unobserved) sea-level process f and the parameters of that distribution θ_d . Below the data level, the sea-level process model $p(f|\theta_s)$ incorporates scientific knowledge and uncertainty into the estimation of the true sea-level process through its conditional parameters θ_s . On the bottom level, the parameter model $p(\theta_d, \theta_s)$ specifies the distribution of all unknown parameters and hyperparameters.

$$\underbrace{p(f, \theta_s, \theta_d|y)}_{\text{posterior}} \propto \underbrace{p(y|f, \theta_d)}_{\text{data model}} \cdot \underbrace{p(f|\theta_s)}_{\text{process model}} \cdot \underbrace{p(\theta_d, \theta_s)}_{\text{parameter model}} \quad (2.2)$$

2.3.2 Analysis & modeling choices

Analysis choices describe decisions about how to implement a specific model structure (e.g., using least-squares analysis, Aitken, 1934; likelihood maximization, Wilks, 1938; or fully Bayesian analysis with Monte Carlo sampling, Hastings, 1970), whereas *modeling choices* refer to the relationships defined within a model and the assumptions made in constructing these relationships (e.g., a linear relationship between time and RSL). The hierarchical statistical framework accommodates a broad range of complexity in analysis and modeling choices; therefore, most methods of statistical analysis can be reframed as hierarchical models. For example, trends in sea level through time can be defined prior to analysis by explicitly assuming linear, polynomial, piecewise-linear, or other forms of the relationship between time and sea level at the process level. Non-parametric approaches, such as spline regression (Gharineiat and Deng, 2015) or Gaussian process regression (GPR; Rasmussen and Williams, 2006; e.g., Cahill et al., 2015a), can also be used to determine trends, without a pre-determined functional form also at the process level. We reframe several sea-level analyses from past publications within a hierarchical framework and highlight their analysis and modeling choices (Table 2.1).

2.4 Implementing the data level

The data level defines the relationship between observations (instrumental and proxy) and sea level, including associated uncertainties. The type of data determines its relationship with sea level and its uncertainties. Different data, therefore, require distinct data-level models to incorporate these

Table 2.1: Techniques table, which includes common techniques, analysis methods, modeling choices, the type of data typically used, relevant time periods to which this approach has been applied, and some examples in publications. Sections 2.5 and 2.6 provide details on the implementations of these techniques, and section 2.7 discusses specific analysis choices. TGs - tide gauges; CCs - continuous core records; SLIPs - sea-level index points; EIV - errors-in-variables; IGP - integrated Gaussian process; EOFs - empirical orthogonal functions.

Technique	Analysis Methods	Modeling Choices	Data	Time Period	Example Publications
Linear Regression	least squares	linear model	TGs,CCs, SLIPs	≤ 3 ky	Shennan et al. (2002); Engelhart et al. (2009)
EIV Change-point	errors-in-variable, Bayesian	change-point model	CCs,TGs, SLIPs	Common Era, Late Holocene	Kemp et al. (2013); Brain et al. (2015)
EIV IGP	errors-in-variable, Bayesian	Covariance functions, IGP, proxy systems model	TGs,CCs, SLIPs	Common Era, Holocene	Cahill et al. (2015a)
Regional Averaging	virtual stations, least-squares, ad hoc	Physical models	altimetry data, TGs	instrumental	Holgate (2007); Douglas (1991); Jevrejeva et al. (2009); Dangendorf et al. (2017)
EOF Regression	least squares	EOFs	altimetry data, TGs	instrumental	Church and White (2004, 2006, 2011)
Kalman Smoother	multi-model KS	Covariance functions, Physical models	TGs	instrumental	Hay et al. (2013, 2015, 2017)
Gaussian processes	EHM, Bayesian	Covariance functions, spatio-temporal, Physical models	TGs,CCs, SLIPs	Common Era, Holocene, LIGs	Parnell (2005); Kopp (2013); Kopp et al. (2015b); Khan et al. (2015, 2017)

relationships and uncertainties.

Regression models often assume that the independent variable, time t , has been measured exactly, and only account for error in time’s functional relationship with RSL f . Here,

$$y_i = f(t_i) + \varepsilon_i, \quad (2.3)$$

where y_i is proxy or instrumental observation i and $f(t_i)$ is true RSL at the time that y_i was observed. Many models assume measurement errors are normally distributed, such that $\varepsilon_i \sim \mathcal{N}(0, \sigma_i^2)$, where σ_i is the standard deviation of measurement uncertainty for observation i . In analyses that do not incorporate measurement uncertainty specific to each observation, ε (equation 2.3) is assumed to be independent, identically distributed (iid) Gaussian error and includes data and process uncertainty. The data level of a spatio-temporal model is equivalent to a time-series model, where true sea-level $f(\mathbf{x}_i, t_i)$ is dependent on both geographic location \mathbf{x}_i and time t_i .

The distinction between measurement uncertainty and inferential uncertainty (the relationship between RSL and a proxy’s position) can be explicit:

$$y_{ij} = f(t_i) + \varepsilon_i + \eta_j, \quad (2.4)$$

where ε_i is the measurement error for observation i , and η_j is the indicative meaning (vertical relationship of a proxy to contemporary tide levels) uncertainty for proxy type j ($\eta = 0$ for instrumental observations).

Instrumental data have negligible temporal error, while proxy data have inherent temporal uncertainties (e.g., from radiocarbon: Polach, 1976; Stuiver and Polach, 1977; Reimer et al., 2013; or U-series dating: Cheng et al., 2013). Incorporating temporal uncertainty into a model can be done in different ways, for example, using an errors-in-variables (EIV) framework (e.g., Kemp et al., 2013, Brain et al., 2015, Cahill et al., 2015a) or through approximation (e.g., NIGP approach of McHutchon and Rasmussen (2011); used, e.g., in Miller et al., 2013; Kopp et al., 2015b; Khan et al., 2017). Regardless of the technique, measurement uncertainties are separated from process noise at the data level:

$$\bar{t}_i = t_i + \delta_i^t, \quad (2.5)$$

where \bar{t}_i is the midpoint of the calibrated age for radiocarbon dating or U-series age, t_i is the true age, which is unknown and unobserved, and δ_i^t is temporal error, which is often approximated as normal within the analysis.

A transfer function, often called a forward model or proxy systems model, is a numerical technique used to derive past RSL estimates with uncertainty from raw micro-fossil input data (e.g., biological assemblages of foraminifera or diatoms) by establishing a formal relationship between the microfossil species abundances and tidal elevation (i.e., sea level) in a modern environment and using this relationship to infer past tidal elevation. It is a forward model in the sense that, given elevation, it will generate a set of microfossil species counts/proportions (e.g., species response curves produced by Cahill et al., 2016).

A key advantage of Bayesian hierarchical models (BHMs; Section 2.7.4) for RSL proxies is

that the data level of the model can link RSL directly to the raw data (e.g., microfossil species abundances, instrumental measurements) accounting for biases and measurement errors as part of the stochastic approach (the way that random error is handled). An entire general approach to proxy systems models has been developed by Parnell et al. (2015), which readily applies to RSL. However, in practice when a transfer function is included in a BHM, the model tends to become much more complex, as the link between the data and RSL is often highly non-linear and non-Gaussian, and thus requires extra information to calibrate (e.g., via modern analogue datasets or through physics-based deterministic models; Carson et al., 2018). This creates challenges for fitting models and estimating parameters. Therefore, application of a transfer function to derive RSL is usually carried out as an independent step prior to the process modeling we are discussing here.

2.5 Modeling the temporal sea-level process

RSL time series models have a long history, beginning with hand-drawn curves (e.g., Lighty et al., 1982; Zong, 2004; Smith et al., 2011; Abdul et al., 2016), data plotted in comparison to physical process models (e.g., models of GIA: Toscano et al., 2011; Engelhart and Horton, 2012), and GIA-corrected data plotted to estimate GMSL change (e.g., Fairbanks, 1989; Bard et al., 1990; Peltier and Fairbanks, 2006; Yokoyama et al., 2000). Models have evolved to include different forms of statistical regression, most of which do not separate data error from process noise, and instead incorporate both measurement noise and non-linear or high-frequency process variability into the error term, ε . Recasting these models in a hierarchical framework allows the separation of uncertainties of different types. Separating the data level from the process level enables more clear distinctions to be made in sea-level time series models so as to evaluate the appropriate method to use with a consistent comparison.

2.5.1 Temporally linear models

One of the simplest approaches to estimating RSL and an average rate of RSL change is fitting a temporally linear model to tide gauge and/or RSL proxy data. As just two examples, Shennan and Horton (2002) and Engelhart et al. (2009) applied simple linear regression to discrete index points and tide gauges in order to find the linear rate of change in RSL from GIA over the past

few thousand years, over which the rate of GIA is approximately constant. In both instances, the authors performed a linear regression on the midpoints of each RSL proxy data point and did not account for the vertical and temporal uncertainty in the data, combining equation 2.3 at the data level with the process-level relationship

$$f(t) = m \cdot t + \beta, \quad (2.6)$$

where $f(t)$ is true RSL, m is the constant rate of change in RSL, and β is the intercept. The slope m and y-intercept parameter β can be estimated using many analysis methods, but are most typically analyzed using least-squares regression.

Linear models are common and easy to use, and they provide a simple way to find a first-order constraint on rates over time periods when they are expected to be roughly constant. However, linear models can provide biased estimates of the slope parameters, due to their sensitivity to the temporal distribution of data. For example, intervals with a high concentration of data exert an undue influence on rate estimates. In addition, the linearity assumption is rigid; linear models lack the ability to model any evolution in rates of RSL change. Linear models are appropriate for modeling a first-order estimate, but are generally inappropriate for any more in-depth analysis.

2.5.2 Change-point models

Change-point models represent a time series as separate, linear sections and are generally employed to estimate the timing of changes in trend. For example, Kemp et al. (2013) tested whether late Holocene RSL was stable or included persistent and distinctive phases of variability. Additionally, Long et al. (2014) identified an acceleration in RSL change in the UK using this technique. At the process level, RSL f is modeled through time t with a linear change-point model, which assumes the underlying sea-level process is continuous and piecewise linear (i.e., linear in each section) and

each section has a different rate of change:

$$f = \begin{cases} \alpha_1 + \beta_1(t - \gamma_1), & \text{when } t < \gamma_1 \\ \alpha_1 + \beta_2(t - \gamma_1), & \text{when } \gamma_1 < t < \gamma_2 \\ \alpha_{j-1} + \beta_j(t - \gamma_{j-1}), & \text{for } j = 3, \dots, (m + 1), \text{ and } t > \gamma_{j-1}, \end{cases} \quad (2.7)$$

where γ_k is the change point and α_k is the expected value of RSL at the change point [with a continuity constraint, such that $\alpha_k = \alpha_{k-1} + \beta_{k-1}(\gamma_k - \gamma_{k-1})$], and β_j is the rate of sea-level change for each of the $m + 1$ segments. The parameters of change-point models can be estimated using a range of analysis approaches, including non-linear least squares and empirical Bayes (Section 2.7.3), but in the RSL modeling literature, these models generally follow Cahill et al. (2015b) in employing a change-point process model using a *Bayesian Hierarchical Model* (BHM; Section 2.7.4) within an EIV framework (Section 2.4).

While change-point models improve upon simple linear models and are fairly simple to implement, the linear constraints on each section are still fairly rigid and do not represent the true behavior of RSL. Change-point models are appropriate for estimating the timing of distinct phases when there is a clear pattern of phase-changes in the data. However, we recommend using an alternative model when fluctuations in the data reach a complexity that cannot be adequately captured by a small number of change points (i.e., 3 to 4).

2.5.3 Gaussian process models

A Gaussian process (GP) is a generalization of the Gaussian (normal) probability distribution. Extending the multivariate normal, which is fully defined by its mean vector and covariance matrix, to continuous time (and space) (Rasmussen and Williams, 2006), a GP is fully defined by its mean function $\mu(t)$ and covariance function, $K(t, t')$, where t is an input variable, here time (but can also include geographic location in spatial sea-level modeling; see Section 2.6). When RSL $f(t)$ is a GP, this is expressed as

$$f(t) \sim \mathcal{GP}\{\mu(t), K(t, t')\}. \quad (2.8)$$

The covariance function $K(t, t')$ defines prior expectations about the correlation between points in time (and space), and thus about the way in which information is shared between time points. More specifically, in RSL time-series models, the covariance function defines prior beliefs about the way that RSL varies over time. For example, Khan et al. (2015) applied models with GP priors to RSL proxy data at a global subset of sites to characterize regional RSLs.

In a GP model, $f(t)$ is a non-parametric depiction (i.e., the form is not predetermined). Accordingly, GP time-series models have much more flexibility than temporally linear or change-point models. The shape of the curve is driven by the data, as opposed to a predetermined functional form.

One specific type of GP model is an Integrated Gaussian Process (IGP) model, which places a GP prior on the rate process rather than the sea-level process. For example, Cahill et al. (2015a) estimated the continuous and dynamic evolution of RSL change in North Carolina from sediment cores using change-point models. At the process level, IGP regression models $f'(t)$, the RSL rate process, as a GP. The underlying RSL process $f(t)$ is the integral of the rate process, plus a constant intercept α :

$$f'(t) \sim \mathcal{GP}\{\mu(t), K(t, t')\}, \quad (2.9)$$

$$f(t) = \alpha + \int_0^t f'(u) du, \quad (2.10)$$

where t is true time.

In both GP and IGP models, the covariance functions can take a range of functional forms (Section A.1). The form and parameters of the covariance function [called *hyperparameters*, as they set assumptions that inform the non-parametric representation of $f(t)$] define how abruptly modeled RSL may change with temporal (or spatio-temporal) distance. Scale hyperparameters express prior beliefs about the amplitude of variability over time (or space). Range hyperparameters (or characteristic length scale) set the distance over which the correlation between two sites or times decays toward zero. Smoothness parameters determine the speed of decay in the correlation in time or space (e.g., the degree of differentiability). For fixed hyperparameters, GP posterior distributions

are analytically tractable (i.e., no approximation or sampling is necessary) when data uncertainty is represented as normally distributed; statistically speaking, this reflects the fact that the normal distribution is self-conjugate.

Key disadvantages of GP and IGP models include their complexity and relatively long analysis times. The common assumption that the covariance function is stationary – e.g., that prior expectations about the relationship between RSL at 10 ka and 8 ka are the same as those between 4 ka and 2 ka – is a rough approximation, although still more flexible than parametric approaches. IGP models generally make the same assumption about rates as opposed to levels, which is a somewhat more accurate approximation.

For the casual analyst, GP models are considerably more difficult to implement than linear or change-point models, although an increasing number of tools are available to assist in their implementation (e.g., Kopp, 2016; Cahill, 2018). The hyperparameters that characterize aspects of the covariance function – e.g., prior expectations regarding amplitude and scales of variability – are readily derived from the posterior probability estimate of $f(t)$. GP models are appropriate for many applications because of their flexibility and ability to incorporate physical knowledge regarding ranges and scales of variability through their covariance functions (Section A.1).

2.6 Modeling the spatio-temporal sea-level process

Reconstructing the spatio-temporal RSL field allows information to be shared among disparate sites and estimation of RSL and its rates of change at sites where there are no data. Spatio-temporal models also support the estimation of change in global-mean sea level (GMSL), which is defined as the spatial average of RSL or SSH (sea-surface height) over the ocean (Gornitz et al., 1982). Most spatio-temporal models implemented in the literature are not explicitly hierarchical, but – as with time-series models – they can be recast in this way in order to compare their process levels.

Spatio-temporal RSL models represent a continuum from purely statistical to purely physical models. At the purely statistical end, the priors of the process level relating RSLs from different locations to one another are based solely on their spatial and temporal proximity. At the purely physical end, a deterministic model (e.g., a GIA model) is used to estimate the RSL field.

2.6.1 RSL represented with single or multiple GP priors

The simplest and most fully statistical models place a single GP prior on RSL, as in equation 2.8 (with covariance dependent on both time and geographic location), conditioning on RSL proxy or instrumental data, and result in a posterior distribution of RSL in time and space. The covariance function in this context may be spatially and temporally separable, in which case it is represented as the product of a temporal covariance function and a spatial covariance function. The former describes prior expectations about scales of change in time, the latter about scales of change in space. The analysis of a spatio-temporal GP is amenable to the same approaches as a temporal GP.

A single GP with a parameteric covariance function is rarely implemented in the spatio-temporal RSL modeling literature, however, because a single scale of temporal variability and a single scale of spatial variability is too simple to capture physical behavior. More physical insight recognizes that RSL should have multiple spatio-temporal scales of variability, and can therefore be represented as the sum of multiple terms with GP priors. Kopp (2013) introduced this approach into the the spatio-temporal RSL literature to model tide-gauge data along the east coast of the United States in order to determine whether there was a regional acceleration in RSL. His process model employed nine separate terms with GP priors, combining three spatial scales of variability (global, regional, and local) with three temporal scales of variability (low, medium, and high frequency). Lower resolution RSL proxy data frequently require a simpler process level. For example, several studies (e.g., Kopp et al., 2016; Khan et al., 2017) employ models of the form:

$$f(\mathbf{x}, t) = g(t) + r(\mathbf{x}, t) + m(\mathbf{x}, t), \quad (2.11)$$

where $g(t)$ represents a global term that is common to all sites and could include (in a global analysis) the global-mean effects of thermal expansion and changing land ice volume; $r(\mathbf{x}, t)$ is a regional term, which might represent processes like GIA, ocean/atmosphere dynamics, and the static-equilibrium effects of land-ice mass changes; and $m(\mathbf{x}, t)$ might capture more local processes, like tectonics and natural sediment compaction.

2.6.2 Empirical orthogonal functions

Empirical orthogonal function (EOF) regression is an extension of principle component analysis (PCA) and seeks structures that explain the maximum amount of variance in a dataset. For example, Church and White (2004), Domingues et al. (2008), and Ray and Douglas (2011) used EOF decomposition (after correction for GIA) to calculate the dominant spatial patterns of (high-frequency) variability in SSH from altimetry observations, and applied those to tide gauge data in order to estimate GMSL change. Using EOF decomposition can be viewed as a form of process knowledge, although incorporating less physical knowledge than approaches that link to physical models. The process level in EOF regression can be represented as:

$$f(\mathbf{x}, t) = g(t) + \sum_i U_i(\mathbf{x})\alpha_i(t) + GIA(\mathbf{x}, t - t_0). \quad (2.12)$$

Here, $g(t)$ is a global “mode” that is constant over space, each U represents a leading spatial EOF, α is a time series of amplitudes of the EOFs, and $GIA(\mathbf{x}, t - t_0)$ represents the GIA term (implemented through a correction from a single, selected GIA model). The solution, including the amplitudes of the leading EOFs, models the change in RSL from one time step to the next (e.g., monthly averages for Church and White, 2004, 2011).

The assumption that dominant spatial patterns are constant over time, across frequencies of variability, and over the changing selection of tide gauges may lead to biases because of the sensitivity of EOFs to the choice of spatial domain and time period. Additionally, features can be mixed between EOFs and there is no guarantee the EOF pattern has physical meaning; instead, the patterns can represent noise (see Calafat et al., 2014 for a more extensive critique).

2.6.3 Incorporating physics-based models

Still more physical knowledge can be incorporated at the process level through physical models. For example, Kopp et al. (2009) used physical models of glacial-isostatic adjustment (GIA) to help define the covariance structure of a spatio-temporal GP for an analysis of GMSL and RSL change during the Last Interglacial. Additionally, although the analysis methods (Section 2.7) used in the implementations differ, the process models of Hay et al. (2015) and Dangendorf et al. (2017), used

to analyze the instrumental record, are similar variants of:

$$f(\mathbf{x}, t) = g(t) + \sum_j FP_j(\mathbf{x})M_j(t) + DSL(\mathbf{x}, t) + GIA(\mathbf{x})(t - t_0) + NL(\mathbf{x}, t) + w(\mathbf{x}, t). \quad (2.13)$$

The spatio-temporal RSL field is split into several component fields. Here, $g(t)$ is a globally-uniform term that includes global thermal expansion and unmodeled sources of change. (It is not, however, representative of GMSL, as several of the terms have non-zero global means). FP_j and M_j are the static-equilibrium fingerprint and melt, respectively, for each ice sheet/glacier source regions, indexed by j . $DSL(\mathbf{x}, t)$ is dynamic sea-level change, estimated using information from atmospheric/ocean global climate models. $GIA(\mathbf{x})$ is the local contribution to RSL from GIA, estimated using information from GIA process models, and $w(\mathbf{x}, t)$ is process noise. Each implementation incorporated physics-based models in different ways (see Section 2.7).

An advantage to incorporating knowledge of processes through physical models is that they add potential information in the open ocean, far from tide gauge sites, whereas purely statistical models lose power away from the data. A disadvantage is that they can be more complex to implement and may be overly rigid, relying on a small number of interpretations of physical processes, without comprehensively accounting for uncertainties in the parameters that determine that process.

2.7 Analysis choices

Analytical approaches used in the sea-level modeling literature include least-squares analysis (e.g., Church and White, 2004; Shennan and Horton, 2002; Engelhart et al., 2009), *ad hoc* approaches such as “virtual station” averaging (e.g., Jevrejeva et al., 2006; Dangendorf et al., 2017), and Bayesian approaches including empirical Bayesian analysis (e.g., Kopp et al., 2009; Khan et al., 2017; Meltzner et al., 2017), fully Bayesian analysis (e.g., Parnell, 2005; Cahill et al., 2016), and Kalman smoother (KS) algorithms (e.g., Hay et al., 2015). Simple process models can be implemented with almost any analysis choice, while more complex models may require non-linear least squares or a Bayesian approach.

2.7.1 Least squares

Least-squares analysis optimizes a model by minimizing the sum of squared deviations between the observed RSL and a RSL-process model function (Legendre, 1805). It can be used with functions as simple as a line (i.e., simple linear regression, Section 2.5.1) or as complex as in EOF regression (Section 2.6.2). Least-squares analysis is included with most statistical software (e.g., R, MATLAB, SAS) and is easy to implement with many modeling choices. However, ordinary least-squares (OLS; Aitken, 1934) analysis does not include implementation of a data level, and therefore typically excludes explicit measurement error and inferential uncertainties.

Slightly more advanced solutions than OLS include weighted least squares (WLS) and generalized least squares (GLS). WLS addresses the problem of *heteroscedastic* (unequal) variances, and GLS additionally addresses the problem of autocorrelation among variances, both of which are common characteristics of data used in sea-level analyses. GLS estimators can be more efficient than OLS estimators (Goldberger, 1962). OLS, WLS, and GLS all require parametric linear models (though note that a linear model need not be a linear function of time). Conversely, total least squares (Golub, 1973; Golub et al., 1999) is a generalization of the least-squares approximation method and incorporates uncertainty in both the independent and dependent variable, and non-linear least squares uses optimization algorithms to maximize the fit of more complex models.

2.7.2 Ad hoc approaches: regional averaging, virtual stations, pre-processing

We define “*ad hoc*” approaches as analysis methods constructed without an underlying statistical theory. Modern estimates of GMSL change apply various versions of these ad hoc approaches, including regional averaging, “virtual stations,” and pre-processing to different subsets of tide gauges. The results of these techniques exhibit various GMSL curves (Figure 2.1).

Regional averaging effectively removes the contributions of some processes, such as those included in the regional and local terms of purely statistical models. Definitions of the number of regions and how the averaging is implemented vary by study. Jevrejeva et al. (2006, 2009, 2016) attempted to address the spatial heterogeneity of tide gauges separated by geographic regions through a “virtual station” approach, which iteratively averages rates between stations to estimate a regional average and then averages across all regions to find a global average. Dangendorf

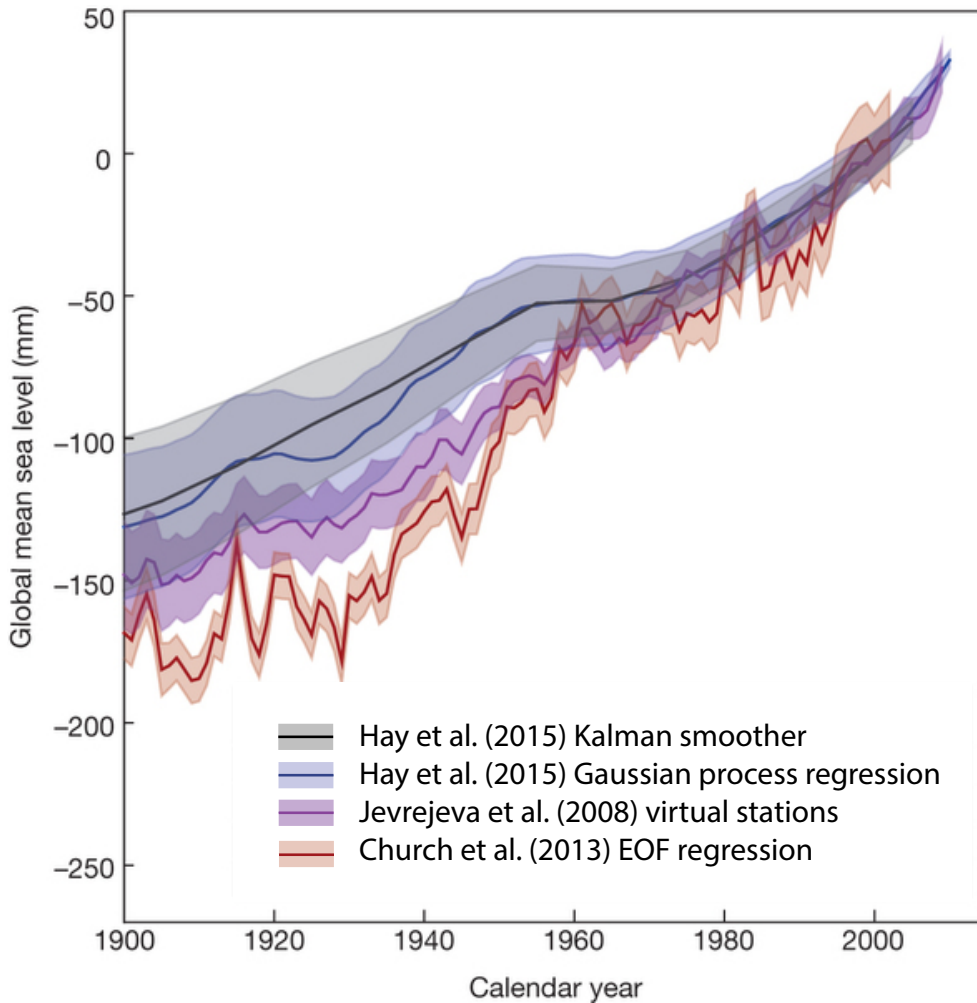


Figure 2.1: Comparison of GMSL curves based on different subsets of tide gauges, process model choices, and analysis methods, including KS, GP, virtual stations, and EOF regression (Jevrejeva et al., 2008; Church et al., 2013b; Hay et al., 2015).

et al. (2017) adopted the general idea of Jevrejeva’s “virtual station” technique and weighted each regional estimate by its approximate area in relation to the entire ocean.

Regardless of the model, many analyses in addition to regional averaging, “correct” for physical processes prior to analysis (e.g., Cahill et al., 2015a; Tamisiea and Mitrovica, 2011; Church and White, 2011) by subtracting out signals from physics-based process models *ad hoc* prior to analysis (i.e., pre-processing). For example, within regional averaging implementations, Douglas (1991, 1997) and Holgate (2007) corrected for the effects of GIA using single GIA models. Dangendorf et al. (2017) corrected each tide gauge, prior to analysis, according to the static-equilibrium fingerprint,

a melt component, GIA, and vertical land motion, which were each estimated by physical process models.

While some regional averaging techniques are fairly simple to implement, others are more complex. Advantages of simpler approaches are ease of use and straight-forward implementation. The Jevrejeva et al. (2006) technique assumes that RSL varies linearly in space, while the more simplistic averaging does not take within-region spatial variability into account. The selection of a subset of tide gauges (with bias toward sites at latitudes less than 60°), without addressing sparsity in time and space, introduces a potential bias into estimates of GMSL by not accounting for the physics or geometry of the contributing processes (Hay et al., 2015). Regional averaging does not produce the spatio-temporal RSL field, and only estimates regionally-averaged changes in RSL in addition to GMSL.

2.7.3 Empirical Bayesian analysis

Empirical Bayesian analysis, employing an *Empirical Hierarchical Model* (EHM), uses point estimates of the parameters based on the RSL data (e.g., Kopp et al., 2016; Hay et al., 2015). Maximum likelihood estimates (MLEs, $\hat{\theta}$) are optimal point estimates found by maximizing the likelihood $p(y|\theta)$ of the model, given fixed data. Each set of parameters has a distinct likelihood, and the optimal parameters are the ones with the highest likelihood for the given dataset. An EHM results in a posterior distribution of RSL, conditional on the data and the optimal parameters $p(f|y, \hat{\theta}_s, \hat{\theta}_d)$. Although explicit bounds are usually set for MLEs, there is no explicit prior distribution on the parameters. Instead, the parameter level describes the optimization or estimation of the data and process parameters, θ_d and θ_s , respectively:

$$\underbrace{p(f|y, \hat{\theta}_s, \hat{\theta}_d)}_{\text{posterior}} \propto \underbrace{p(y|f, \hat{\theta}_d)}_{\text{likelihood}} \cdot \underbrace{p(f|\hat{\theta}_s)}_{\text{prior}}. \quad (2.14)$$

Almost all published implementations of RSL process models with spatio-temporal GP priors for proxy analysis use empirical Bayesian analysis (e.g., Kopp et al., 2009, 2015b; Khan et al., 2017). For instrumental data, Hay et al. (2015) demonstrated an EHM with GP priors alongside the KS approach (Section 2.7.5) to estimate GMSL, the spatio-temporal RSL field, and the components contributing to RSL globally at decadal intervals from tide gauge records. Meltzner et al. (2017)

implemented an empirical GP model using coral microatoll proxy data from the mid-Holocene in Southeast Asia to estimate rates of RSL change by incorporating a periodic term to capture the 18.6-year tidal cycle (Chapter 4).

EHMs generally require fewer computational resources than fully Bayesian techniques; however, like fully Bayesian approaches, empirical GP implementations require computation of a full covariance matrix (over all times and space), the computational demands of which are more strenuous than a state-space model (i.e., that estimates a covariance matrix at each time step). For this reason, EHM analyses (and BHM analyses) do not scale to large datasets as easily as other approaches.

2.7.4 Fully Bayesian analysis

Another analysis choice, fully Bayesian analysis, gives rise to a Bayesian Hierarchical Model (BHM). A fully Bayesian analysis requires that all model parameters have prior probability distributions, allowing parameters to take on a range of probable values. These prior distributions may incorporate a priori information or be uninformative, expressing vague information. Priors are typically sampled using *Markov Chain Monte Carlo* techniques (MCMC: algorithms used to approximate random samples from complex probability distributions, e.g., Gelman et al., 2011); however, for a limited set of likelihood and *conjugate prior* distributions, combined with relatively simple model structures and known hyperparameters, they can be solved analytically.

The output of a BHM is the posterior distribution $f, \theta_s, \theta_d | y$ of the sea-level process f (e.g., the probability distribution of RSL at a specific point in time and space) and the parameters, θ_s and θ_d , given the observed data y . This posterior is proportional to the product of the likelihood of the model $p(y|f, \theta_d)$, the prior distribution of the model $p(f|\theta_s)$, and the prior of the parameters $p(\theta_d, \theta_s)$, where θ_d and θ_s are the data and sea-level process hyperparameters, respectively:

$$\underbrace{p(f, \theta_s, \theta_d | y)}_{\text{posterior}} \propto \underbrace{p(y | f, \theta_d)}_{\text{likelihood}} \cdot \underbrace{p(f | \theta_s) \cdot p(\theta_d, \theta_s)}_{\text{prior}}. \quad (2.15)$$

As with empirical Bayesian analysis, fully Bayesian analysis can be implemented with virtually any process model (e.g., Parnell et al., 2015; Cahill et al., 2015b, 2016; Piecuch et al., 2017). In general, it is more computationally demanding than an empirical Bayesian analysis but provides

more thorough estimates of relative uncertainties (e.g., Piecuch et al., 2017).

2.7.5 Kalman smoother techniques

The Kalman smoother can combine process-based models of the drivers of sea-level change with spatially and temporally sparse observations to estimate a temporal or spatio-temporal model. Implementation of the Kalman smoother (KS) is based on the Kalman filter (Kalman, 1960), a data assimilation technique that iteratively performs a least-squares analysis whenever observations are available, but in the absence of observations relies on model dynamics to compute the best estimate of the state vector. The Kalman filter method assumes that the state at time k evolves from the state at $k - 1$. The approach is similar to a Bayesian updating process, which occurs one time step at a time, or a linear Gaussian state-space model (examples of non-linear, non-Gaussian state-space models include Parnell et al., 2015 and Cahill et al., 2016). The Kalman smoother extends the Kalman filter so that estimates at any given point in time are informed by observations in its future as well as in its past. For example, Hay et al. (2013, 2015, 2017) used the Kalman smoother to implement a model similar to that in equation 2.13 and thus model GMSL, the field of RSL change, and different driving processes (see Section A.2.2 for more details on this implementation).

The KS approach is flexible in terms of process models that can be represented and is computationally faster than approaches (such as EHMs or BHMs) that require estimating all spatio-temporal points simultaneously. However, it fails for low data density (which can be shown analytically; see Hay et al., 2017; Gelb et al., 1974), does not readily handle temporal uncertainty (Kalman, 1960; Visser and Molenaar, 1988), and has not yet been implemented in the literature using proxy data.

2.8 Illustrative analyses

To illustrate the advantages and disadvantages of specific implementations in RSL modeling, we applied several modeling and analytical methods to common datasets. We focused on pairs of modeling and analytical choices that commonly occur together in the literature: temporal-linear models with least-squares analysis (e.g., Shennan and Horton, 2002; Engelhart et al., 2009); change-point and EIV-IGP models with fully Bayesian analysis (e.g., Brain et al., 2015; Cahill et al., 2015b; Cahill, 2018); temporal and spatio-temporal models with GP priors with empirical Bayesian

analysis (e.g., Khan et al., 2015; Hay et al., 2015; Kopp et al., 2016); and Kalman smoother with a physically informed model (e.g., Hay et al., 2013, 2017). The type of data, time period of interest, and relevant question determine which techniques are appropriate. First, we demonstrate the differences between several time-series models (linear, change-point, GP, IGP) to estimate RSL change from continuous-core data over the Common Era. The quasi-linearity of RSL over this period warrants an evaluation of linear and change-point models. Next, we demonstrate a spatio-temporal GP model with empirical Bayesian analysis, which characterizes spatial and temporal variability in RSL change over the Holocene using RSL proxy data. This is the only technique currently used in the literature that accommodates both temporal uncertainties and spatial correlations. Last, we analyze tide gauge data with KS and GP models, as they are capable of estimating both GMSL and the spatio-temporal field of RSL and its rates of change with uncertainties.

2.8.1 Estimating rates of RSL change from continuous cores (Common Era to present)

Identifying accelerations in rates of RSL change, and their causes, can be challenging based on short instrumental records, and thus requires RSL proxy data. In particular, the near-continuous records from single cores of salt-marsh sediment are well-suited to capturing the onset of modern rise because they bridge the gap between instrumental measurements and sea-level index points, and they possess sufficient vertical and temporal resolution to provide a meaningful estimate of when modern RSL rise was initiated. The data used in the following analyses include previously published data from continuous cores from two sites in New Jersey (i.e., Leeds Point and Cape May Courthouse; Kemp et al., 2017b, 135 data points) and one site in North Carolina (i.e., Sand Point; Kemp et al., 2017c, 109 data points), where the NJ sites are assumed to be independent of the NC site.

Models and implementations

Temporally linear model: Using a simple, temporally linear model, we applied ordinary (OLS) and general (GLS) least-squares analyses to the continuous core records. The OLS analysis was conducted on the mean RSLs and median ages for each continuous core record (i.e., excluding

vertical and temporal uncertainties). The GLS analysis included vertical (RSL) uncertainty (Figure 2.2). The estimated OLS and GLS parameters are similar for the two sites (Figure A.1, table a).

Change-point regression: We implemented a linear change-point model with fully Bayesian analysis and incorporated temporal uncertainty within an errors-in-variable framework. The NJ record was best fit by a model with three change points, whereas the NC record was best fit with two change points (Figure A.1, table b).

Empirical temporal GP model (ET-GP): We implemented a temporal-only model with GP priors using empirical Bayesian analysis with the following process model:

$$f(t) = l(t) + m(t) + w(t), \quad (2.16)$$

where $l(t)$ and $m(t)$ are low- and medium-frequency terms, respectively, and $w(t)$ is high-frequency variability, interpreted as white noise. The $l(t)$ and $m(t)$ terms were each assigned zero-mean GP priors with once-differentiable Matérn(3/2) covariance functions (Section A.1). Using empirical Bayesian analysis, the optimal point estimates of the hyperparameters varied for the two independent models (Figure A.1, table d).

Bayesian EIV-IGP: We implemented the EIV-IGP model (Section 2.5.3) with fully Bayesian analysis, where the posterior distributions on the hyperparameters differed for the two models (Figure A.1, table c).

Results and discussion of temporal models during the Common Era from continuous cores

The uncertainties in these implementations differ more than their central-tendency estimates of RSL, although the disparities in predictions at the beginning and end of the analysis period are greater than in the middle. The ET-GP, change-point, and EIV-IGP models allow the incorporation of temporal and vertical uncertainty and therefore more appropriately characterize the errors in the models (Figure 2.2). The rigid linearity of the temporally linear model does not accommodate the process underlying the data. The ET-GP and Bayesian EIV-IGP models yield similar mean estimates, although the Bayesian EIV-IGP makes somewhat more precise predictions (Figure 2.2) in this particular application.

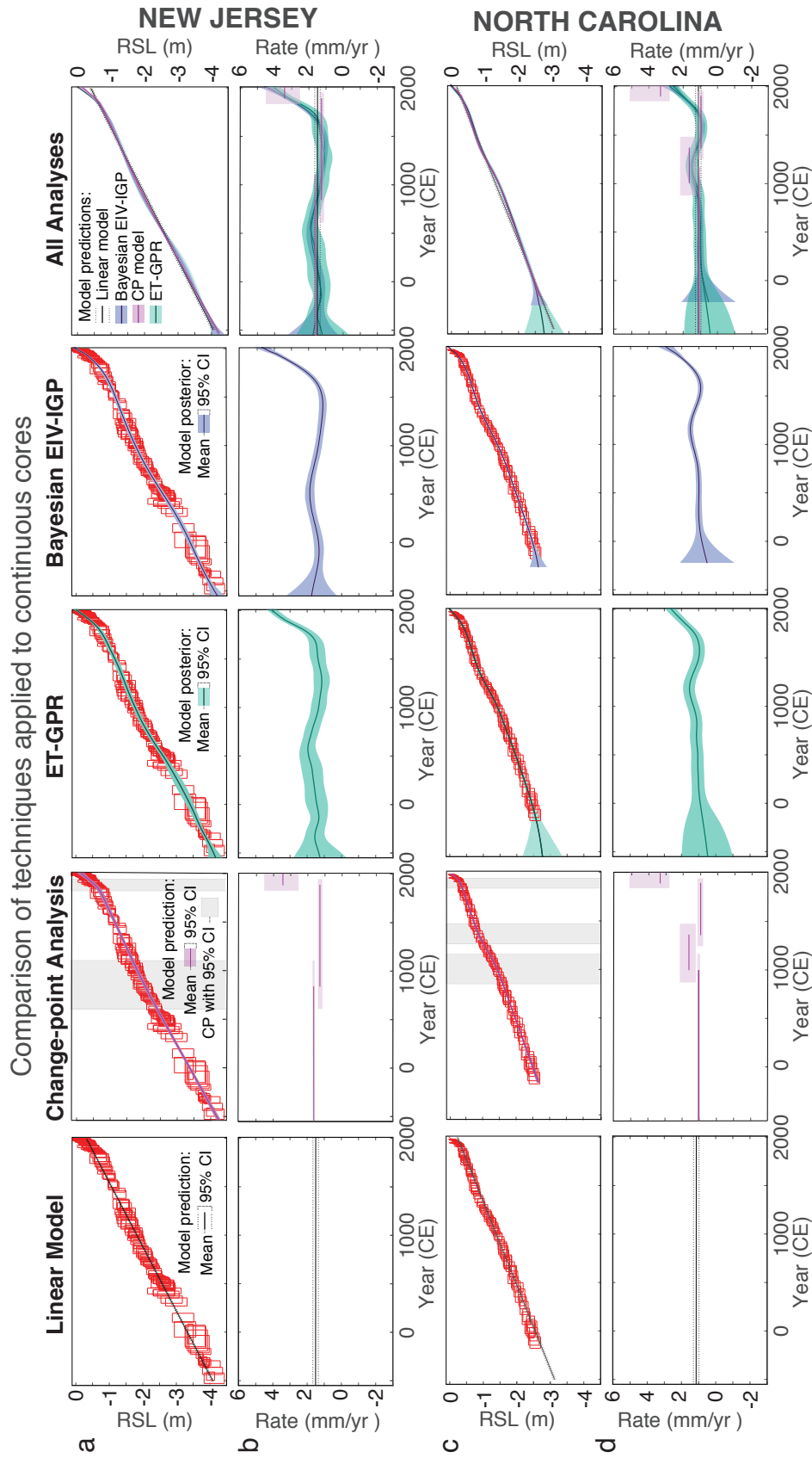


Figure 2: Common Era comparison of (column 1) linear model results, (column 2) change-point analysis, (column 3) empirical temporal GP model results, and (column 4) Bayesian EIV-IGP model results, where input data are continuous cores, and there is no spatial correlation, in (a,b) New Jersey, and (c,d) North Carolina. Output includes estimates of (a,c) RSL and (b,d) rates of RSL change, which are each shown with mean and 95% confidence or credible intervals.

The residuals of the linear model display a non-random pattern (Figure 2.3) indicating that the model does not fit this dataset well. The non-linear models (Figure 2.3) show less structure in the residuals, as well as smaller residuals than the linear model. The non-parametric nature of the Bayesian EIV-IGP and ET-GP lead to estimates of both RSL and rates of RSL change (Figure 2.2) that are more informed by the data as opposed to predetermined by the functional form.

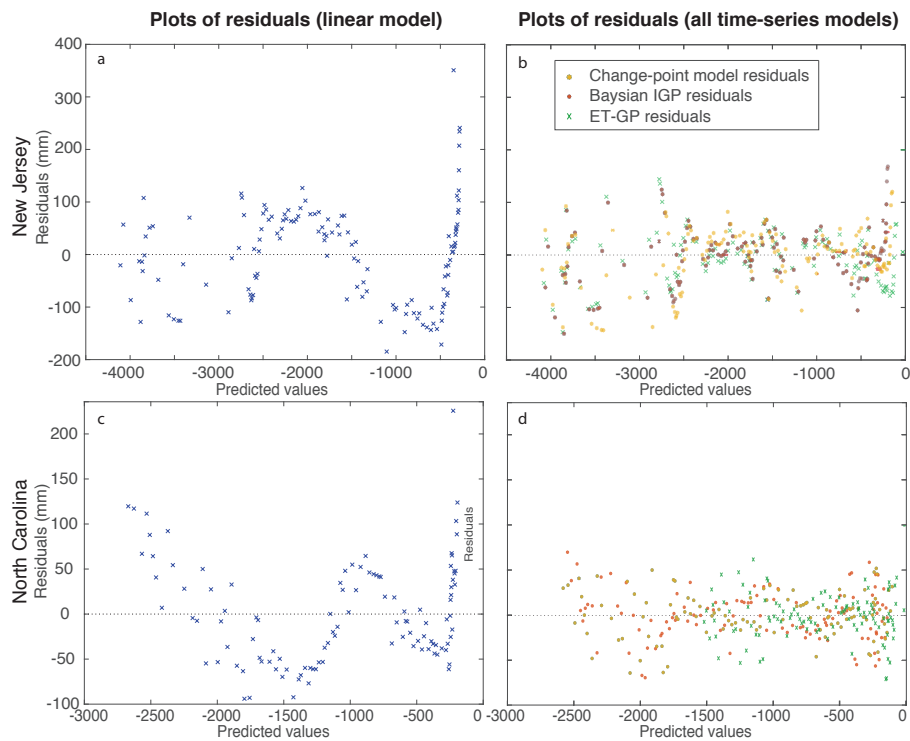


Figure 2.3: (a,c) Linear model and (b,d) all models residuals plotted against the predicted values for each site (a,b: NJ, c,d: NC).

There are a number of analytical methods that can be used to evaluate a given scientific question. When the question relates to the rates of change during a specific time period, and the relevant data are continuous cores, fully Bayesian and empirical Bayesian analyses, for a given modeling choice, are both appropriate. An advantage of both of these analytical methods is that they can be applied flexibly to many modeling choices and allow the data to determine the form of the posterior distribution when using non-parametric models.

Relative to simpler analysis choices, a challenge of empirical Bayesian analysis and fully Bayesian analysis can be the computational time. On a desktop computer, with the 135 New Jersey data points, least-squares analysis is trivially fast (<2 seconds). With relatively similar process models,

the ET-GP model takes ~ 60 seconds to run, with most of the computational time occupied by the hyperparameter optimization. The sampling required for the fully Bayesian EIV-IGP model yields a computational time about two orders of magnitude slower (6.1 hours). Considering four different possible numbers of change points, the fully Bayesian change-point regression took about 24 minutes to run. Although these run times are all trivial with respect to the time to collect data, computational time is not in general a trivial consideration. Statistical modeling is an iterative process of model development, model fitting, and model criticism, and slow analysis methods can be a hindrance to this process. Moreover, the computational time can scale rapidly with the number of data points. The time to invert a covariance matrix for a GP analysis scales with the cube of the number of data points, and the computational time of a model that both inverts a covariance matrix and samples temporal uncertainty (e.g., the EIV-IGP) scales with the number of data points to the fourth power. Conducting the empirical Bayesian analysis with 5000 data points, for example, would lead to a computational time for a single model iteration of about 35 days; the fully Bayesian EIV-IGP analysis on the same dataset and same computational platform would – without improvements in computational efficiency – take about 1,300 years.

Each modeling choice has advantages and disadvantages. As a modeling choice, linear regression is sensitive to the temporal distribution of data and influential data points. However, when uncertainties in the data are incorporated into the model, linear regression is appropriate to determine first-order rates of change in processes that have approximately constant rates, and advantages include its ease of use and computational speed. One limitation of the change-point approach is that phases of persistent sea-level behavior are approximated by linear trends that may not accurately represent the underlying physics of RSL change and mask (to some degree) the continuous evolution of RSL through time (Cahill et al., 2015a). Drawbacks of these more simplistic approaches motivated Cahill et al. (2015a) to develop an objective (non-parametric IGP) methodology for estimating rates of RSL change from multiple types of proxy data (Sections 2.5.2 and 2.5.3) and Kopp (2013) to use spatio-temporal GP models (Section 2.6), which share information from nearby geographical sites to overcome the limited length of records in certain locations.

Some of the differences between the ET-GP and EIV-IGP models are associated with the conventional choices of covariance functions used. The squared-exponential covariance function, used

in the Bayesian EIV-IGP, is slightly smoother in this implementation than the Matérn covariance function in the ET-GP (Figure 2.2). The ET-GP method as employed enables more complexity for various processes through multiple separate covariance functions, summed together to create the composite RSL process. Either method could incorporate various covariance functions, however. Whereas the Bayesian EIV-IGP models rates as the variable of interest and integrates to produce the RSL estimates from the rate curve, each of the other implementations model RSL, and the ET-GP derives the rates of RSL change and their uncertainties through a linear transformation.

Both the EIV models and the ET-GP incorporate temporal uncertainty into the models. The EIV method implements this directly through sampling, and the ET-GP approximates and recasts temporal noise into RSL uncertainty using *noisy input GP (NIGP)* methods. If the goal of an analysis is to evaluate rates of change at a specific site, then the Bayesian EIV-IGP implementation has hyperparameters that are more readily interpretable. However, if combining information from various sources and locations is important in an analysis, a spatio-temporal version of the ET-GP would enable this over the Bayesian EIV-IGP, which has only been implemented in a purely temporal model.

2.8.2 Characterizing spatial and temporal variability in RSL change from proxy data (Holocene to present)

We compiled data from previously published studies (Engelhart and Horton, 2012; Kemp et al., 2013, 2014, 2015, 2017a,c; Khan et al., 2017) in the Caribbean and along the Atlantic coast of the United States (latitudes 24.95–44.68°N, longitudes 67.38–81.73°W) from 12 ky BP (years before 1950 CE) to present (Supplemental A.4). The dataset compiled in Engelhart and Horton (2012) consists of 450 index points spanning from 8 ky BP to present. The dataset compiled in Khan et al. (2017) consists of 66 index points from 11 ky BP to present. The datasets of Kemp et al. (2013, 2014, 2015, 2017a,c) consist of 498 continuous core records and 28 index points from 3 ky BP to present.

Models and implementations

Empirical spatio-temporal GP model (EST-GP): We implemented an empirical spatio-temporal GP model (EST-GP) using discrete index points and continuous core records with the process model in equation 2.11 with an addition white noise term, $w(t)$. In this implementation, $g(t)$, $r(\mathbf{x}, t)$, and $m(\mathbf{x}, t)$ are common, regional, and local terms, respectively, each with zero-mean GP priors with Matérn(3/2) covariance functions. We removed the data from one site, Inner Delaware, to test the performance of the EST-GP model without any site-specific input, such that all information for predicting RSL comes from the correlation in RSL with other sites (Figure 2.4).

Bayesian EIV-IGP for single sites: As in Section 2.8.1, we implemented the Bayesian EIV-IGP (Section 2.5.3), which does not include a spatial component, in order to provide a comparison to the spatio-temporal model. The input data for New Jersey and North Carolina were equivalent to the EST-GP, including index points and continuous core records from each location.

Results and discussion of empirical spatio-temporal GP (EST-GP) and temporal-only Bayesian EIV-IGP models for full Holocene

Whereas the Bayesian EIV-IGP model only predicts RSL and rates of RSL change at sites with data (because the model is temporal only and runs independently for each site), the EST-GP makes predications at any point in space and time. Despite the omission of data at Inner Delaware (Figure 2.4f), where the data are only shown for comparison purposes, the predictions fall quite close to the data. Only two out of 28 data points fall outside of the 95% confidence interval model prediction of RSL.

One notable difference between the EIV-IGP and the EST-GP difference in modeling choices is the spatial correlation within the EST-GP model. The form of the RSL curve in North Carolina (Figure 2.4e) is influenced by this correlation. Whereas the Bayesian EIV-IGP model produces higher RSL at 11 ka than 10 ka, the EST-GP uses information from the correlation with other sites to estimate increasing RSL throughout the Holocene. The EST-GP also maintains fairly constant uncertainties throughout the period of interest, whereas the Bayesian EIV-IGP has less precision

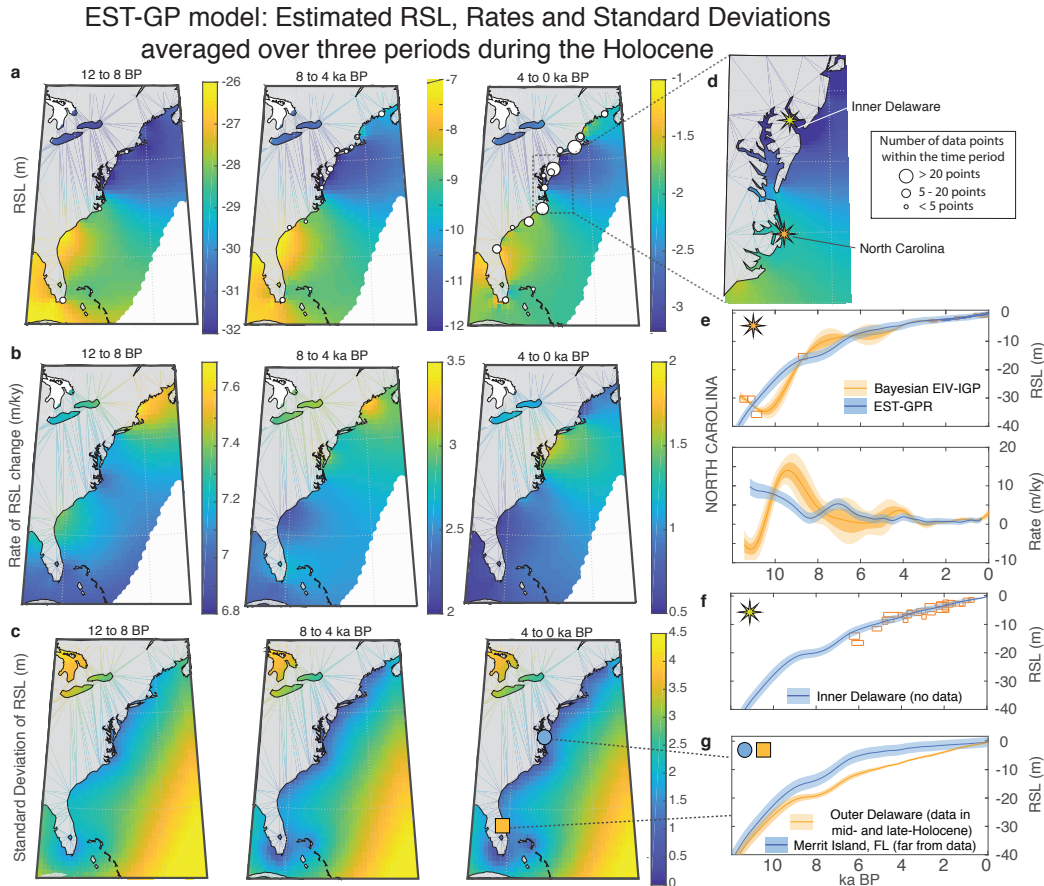


Figure 2.4: Spatio-temporal Holocene model (EST-GP) results, including maps of mean estimated (a) RSL, (b) rate of RSL change, and (c) standard deviation of RSL, averaged over 4000-year periods. (d) Stars on the map show the locations of two sites with (e,f) estimated RSL curves. (e) Comparison of predicted RSL and its rates of change are shown with 95% credible intervals at North Carolina for the EST-GP (includes spatial correlations) and Bayesian EIV-IGP models. (f) The EST-GP makes predictions at a site, Inner Delaware, where no data were used as input; data are shown for comparison purposes only. (g) Two models demonstrate the difference in uncertainties when the model is close to data (Outer Delaware, orange) versus far from data (Merrit Island, blue).

when data are sparse, due to the assumption of independence between sites (through the temporal-only implementation). However, at times and locations farther away from the data, the uncertainty increases in the EST-GP model, as well (Figure 2.4c). Predicted uncertainty in RSL is greater at sites that are far from data (e.g., Merrit Island, FL; Figure 2.4g), whereas uncertainties decrease at times and locations with precise data points.

In these specific implementations, another notable difference is the process level model of the EST-GP, which has three distinct terms capturing common, regional, and local signals. These

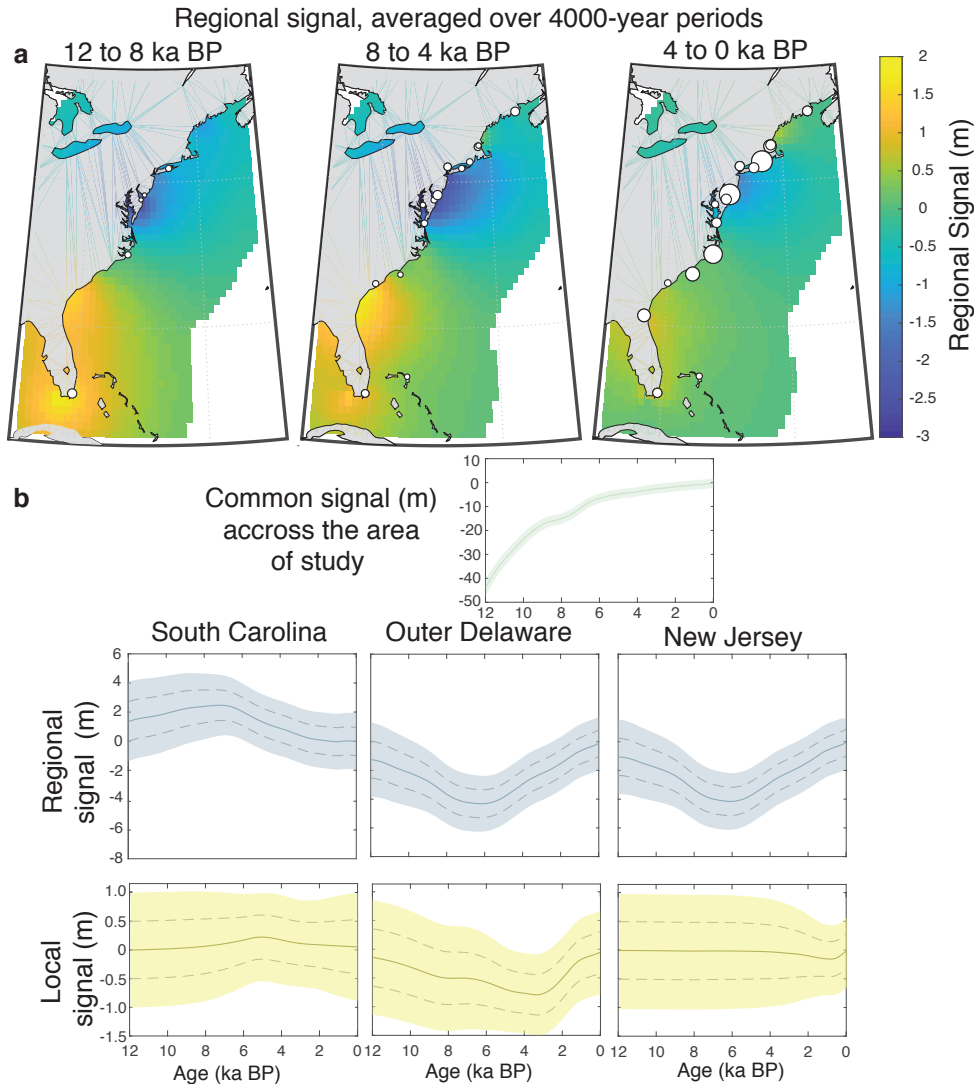


Figure 2.5: (a) Maps of the regional RSL signal, averaged over 4000-year periods, and (b) common, regional, and local terms over time in South Carolina, Outer Delaware, and New Jersey

terms can be separated and analyzed (Figure 2.5), resulting in maps of the spatio-temporal signal for each term (Figure 2.5a) and plots of each term for specific sites. The common signal (which is uniform over the entire domain) absorbs a majority of the signal (Figure 2.5b), whereas the regional and local signals explain the variation between sites. The higher RSL heights along the southern coast in the early- and mid-Holocene (12ka to 4ka) are evident in the maps and in the regional curve for South Carolina (Figure 2.5b). The Outer Delaware and New Jersey sites have lower regional signals, and the differences in these two sites is represented in the local signal (Figure 2.5b).

In some cases, borrowing hyperparameter learning from multiple sites, through optimization

of hyperparameters in a spatio-temporal model, is valuable. When the processes influencing the sites are known to be similar during a period of time, adding a spatial component to a model can add useful information (Figure 2.4). In the particular example here, sharing among sites has led to smoother temporal structure. In the case of the North Carolina record, the spatio-temporal model learns from the overall database that the kyr-scale fluctuations seen in the EIV-IGP fit to the North Carolina data is most likely due to measurement noise.

2.8.3 Estimating spatio-temporal RSL and GMSL from instrumental data (1900 to present)

During the instrumental record, data include satellite altimetry measurements and tide gauges. These data are inherently different from proxy data with negligible temporal error and smaller vertical uncertainties than proxies produce, and thus allow different methods. Estimating GMSL through time and interpolating the spatio-temporal field of RSL change from instrumental records in the past are well-suited to KS and GP model techniques. We implemented both techniques using multiple tide gauge records obtained from the permanent service for mean sea level (PSMSL, 2017; Holgate et al., 2013), with results shown at two sites: Atlantic City, New Jersey, (39.4°N , 74.4°W) and Wilmington, North Carolina (34.2°N , -78.0°W) (Figure 2.6).

Models and implementations

Empirical spatio-temporal GP model (EST-GP): Using a regional subset of tide gauges from the U.S. Atlantic coast (from the same geographic range as the proxy data in Section 2.8.2), we implemented an empirical spatio-temporal GP model (EST-GP). Results include estimates of the spatio-temporal fields of RSL and its rates change with uncertainties along the U.S. Atlantic coast and estimates at two specific sites (Figure 2.6). Although this technique can produce estimates of GMSL (as in Hay et al., 2015), this implementation does not include global results, because it is implemented on a regional subset of data.

KS implementation Using a subset of global tide gauges (see Hay et al., 2015 for further information on the tide gauges used), we implemented the process model in equation 2.13 with a multi-model KS (Section 2.7.5). The KS estimates GMSL and the spatio-temporal fields of RSL

and rates of RSL change along the U.S. Atlantic coast and at specific sites (Figure 2.6).

Results and discussion of KS and EST-GP from 1900 to present

Both techniques can compute posterior estimates of GMSL (Figure 2.6) as well as reconstruct the spatio-temporal sea-level field, conditioned on observed data, but their implementations are very different. The KS approach (Section 2.7.5; described in more detail in Supplemental A.2.2) steps through a forward filtering pass and a backward smoother pass for each time step, enabling computation of the covariance for a smaller subset of points and thus faster solution times (~ 45 seconds for a single KS run at the tide gauge sites only, and ~ 4 hours for the entire multi-model implementation globally). Conversely, the EST-GP conditions on all observations at all time points concurrently. In Hay et al. (2015), both KS and GP implementations use output from physical process models. However, in the current implementation, the EST-GP model has no physical-model input and is purely statistical, based solely on the data. See Hay et al. (2015) for a more complete treatment of these two analytical approaches.

Because of the differences in implementation of the KS and EST-GP, there are some drawbacks and advantages to each. The full covariance matrix (over all space and time points for data and predictions) that is required for the EST-GP makes the resolution of annual tide gauge data difficult to handle when attempting to model these data on a global scale. As a solution, lower-resolution averages can be used as input (Hay et al., 2015). Conversely, the KS becomes unstable during the backward smoothing pass when persistent data gaps are present in the records. The KS therefore requires a subset of tide gauges which ensures observation availability over time.

The spatial field computed by Hay et al. (2017) is less refined because of their modeling choice to compute the global field on a 5° grid. A higher resolution field can be computed with the KS; however, this will be accompanied by longer model run time. Moreover, embedded in the KS spatial maps are DSL fields from several global climate models, and the resolution of the KS reconstruction is limited by the resolution of these models. These physical models have the potential to provide information about processes occurring in the open ocean, far from tide gauge sites, whereas the purely statistical model loses power when moving away from observed data. When less data are available, for example earlier in time because the tide gauges are sparse, the KS predicts a much

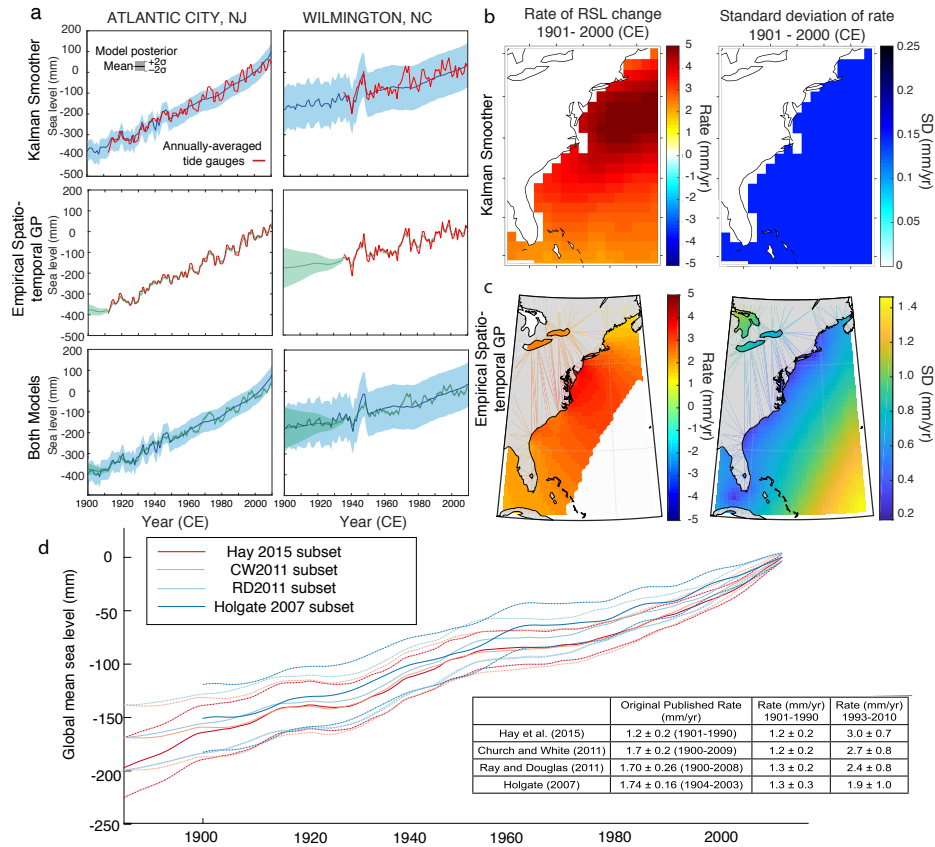


Figure 2.6: Comparison of KS and EST-GP predictions at (a) two sites based on annually-averaged tide gauges, which are shown in red. Both models include a spatial component and produce maps of RSL rates of change, for the (b) KS and (c) EST-GP. (d) GMSL time series obtained using the KS applied to subsets of tide gauges from previous studies, with 1σ uncertainties (Hay et al., 2017).

rougher sea-level time series for each location, despite the fact that there are tide gauges at these particular sites, whereas the EST-GP has larger uncertainties when there are no tide gauges as input at a specific site (Figure 2.6a).

The KS model has also been tested on various subsets of tide gauges (Church and White, 2011; Holgate, 2007; Ray and Douglas, 2011), which can slightly influence the results (Figure 2.6d, Hay et al., 2017). However, the results with a single technique are more similar than when the data and technique are both different. When the research question relates to estimating GMSL, fully Bayesian methods may be too computationally intensive for the datasets; however, ad hoc (Section 2.7.2) choices may lead to different conclusions than the KS or GP techniques, especially when analyzing different sets of instrumental data.

GMSL reconstructions from a combination of proxy and instrumental data are possible using

empirical Bayesian analysis, although they have rarely been implemented. Kopp et al. (2016) provide the only example of using both instrumental and proxy data to construct an empirical GMSL reconstruction over the past 3000 years using spatio-temporal modeling with empirical Bayesian analysis (Figure 2.7). They find a robust GMSL fall from 1000–1400 CE and a 20th century rise at a rate that is unprecedented in at least 2800 years. The pattern of GMSL seems to have a lot of variability through the Common Era; however, this is due to several modeling choices, including that the model is conditioned on the assumption that mean GSS over -100–100 CE is equal to mean GSL over 1600–1800 CE to focus on submillennial variations. (see Kopp et al. 2016 for additional details).

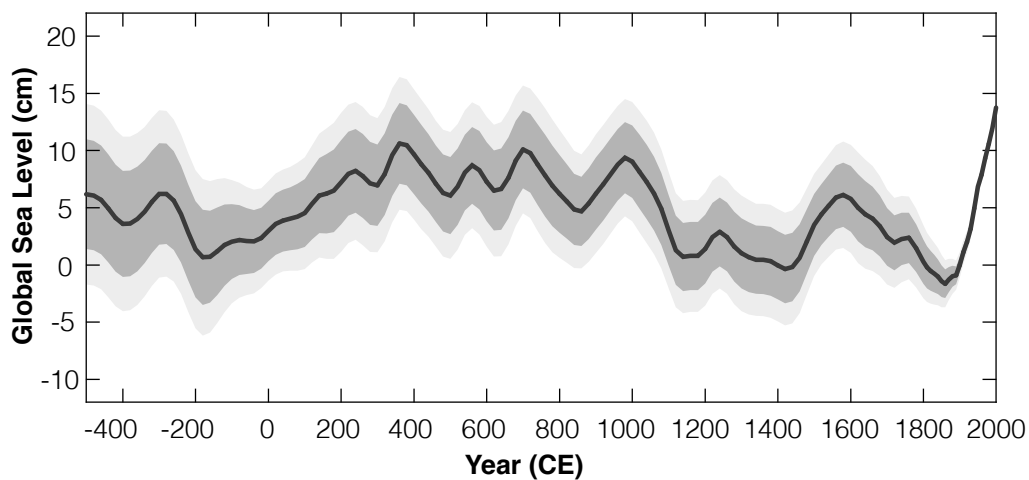


Figure 2.7: GMSL estimate over the last ~ 2500 years from Kopp et al. (2016) using a model with GP priors, applied to RSL proxy data and instrumental data in an empirical Bayesian analysis.

2.9 Conclusions

Hierarchical statistical modeling frameworks provide a transparent approach for separating modeling choices at the data and process level from analysis choices. Appropriate modeling and analysis choices in sea-level research depend on the type of data and the scientific question(s) being addressed. Estimating past GMSL requires techniques that account for the physics or geometry of the contributing processes. For example, Kalman smoother techniques are especially valuable for estimating GMSL and RSL over the instrumental period. Because the KS is recursive, one of its benefits is computationally enabling analysis of data at a higher temporal resolution (e.g., yearly)

compared to other methods. Conversely, this approach is poorly suited to proxy data that have temporal uncertainties, and therefore cannot in current implementations be used to reconstruct trends over longer timescales. Alternative methods, including EIV and NIGP, have been implemented within GP models to incorporate temporal uncertainties. However, the use of full covariance matrices within GP models may restrict estimation to lower temporal resolutions (e.g., decadal), particularly when using instrumental data and for large datasets. There are several approximation and estimation techniques in the GP and machine-learning literature that have not yet been applied in a sea-level context, such as reduced-rank approximation (Gabriel and Zamir, 1979) and variational inference (Blei et al., 2017), which could speed up analyses and improve resolution with large datasets.

Another related goal in sea-level research is identifying accelerations in rates of RSL and GMSL change (e.g., Church and White, 2006; Jevrejeva et al., 2008; Kopp, 2013). Although change-point regression attempts to address these types of questions, the inherent assumptions that RSL or GMSL is piecewise linear can be restrictive. Non-parametric models with statistically robust methods for calculating GMSL and estimating RSL, such as KS or GP models, can help answer questions about acceleration in a manner that recognizes that acceleration may occur gradually rather than abruptly.

Identifying the physical processes that explain patterns of spatial variability in RSL is a further objective of the sea-level community. Spatio-temporal approaches are required to address this problem in a manner that allows rigorous comparisons between sites. Current methods incorporate different processes through physics-based models (as in Hay et al., 2015) or by reconstructing the sea-level field statistically and compare it to the relevant physics-based models (e.g., atmosphere-ocean global circulation models on recent timescales with higher resolution records, or GIA over longer periods with lower resolution data).

Improving estimates of GIA is a related goal to explaining spatial variability because it is the dominant driver of spatial variability in RSL change over Holocene timescales (Peltier et al., 2015). Traditionally, this is done through an iterative, manual process, where data from specific sites are compared to different versions of physical GIA models. However, alternative approaches include using a suite of GIA models (Hay et al., 2015) or using a single GIA model as a mean prior

estimate and fitting the mismatch with a Gaussian process (e.g., Kopp et al., 2016; Vacchi et al., in review). The latter approach enables further constraints on the role of spatially-variable GIA, while appropriately characterizing uncertainties.

An important area of development for statistical sea-level models is more comprehensive and accurate use of data. Most proxies do not conform to normal distributions, so techniques for incorporating non-Gaussian likelihoods, such as integrating transfer functions into spatio-temporal models, have the potential to make use of previously underutilized proxies. The development of transfer functions is now a widely researched topic in the general field of palaeoclimate reconstruction (e.g., Ohlwein and Wahl, 2012 for pollen, Tolwinski-Ward et al., 2011 for tree rings, Hughes et al., 2002 for pollen, Zong and Horton, 1999 for diatoms, Guilbault et al., 1996 for forams). A general approach has been developed by Parnell et al. (2015), which readily applies to RSL. Although they are usually carried out prior to process modeling, integrating transfer functions into full statistical models (e.g., Cahill et al., 2016) is a key goal for the next generation of palaeo-RSL models. Another example of valuable information, which is underutilized to date, is field data indicating the rate or direction of change of sea-level (e.g., stratigraphic context). Quantitatively incorporating this information into statistical models would enhance future estimation and prediction of the sea-level field.

Identifying future directions for growth in statistical models could inform the standardization and treatment of data collection and database structures, all of which are required for advanced statistical methods in the present. Data compilation efforts (e.g., Düsterhus et al., 2016) aim to standardize and synthesize RSL data, which will enhance the comparability and accessibility of information to improve both physical models and statistical reconstructions. The accuracy and consistency of all statistical models will be enhanced when databases are standardized. Currently, the challenge of standardization often falls to the authors of individual statistical studies. However, progress will be faster if standard protocols and database formats are applied as a routine matter.

Over the last decade, the tools used to conduct inference have greatly advanced, making more analytical and modeling choices available to address different questions. Spatio-temporal statistical modeling is an active area of research, which will benefit from further interdisciplinary collaboration. Formalizing a hierarchical statistical framework for sea-level analysis and standardizing the data

used for RSL reconstructions brings clarity to problems and potential future advancements in paleo-sea-level modeling.

2.10 Glossary

Table 2.2: Definitions of relevant terms

Term	Meaning
<i>analysis choices</i>	decisions in how to implement a specific model structure (e.g., least-squares, likelihood maximization, empirical Bayesian analysis, fully Bayesian analysis (MCMC), Kalman Smoother, ad hoc, EIV, NIGP)
<i>BHM</i>	Bayesian Hierarchical Model; uses fully Bayesian analysis, which approximates complicated distributions through sampling, usually using MCMC sampling
<i>conditional probabilities</i>	the distribution of a random quantity, given a particular value of another (unknown) random quantity; express uncertainties in hierarchical models
<i>conjugate prior</i>	prior distribution that comes from the same family of distributions as the likelihood distribution, so as to enable an analytically tractable solution for the posterior
<i>continuous core</i>	near-continuous records from a single core of salt-marsh sediment or a single coral head
<i>covariance function</i>	function defining prior beliefs about the relationship between one or more variables in a Gaussian process, as a measure of how much they change together
<i>EHM</i>	Empirical Hierarchical Model; uses empirical Bayesian analysis, which estimates parameters with point estimates, usually by maximizing their likelihoods, as opposed to a BHM, which samples the prior distributions on parameters
<i>EIV</i>	errors-in-variable framework; accounts for the measurement error in the independent variables by assuming that errors in both variables are independent of one another

<i>EIV-IGP</i>	errors-in-variables integrated Gaussian process model; implements a temporal model of the rate of RSL change, deriving the RSL curve from the rate curve; incorporates uncertainty in the independent (time) variable and the dependent variable through EIV framework
<i>EOF</i>	empirical orthogonal function; technique used to find the dominant spatial patterns in a dataset; when analyzing sea level, used to find the dominant patterns in SSH from satellite altimetry measurements and apply to tide gauges in order to estimate GMSL change
<i>error</i>	the difference between a measurement and the true value, for a particular data point; one can model the error as a random draw from an uncertainty distribution
<i>EST-GP</i>	empirical spatio-temporal Gaussian process model; model with Gaussian process priors, which incorporates spatial and temporal covariance functions to produce the fields of RSL and rate of RSL change as maps; solved using an empirical methodology that maximizes the likelihood of the model conditional upon the parameters of the prior
<i>ET-GP</i>	empirical temporal Gaussian process model; model using Gaussian process priors, which is independent in space (no spatial component) and solved using an empirical methodology that maximizes the likelihood of the model conditional upon the parameters of the prior
<i>GP</i>	Gaussian process; a generalization of the multi-variate Gaussian distribution to continuous time (and space), which is fully defined by its mean function and covariance function; GP regression provides an analytically tractable solution when adopting the assumption of normality for all distributions
<i>heteroscedasticity</i>	heterogeneous (unequal) errors
<i>hyperparameter</i>	parameter of a prior distribution
<i>hyperprior</i>	prior distribution on a hyperparameter
<i>index point</i>	discrete data that constrain RSL at a single point in time and space
<i>inferential uncertainty</i>	the error that arises from the data-generation process from true RSL to the creation of a RSL proxy

<i>KS</i>	Kalman Smoother; iterative method that comprises a forward filtering pass and a backward smoother pass; used in a multi-model implementation to compute posterior estimates of GMSL and spatio-temporal RSL fields, conditioning prior estimates from physical models of several processes on observations
<i>latent</i>	unobserved or hidden (e.g., the true values of RSL)
<i>likelihood</i>	the probability of observing the data as described by the fitted model; also known as the sampling or data distribution; a conditional distribution that is a function of unknown parameters for observed data and incorporates the form of uncertainty in the data (e.g., measurement and/or inferential)
<i>marginal distribution</i>	unconditional probability distribution of a random quantity, found by integrating over all values of the conditional distribution in Bayesian analyses
<i>MCMC</i>	Markov Chain Monte Carlo techniques; methods used to generate random variables, perform complicated calculations, and simulate complicated distributions through sampling in Bayesian hierarchical models (common algorithms include Gibbs sampling, Metropolis-Hastings, Metropolis within Gibbs, importance sampling)
<i>modeling choices</i>	decisions that define the relationships in a model, usually at the process level; in sea-level analysis, the relationship between time, space and RSL (e.g., linear, polynomial, change-point, GP (integrated), incorporation of physical models)
<i>NIGP</i>	noisy-input Gaussian process method; a method for incorporating uncertainty in the independent variable within a Gaussian process model; using a Taylor expansion about each input point to recast input noise as output noise proportional to the squared gradient of the GP posterior mean (McHutchon and Rasmussen, 2011); in sea-level analysis, geochronological uncertainty is recast as proportional error in RSL
<i>noise</i>	error; statistical noise refers to unexplained variation or randomness
<i>noisy data</i>	error-prone data that have been corrupted by known or unknown processes
<i>non-parametric</i>	not involving any assumptions as to the functional form

<i>posterior distribution</i>	the probability distribution of an unknown quantity, conditional on observed data; in sea-level analysis, estimates (for example) the true RSL time series or field of RSL with uncertainties, given proxy or instrumental data
<i>prior distribution</i>	the information about an uncertain parameter that is combined with the probability distribution of new data to yield the posterior distribution; can be subjective, based on a priori beliefs, or noninformative, which minimizes the impact on inference
<i>uncertainty</i>	parameter characterizing the range of values within which a measured value can be said to lie with a specified probability
<i>white noise</i>	serially uncorrelated random variation (zero mean and finite variance)

Chapter 3

A statistical framework for integrating non-Gaussian proxy distributions into geological reconstructions of relative sea level

By Erica L. Ashe¹, Nicole Khan², Lauren Toth³, Andrea L. Dutton⁴, and Robert E. Kopp¹

¹*Rutgers University*, ²*Nanyang Technological University*, ³*United States Geological Survey*, ⁴*University of Florida*

Abstract

Robust, proxy-based reconstructions of sea-level change are critical to discerning the processes that drive variability in relative sea level (RSL); however, these reconstructions rely on the ability of statistical models of RSL to accurately constrain the relationship between the proxy and sea level. These relationships can be complex, and are often poorly described by traditional methods that assume Gaussian distributions. We develop a new statistical framework to estimate past sea-level change based on the modern distributions of RSL proxy elevations in relation to sea level, using corals as an illustrative example. The new statistical framework is hierarchical and comprises 1) data, 2) process, and 3) parameter levels. In a case study based on coral archives, the data level describes each observed proxy's elevation and geochronological uncertainty from field and laboratory measurements and uses modern depth distributions of individual coral taxa to infer the likelihood of RSL, given the observed proxy elevations. The process level uses the full temporal covariance to model RSL through time. The parameter level dictates prior expectations regarding the temporal correlation structure of RSL. Using MCMC sampling, we approximate the posterior distributions on these parameters and RSL, conditioned on the observed data. We find that incorporating the non-parametric empirical distributions of coral taxa in models of RSL in south Florida produces robust and realistic estimates of RSL and its uncertainty through time.

3.1 Introduction

Far-field (i.e., distal to ice sheets) records of RSL change derived from low-latitude locations are critical for constraining physical processes that drive sea-level change; however, records from these regions are sparse due to the limited availability of reliable relative sea level (RSL) proxy records (e.g., Milne et al., 2005; Woodroffe and Horton, 2005; Woodroffe et al., 2015). Realistically characterizing the relationships between proxy records and RSL is vital to constraining the geophysical and oceanographic processes that control RSL changes over a variety of spatial and temporal scales. Using proxy records to quantify RSL and the rates of RSL change in the past can help to determine the role that these processes may play in the present and in the future. For example, the geologic record from previous interglacial periods can provide insight into potential ice-sheet instabilities under conditions analogous to our presently warming climate (Dutton and

Lambeck, 2012; Dutton et al., 2015; DeConto and Pollard, 2016). Similarly, periods of deglaciation reveal short intervals of acceleration in RSL rise, termed ‘meltwater pulses’ (e.g., Bard et al., 1990; Yokoyama et al., 2000; Abdul et al., 2016; Renema et al., 2016; Blanchon, 2017), which may provide insight into non-linear, or abrupt changes, in ice-sheet volume (e.g., Abdul et al., 2016). Reconstructions of RSL from more stable periods, like the middle-to-late Holocene, reveal internal variability that modulates local- to regional-scale processes (Engelhart et al., 2009; Kopp et al., 2016; Khan et al., 2017). Although reconstructions of past RSL change are central to understanding modern sea-level variability, the quality of the information that can be uncovered from geologic archives is constrained by the accuracy and precision of the RSL proxy records they yield.

Many RSL models (Khan et al., 2017; Hay et al., 2015; Cahill et al., 2016; Kemp et al., 2014) assume that the relationship between RSL and an individual proxy data point’s elevation follows a normal distribution, an assumption that does not accurately represent the observed distribution of many proxies with respect to RSL. For example, Khan et al. (2017) and Kopp et al. (2009) used a normal distribution to approximate an assumed uniform distribution for the coral records used in their models. Meltzner et al. (2017) and Kopp et al. (2009) treated other corals as lower (marine) limits on RSL, and Khan et al. (2017) excluded *A. palmata* from their statistical modeling. Our aim is to develop a method for incorporating modern depth distributions from empirical observations into a statistical framework for estimating RSL. Using individual coral taxa as examples of RSL proxies that have non-Gaussian relationships with sea level (Hibbert et al., 2016; Blanchon et al., 2009; Camoin and Webster, 2015), we implement an approach that is compatible with previous models used in spatio-temporal hierarchical modeling of RSL.

Early coral-based reconstructions of past RSL from the Caribbean (e.g., Lighty et al., 1982; Bard et al., 1990) relied primarily on a single taxon, *A. palmata*, which was the dominant coral in the regional fossil record from reef-crest environments throughout the late Quaternary (Budd et al., 1994; Kuffner and Toth, 2017; Renema et al., 2016). Drawing on the assumption that *A. palmata* predominantly occurred within five meters of the sea surface, these corals have been used as estimates of “minimum” sea-level height (e.g., Lighty et al., 1982; Toscano and Macintyre, 2003) and more recently, as quantitative indicators of millennial-scale RSL variability (e.g., Khan et al., 2017). Combining *A. palmata* records with more precise RSL proxy records, such as mangrove peat (Toscano and Macintyre, 2003), records from additional coral taxa (Blanchon and Shaw, 1995; Peltier and Fairbanks, 2006; Abdul et al., 2016), or other sedimentary or geomorphic records not traditionally incorporated into multi-proxy reconstructions has the potential to increase both the accuracy and precision of RSL estimates.

Many RSL studies in the circum-Caribbean region have focused on *A. palmata* because of the relatively large paleodepth uncertainty of most other coral taxa compared to other RSL proxy types (Camoin and

Webster, 2015). It is because of the relatively high uncertainty of coral-based RSL proxies that accurately constraining the relationship of corals to RSL is so important. Few RSL studies (see Hibbert et al., 2016; Stanford et al., 2011 for exceptions) have attempted to systematically quantify the distributions of other coral taxa with depth using modern observational datasets. One challenge to doing this is that coral depth distributions can vary significantly based on a myriad of factors that may depend on geography (Hibbert et al., 2016). Although Hibbert et al. (2016) used Markov Chain Monte Carlo (MCMC) sampling to estimate RSL at single points in time from taxon-specific coral depth distributions empirically, they stopped short of inferring a sea-level curve or rates of RSL change with time-series statistical methods. Austermann et al. (2017) used the empirical distributions of Hibbert et al. (2016) to constrain dynamic topography signals, but still treated the records as uncorrelated over time. Stanford et al. (2011) inferred a sea-level curve, combining multiple RSL proxy records from various sites using non-Gaussian distributions applying a spline smoothing function to estimate a probabilistic sea-level curve. They assumed far-field sites at low latitudes represented the same signal, precluding a spatio-temporal implementation. Through the use of Gaussian processes (GP) priors with covariance functions, the framework we present here can be easily adapted to include multiple sites with spatial correlations.

We build upon the models of Khan et al. (2015, 2017) and Kopp et al. (2016) and the analysis of Hibbert et al. (2016) in a hierarchical statistical framework. We first compile and fit probability distributions to data comprising the modern occurrences of various coral taxa by depth. We then construct a hierarchical statistical model and use MCMC sampling to condition Gaussian process (GP) prior probability distributions on the non-Gaussian likelihoods (the modern fitted distributions) of RSL proxy records. To evaluate its performance and sensitivity to various types of data and uncertainties, we apply the model to Holocene records of coral and sedimentary archives from south Florida. Although we use the example of corals to implement the modeling framework, our method could be applied to any sea-level proxy that has a non-Gaussian relationship to sea level.

3.2 Methods

The International Geological Correlations Programme (IGCP) projects 61, 200, 495 and 588 (e.g., van de Plassche, 1986; Hijma et al., 2015) endorsed a universal approach to reconstruct RSL histories from different locations and environments with quantified age and RSL uncertainty terms inherent in inference and measurement (e.g., van de Plassche, 1986). We employ this approach (briefly described below) in a hierarchical statistical framework, which partitions uncertainties among model levels.

Geological proxy records for RSL are derived from sediments, fossils, and morphological and archeological features, the formation of which were controlled by the past position of RSL (Shennan, 2015). These proxy

records possess a systematic and quantifiable relationship to elevation with respect to a tidal datum (e.g., mean sea level [MSL]). The relationship of a proxy record to sea level, known as the proxy’s *indicative meaning*, is defined by 1) a *reference water level*, which is the central tendency (e.g., mean or median) of the distribution of the proxy record with respect to a tidal datum, and 2) an *indicative range*, which describes the uncertainty in the vertical distribution of the proxy record.

Dated RSL proxies record the past position of RSL as

$$RSL = E - RWL, \quad (3.1)$$

where E is the elevation of the proxy record and RWL is the proxy’s reference water level (Hijma et al., 2015). Each sample has unique uncertainty estimates, where its age uncertainty is based on inferential and measurement uncertainties associated with the method used to date the sample (e.g., laboratory and calibration uncertainties for radiocarbon-dated samples), and its RSL uncertainty stems from uncertainties in interpretation of the distribution of the proxy in relation to RWL (i.e., δ , indicative range or sometimes referred to as inferential uncertainty) and measurement of E (i.e., ε) in Equation 3.2. When reconstructing RSL, the uncertainties are combined by summing their variances to estimate the total uncertainty variance. This relationship can be statistically formalized by adding terms for the errors inherent in the observation of a proxy record, such that:

$$RSL_i \begin{cases} = E_i - RWL_i + \varepsilon_i + \delta_i \\ > E_i - RWL_i + \varepsilon_i + \delta_i \\ < E_i - RWL_i + \varepsilon_i + \delta_i, \end{cases} \quad (3.2)$$

where the observed RSL proxy record is indexed by i , ε is the measurement error, and δ is the error associated with the proxy record’s indicative range. Two types of RSL proxy records are identified: 1) index points, which record the unique (or discrete) position of RSL in space and time, and 2) limiting data, which define an upper (terrestrial) or lower (marine) bound on RSL at a given point in space and time.

To incorporate the IGCP approach into a hierarchical statistical framework, we first fit parametric probability distributions to the modern depth occurrences of individual coral taxa to describe their indicative meanings (Section 3.2.2). These parametric probability distributions are incorporated in the hierarchical statistical model, which accommodates measurement and inferential data uncertainties in its different levels (Section 3.2.1). We implement the model (Section 3.2.2) and test its performance given different data types with a case study of south Florida sea-level archives (Section 3.2.3).

3.2.1 Statistical model structure

The goal of our analysis is to determine the probability distribution of RSL (\mathbf{f}) through time, based on the observed elevations ($\hat{\mathbf{y}}$) of proxy data points and their estimated ages ($\hat{\mathbf{t}}$). Using hierarchical modeling, we explicitly distinguish between three levels: (1) a data level, (2) a process level, and (3) a parameter level. The data level describes $p(\hat{\mathbf{y}}, \hat{\mathbf{t}} | \mathbf{z}, \mathbf{t}, \Theta_d)$, the probability of the measured elevations $\hat{\mathbf{y}}$ and times $\hat{\mathbf{t}}$ of the proxies, conditional upon sample-wise noisy RSLs \mathbf{z} , true times \mathbf{t} , and data-model parameters Θ_d . The data model characterizes the way in which RSL is recorded by different proxies according to their modern depth distributions, measurement errors, and dating errors. The process level describes $p(\mathbf{f}, \mathbf{t} | \Theta_s)$, the probability of true RSL \mathbf{f} at true time \mathbf{t} conditional upon the process-level hyperparameters Θ_s . The parameter level characterizes key attributes (Θ_s) of the process level.

We use Bayesian analysis (Cressie and Wikle, 2015) to infer all unknown quantities (including RSL, its uncertainty, and parameters within the model), as described in the model implementation (Section 3.2.2). Throughout, we use italicized variables to represent scalars (e.g., the elevation of a single observation) and bold variables to represent vectors (e.g., the elevations of all observations). The variables used throughout the statistical analyses are summarized in Table 3.1.

Table 3.1: Definitions of all relevant notation in the model

Variable	Definition
i	indexes the observed proxy elevations and ages, as well as their uncertainties
j	indexes the type of proxy (e.g., coral taxa) and thus its likelihood distribution, which is common to all proxies of that type
\mathbf{f}	true, unobserved RSLs, which have a prior relationship with \mathbf{t} characterized by fixed parameters Θ_s
\mathbf{z}	sample-wise, noisy RSLs corresponding to each observation (produced in the sampling module) after accounting for the relationship between elevation and RSL as well as the correlations in time from the sea-level processes
\mathbf{y}	true, unobserved elevations
\hat{y}_i	noisy, observed elevation
\mathbf{t}	true, unobserved ages
\hat{t}_i	estimated age, based on radiocarbon dates (midpoint of calibrated age)
μ_j	log mean (for log-normal) or mean (for normal) parameter of the likelihood distribution for proxy type j
σ_j	log standard deviation (for log-normal) or standard deviation (for normal) parameter of the likelihood distribution for proxy type j
ε_i	standard deviation of elevational measurement uncertainty for observation i
τ_i	standard deviation of age uncertainty for observation i
Θ_d	data-level parameters $\{\mu_j, \sigma_j, \varepsilon_i, \tau_i\}$ for all proxy types j and all observations i , which are estimated in the distribution-fitting module
Θ_s	process-level hyperparameters $\{\alpha_m, \beta_m, \alpha_w\}$, which are approximated in the sampling module
k	minimum probability constant

We create a Bayesian hierarchical model to estimate the posterior distribution of RSL and parameters

given observed data:

$$\begin{aligned}
 & \underbrace{p(\mathbf{f}, \mathbf{t}, \Theta_s, \mathbf{z} | \hat{\mathbf{y}}, \hat{\mathbf{t}}, \Theta_d)}_{\text{posterior}} \propto \tag{3.3} \\
 & \underbrace{p(\hat{\mathbf{y}} | \mathbf{z}, \Theta_d) \times p(\hat{\mathbf{t}} | \mathbf{t}, \Theta_d)}_{\text{data model}} \times \underbrace{p(\mathbf{z} | \mathbf{f}, \mathbf{t}, \Theta_d) \times p(\mathbf{f}, \mathbf{t} | \Theta_s)}_{\text{process model}} \times \underbrace{p(\Theta_s)}_{\text{parameter model}}
 \end{aligned}$$

Before we describe each component of the model, we follow Parnell et al. (2015) and Cahill et al. (2016) in making some simplifying assumptions. As described in Section 3.2.2, we assume that the data model parameters can be estimated by the modern data and that all measurement errors can be estimated by the uncertainties (temporal and elevational) defined in the collection of the data. We also assume that the relationship between RSL and the elevation of each proxy is independent of the RSL process. We define three modules—a distribution-fitting module, a sampling module, and a sample-wise prediction module—which are implemented in succession and described in more detail in Section 3.2.2:

$$p(\mathbf{z}, \Theta_s | \hat{\mathbf{y}}, \hat{\mathbf{t}}, \Theta_d) \propto p(\hat{\mathbf{y}} | \mathbf{z}, \Theta_d) \times p(\mathbf{z} | \mathbf{f}, \mathbf{t}, \Theta_d) \times p(\mathbf{f}, \mathbf{t} | \Theta_s) \times p(\hat{\mathbf{t}} | \mathbf{t}, \Theta_d) \times p(\Theta_s) \tag{3.4}$$

$$p(\mathbf{f}, \mathbf{t}, \Theta_s, \mathbf{z} | \hat{\mathbf{y}}, \hat{\mathbf{t}}, \Theta_d) \propto p(\mathbf{z}, \Theta_s | \hat{\mathbf{y}}, \hat{\mathbf{t}}, \Theta_d) \times p(\hat{\mathbf{t}} | \mathbf{t}, \Theta_d) \times p(\mathbf{f}, \mathbf{t} | \Theta_s) \tag{3.5}$$

The distribution-fitting module is implemented through the ‘fitdist’ function in MATLAB. The sampling module (equation 3.4) is implemented through MCMC sampling, resulting in a conditional posterior distribution on \mathbf{z} and Θ_s . We then use the approximation of $p(\mathbf{z}, \Theta_s | \hat{\mathbf{y}}, \hat{\mathbf{t}}, \Theta_d)$ from the sampling module in the sample-wise prediction module (equation 3.5) to infer true RSL over true time through the noisy input Gaussian process (NIGP) method of McHutchon and Rasmussen (2011). These modules are outlined after defining the levels of the hierarchical model in detail.

Data level

The data level includes the observed elevation \hat{y}_i of each RSL proxy data point with measurement uncertainty. This level characterizes the relationship between these elevations and noisy RSL \mathbf{z} , as well as between true age t_i and interpretation of age, \hat{t}_i .

We make the simplifying assumption that vertical measurement uncertainty in RSL proxies is independent and normally distributed, such that:

$$\hat{y}_i | y_i, \varepsilon_i \sim \mathcal{N}(y_i, \varepsilon_i^2), \tag{3.6}$$

where y_i is true (unobserved) elevation and ε_i is the standard deviation of measurement uncertainty for

observation i .

We make the simplifying assumption that age uncertainty in RSL proxies is independent and normally distributed, such that:

$$\hat{t}_i | t_i, \tau_i \sim \mathcal{N}(t_i, \tau_i^2), \quad (3.7)$$

where \hat{t}_i is the midpoint of the calibrated age and t_i is the true (unobserved) age of observed record i and τ_i is the standard deviation of the temporal measurement uncertainty defined in the dating process (Section B.6.6). Age uncertainties are incorporated using the noisy-input GP method of McHutchon and Rasmussen (2011), which translates errors in the independent variable (time) into equivalent errors in the dependent variable (proxy elevation) (Section B.2).

The model can accommodate both parametric and nonparametric fitted distributions as likelihoods, which characterize the relationship between the measured elevation of the RSL proxy \hat{y}_{ij} and the sample-wise, noisy RSL z_i for each observation i of proxy type j . Unobserved z_i is an intermediate variable, which is created within the sampling module and is conditioned on all other sample-wise, noisy RSLs, in addition to being conditioned on the observed elevation \hat{y}_{ij} . In the case study of south Florida, analysis of the modern distributions of coral taxa with depth are defined with both nonparametric likelihoods and distinct functional forms of likelihood distributions, which are based on the modern depths of distinct coral taxa and indicative meanings of sedimentary proxies (Section 3.3.1): kernel, log-normal, normal, censored/upper-limiting, and censored/lower-limiting.

Each coral taxa is fit to a nonparametric empirical distribution (see section 3.2.2), determined by its modern depth data, such that:

$$z_i - \hat{y}_{ij} | z_i, \text{modern data} \sim \text{empirical pdf} \quad (3.8)$$

where the pdf is given by the fitted distribution found using the ‘fitdist’ function in MATLAB (using a kernel density with bandwidth = 0.15 and positive support).

Because the populations of many organisms closely track an optimal suite of environmental conditions that vary with respect to sea level, the distributions of many species follow log-normal distributions (e.g., Brown, 1984). Although the non-parametric distributions provide the best fit to the empirical data, we additionally fit the modern coral taxa to log-normal distributions (see section 3.2.2), such that for taxon $j \in \{1, 2, \dots, 10\}$:

$$z_i - \hat{y}_{ij} | z_i, \mu_j, \sigma_j \sim \mathcal{LN}(\mu_j, \sigma_j^2) \quad (3.9)$$

where \mathcal{LN} signifies the log-normal distribution and scale and shape parameters (μ_j and σ_j ; the mean and standard deviation of the log of the distribution) are estimated for each taxon j (Section 3.2.2) and are in

the vector of data parameters Θ_d .

Mangrove peats are assumed to form between MTL (mean tide level) and HAT (highest astronomical tide) in a normal distribution with mean μ and standard deviation σ based on the indicative meaning of mangrove peat and local tidal levels (Khan et al., 2017; Section B.6.6). A coral taxon with a fitted normal depth distribution (i.e., the Caribbean-wide distribution for *Orbicella* spp.) takes the same form, but with mean μ and standard deviation σ estimated from its modern depth distribution. For both normally distributed coral taxa records and mangrove peat records (records indexed by i , this relationship is defined as:

$$\hat{y}_{ij} - z_i | z_i, \mu_j, \sigma_j \sim \mathcal{N}(\mu_j, \sigma_j^2) \quad (3.10)$$

when the proxy type j is assumed to follow a normal distribution. For mangrove peat index points, μ_j is always positive because the mangrove peat grows above RSL, whereas for normally distributed corals, μ_j is always negative because corals grow below RSL.

Marine-limiting and freshwater-limiting data define lower and upper limits on sea level, respectively, where the relationship between \hat{y} and z takes the following form:

$$p(\hat{y}_{ij} | z_i) \propto \begin{cases} 1, & \text{for marine limiting, if } \hat{y}_{ij} \leq z_i \\ \tau_i \cdot k, & \text{for marine limiting, if } \hat{y}_{ij} > z_i \end{cases} \quad (3.11)$$

$$p(\hat{y}_{ij} | z_i) \propto \begin{cases} 1, & \text{for freshwater limiting, if } \hat{y}_{ij} \geq z_i \\ \tau_i \cdot k, & \text{for freshwater limiting, if } \hat{y}_{ij} < z_i \end{cases} \quad (3.12)$$

where k is a minimum probability constant, which is multiplied by the standard deviation of the age uncertainty τ_i to account for uncertainty in the depositional age of the limiting data. Just as the noisy input Gaussian process recasts age uncertainty as RSL uncertainty, the limiting data distributions much also account for age uncertainty. This is accomplished with the minimum probability constant. Because the precise date the proxy was living above/below the water is unknown, k is used to permit the unobserved sample-wise RSL z_i to take on values above marine limiting elevations and below terrestrial limiting elevations, proportional to the uncertainty in age of a given record. We use the proportionality constant to provide a constraint on the data at the calibrated date, one point in time, to account for this uncertainty over likely age of the observation with age uncertainty. In order to allow slight flexibility in these limiting constraints, because of the age uncertainty of the observed proxy record, we assigned a value of 1×10^{-4} to k . This enables more flexibility when there is less precision in a given observation.

We maintain the simplifying assumption of conditional independence among observed elevations $[p(y_1 | z_1) \perp$

$p(y_2|z_2)$] and among calculated ages $[p(\hat{t}_1|t_1) \perp p(\hat{t}_2|t_2)]$, although there is clearly a correlation at the process level in the underlying RSL. In other words, the relationship between sea level and the elevation of one observation does not affect that relationship for any other observation. The same is true for age uncertainties. The assumed independence may not strictly hold in all cases (e.g., measurements in a sediment core, where elevation estimates may be correlated). However, most samples in these types of analyses are not collected from the same core, therefore, they are independent with respect to age, and the law of superposition does not apply here (or in highstand locations). If the elevation estimates were correlated because they came from a single core such that an age model were used, however, we would use the law of superposition to inform these estimates.

Process level

True RSL is modeled at the process level:

$$f(t) = m(t) + w(t) \quad (3.13)$$

where $m(t)$ is a medium-frequency non-linear signal, and $w(t)$ is a white-noise process, which captures high frequency variability. The medium-frequency signal is modeled with a mean-zero Gaussian process prior distribution:

$$m(t) \sim \mathcal{GP}\{0, \alpha_m^2 \rho(t, t'; \beta_m)\}, \quad (3.14)$$

where ρ is a Matérn correlation function with a smoothness parameter of $3/2$ (Rasmussen and Williams, 2006), which ensures that the function is once-differentiable, α is the amplitude, and β is the characteristic time scale for each term. The white noise term has a standard deviation of α_w , and captures sea-level variability at temporal scales shorter than those characterized $m(t)$. These hyperparameters are described at the parameter level (Section 3.2.1).

Parameter level

At the parameter level of the model $\Theta_s = [\alpha_m, \beta_m, \text{ and } \alpha_w]$ represent the hyperparameters that characterize the process level of the model, where α_m represents the amplitude of the sea-level process, β_m represents the characteristic time-scale of variability, and α_w is the amplitude of the white noise term $w(t)$. We use MCMC sampling to approximate the posterior distributions of each of the parameters, conditional on the observed proxy records. We restrict the bounds of the amplitude and temporal scale proportionally, based on the ratio of magnitude of RSL change during the Holocene epoch, such that the amplitude parameter may take on values between 5 and 30 meters, and the temporal scale parameter may take on values between

4 and 40 ky. We restrict the bounds on the white-noise amplitude according to the average uncertainties on the proxy elevations, with a maximum value of 4 meters. Subject to these bounds, each parameter is assigned a uniform prior distribution.

When implementing with parametric distributions, $\Theta_d = [\mu_j, \sigma_j]$ (for $j \in \{1, \dots, q\}$, where q is the number of different proxy types) are the data-level parameters characterizing the likelihood distributions or indicative meanings associated with the different proxies. These data-level parameters are optimized prior to implementing the statistical model, as described in Section 3.2.2.

3.2.2 Statistical model implementation

Distribution-fitting module

In the distribution-fitting module, we determine the indicative meaning of each coral taxa by analyzing the modern depth distributions (i.e., water depth of living coral) of corals prevalent throughout the western Atlantic/Caribbean region (“Caribbean-wide distributions”). We also examine the distributions of these same coral taxa using data only from south Florida (“Florida-specific distributions”), the location of the RSL proxy dataset. We follow Hibbert et al. (2016) for both analyses, basing the distributions on data from the ecological studies archived on the Ocean Biogeographical Information System database (OBIS, 2017, Appendix B.6.6). We analyze nine coral taxa (Figure B.3), based on their high prevalence in the Quaternary fossil record of the western Atlantic (Pandolfi and Jackson, 2006; Kuffner and Toth, 2017) and presence in the south Florida coral dataset. Data from the Flower Garden Banks National Marine Sanctuary are not included in the Caribbean-wide analysis because the relatively deep-water setting of these reefs is not representative of most Caribbean reef environments (Pattengill-Semmens et al., 2000). The majority of the data used in the Caribbean-wide analysis come from the Atlantic and Gulf Rapid Reef Assessment (AGRRA, 2017). AGRRA monitoring protocols suggest sampling should focus on reef zones within 1–15 m water depth, which could bias the distribution data; however, the fact that the depth optima of some coral taxa in the database are deeper than 15 m water depth suggests that this bias is small.

We fit the modern coral depth data to nonparametric, empirical probability distributions, using the kernel smoother with the ‘fitdist’ function in MATLAB, to assign the likelihood distribution of each coral taxon for use in the statistical model. We used a nonparametric approach in order to avoid making assumptions about the distribution of the data. The kernel smoother assumes that each data point has normal uncertainties and fits an individual probability density curve to each data point. The final probability density function is the sum of all of the smoothed curves (for details, see ‘ksdensity’ in MATLAB).

Sampling module

In the sampling module, we transform the observed proxy elevations $\hat{\mathbf{y}}$ into noisy RSLs \mathbf{z} and estimate the parameters Θ_s that characterize the sea-level processes. The likelihoods used in the sampling module are as defined in the data level (Section 3.2.1), such that:

$$p(\hat{\mathbf{y}}|\mathbf{z}, \Theta_d) = \prod_{i=1}^n p(\hat{y}_{ij}|z_i, \mu_j, \sigma_j), \quad (3.15)$$

where n is the number of RSL proxy records in the model, and Θ_d is the vector of data-level parameters μ_j, σ_j or the empirical pdf for each proxy type j .

We produce samples of noisy RSLs \mathbf{z} successively by conditioning on all other noisy RSLs and incorporating temporal uncertainty using a NIGP (see Appendix section B.2.1), such that:

$$p(\mathbf{z}|\mathbf{f}, \mathbf{t}, \Theta_d) \times p(\mathbf{f}, \mathbf{t}|\Theta_s) \times p(\hat{\mathbf{t}}|\mathbf{t}, \Theta_d) \times p(\Theta_s) \propto \prod_{i=1}^n p(z_i|\mathbf{z}_{-i}, \hat{\mathbf{t}}, \Theta_s) \times p(\hat{t}_i|\mathbf{t}_i, \Theta_d) \times p(\mathbf{f}, \mathbf{t}|\Theta_s) \times p(\Theta_s) \quad (3.16)$$

where the subscript $-i$ signifies all records except i , $p(\mathbf{f}, \mathbf{t}|\Theta_s)$ is the GP prior created with a sample from $p(\Theta_s)$, $p(\hat{t}_i|\mathbf{t}_i, \Theta_d)$ introduces the age uncertainty, and $p(z_i|\mathbf{z}_{-i}, \hat{\mathbf{t}}, \Theta_s)$ creates one RSL sample at time \hat{t}_i , conditioned on all other data.

Equations 3.15 and 3.16 are implemented in succession. Using an adaptive Metropolis-within-Gibbs sampling algorithm (Gelman et al., 2011) produces posterior estimates of $p(\mathbf{z}, \Theta_s|\hat{\mathbf{y}}, \hat{\mathbf{t}}, \Theta_d)$. For details on the algorithm, see Appendix section B.2.2.

Sample-wise prediction module

In the sample-wise prediction module, we combine the samples of noisy RSL (\mathbf{z}) with the samples of the RSL hyperparameters. Each sample Θ_s represents a prior distribution on RSL and is conditioned on a sample \mathbf{z} through the NIGP (see Section B.2.1 for details). The resulting sample-wise predictive distributions are then sampled and combined to estimate the overall posterior distribution of true RSL through time.

In order to test whether our model can successfully estimate RSL under various data and RSL scenarios, we designed a simulation experiment. We created two synthetic RSL time series representing RSL changes characteristic of deglacial and interglacial periods. We applied the model to data of different quantity, type, precision, and temporal distribution to evaluate performance. Results indicate that the best models are those that have high quality (low uncertainty) and/or quantity of data with trade-offs between the two (Appendix

section B.4.1).

3.2.3 Case study using Holocene data from south Florida

RSL archives from south Florida are chosen as a case study to evaluate the performance of the new statistical model framework because of the large quantity of data available from multiple proxy types, the length of the record (spanning ~ 11 ka to present), and the record's representativeness of the best constrained period of deglaciation. The south Florida dataset consists of 159 coral records and 62 sedimentary records. The 159 coral samples include *Orbicella* spp. ($n = 54$), *A. palmata* ($n = 53$), *P. strigosa* ($n = 18$), *Montastraea cavernosa* ($n = 10$), *Diploria labyrinthiformis* ($n = 9$), *Colpophyllia natans* ($n = 6$), *Pseudodiploria clivosa* ($n = 5$), *Siderastrea siderea* ($n = 3$), and *Porites astreoides* ($n = 1$). In addition, we add two extra data points to inform the model of prior knowledge on RSL at present and 13,000 years ago. One point is placed at -67 ± 10 m at 13 ka, and the other at 0 ± 0.2 m at 0 ka, based on data from a nearby site (i.e., Barbados; e.g., Abdul et al., 2016). Coral and sedimentary archives of sea level are compiled following standardized protocol described in Hijma et al. (2015) and Khan et al. (2017), where each sample's location, age, and elevation related to sea level is estimated or known and uncertainties associated with measurement and interpretation of the sample are quantified. A detailed description of the types of data, sampling methodologies, and assignment of uncertainties are in Section B.6.6.

To analyze how the various taxon-specific coral depth distributions affect RSL predictions within our framework, we apply the model to the database of Holocene coral and sedimentary archives from south Florida. We vary the types and interpretations of data in six distinct models (Table 3.2) to simulate how the model would perform with limited proxy types and/or quantities of data. Although the non-parametric kernel distributions fit the data better than parametric distributions, since they are an empirical distribution, we also implement a series of models using the best fit parametric distributions according to AIC criteria (see Table B.1 in Appendix B for AIC comparison). We compare the effects on the model estimates using log-normal, normal, and limiting fitted distributions against the results of models using non-parametric empirical distributions as likelihoods. We estimate RSL, rates of change, and uncertainties averaged over 1000-year periods, from 11 ka to present, and evaluate differences among the models.

The first two models (Parametric Caribbean Corals Only, PCCO; and Nonparametric Caribbean Corals Only, NCCO) use only coral (no sedimentary) proxies to model RSL. PCCO and NCCO both use the Caribbean-wide modern dataset to determine the relationship between all coral taxa and RSL. However, PCCO applies parametric fitted distributions of the Caribbean-wide modern coral dataset (Figure B.3) in Appendix B as likelihoods, whereas NCCO applies nonparametric distributions. The next two models (Nonparametric Florida Coral & Sedimentary, NFCS; and Nonparametric Caribbean Coral & Sedimentary,

Table 3.2: South Florida case study models

Interpretations of Proxies in each Model				
Model	Coral Dist.	<i>A. palmata</i>	Massive corals	Sedimentary data
PCCO	Caribbean parametric	Index points	Index points	<i>not included</i>
NCCO	Caribbean nonparametric	Index points	Index points	<i>not included</i>
NFCS	Florida nonparametric	Index points	Index points	Index/Limiting
NCCS	Caribbean nonparametric	Index points	Index points	Index/Limiting
Khan	Uniform 0-5 m	Index points	<i>not included</i>	Index/ <i>Limiting not included</i>
SDCL	<i>not included</i>	Marine limiting	Marine limiting	Index/Limiting

The Coral Dist. column indicates which, if any, modern depth distribution is applied to the data in the given model, whereas the *A. palmata* and Massive corals columns indicate whether those corals were treated as index points, using the specified coral distribution, as marine limiting data, or not included in the given model. The Sedimentary data column indicates whether that data were included in the given model.

NCCS) use the complete database of fossil proxies, where the relationship between all coral taxa and RSL is based on either the nonparametric fitted Florida-specific or Caribbean-wide coral depth distributions, respectively. We compare the two full models to evaluate the impact of using location-specific versus regional coral depth distributions. We use these models as the ‘best’ representations of true RSL change in south Florida because they are informed by the most sea-level data. The ‘Khan’ model is based on the interpretations of data in Khan et al. (2017), where limiting data are not incorporated into the model quantitatively, and only one coral taxa, *A. palmata*, is used, with a normal distribution approximating an assumed uniform distribution. The last model (Sedimentary Data Coral Limiting, SDCL) interprets all coral taxa as marine limiting.

3.3 Results

3.3.1 Distributions of living Caribbean corals

The modern depth distributions of the Caribbean corals that we analyzed are generally similar in form whether analyzing the Caribbean-wide dataset or the Florida-specific dataset. However, the broader Caribbean region tends to have more variability in the depths of living coral, which results in less precise (wider) nonparametric distributions (Figure 3.1). In order to compare the posterior RSL estimates of models using nonparametric likelihoods to a more conservative approach that assumes more generalized parametric distributions of the coral depths, we also fit the data to log-normal or normal density functions based on which distribution provided the best fit to the data (Appendix section B.1.1). The parametric distributions of the Caribbean-wide dataset are also wider than the Florida-specific (Figure B.3b).

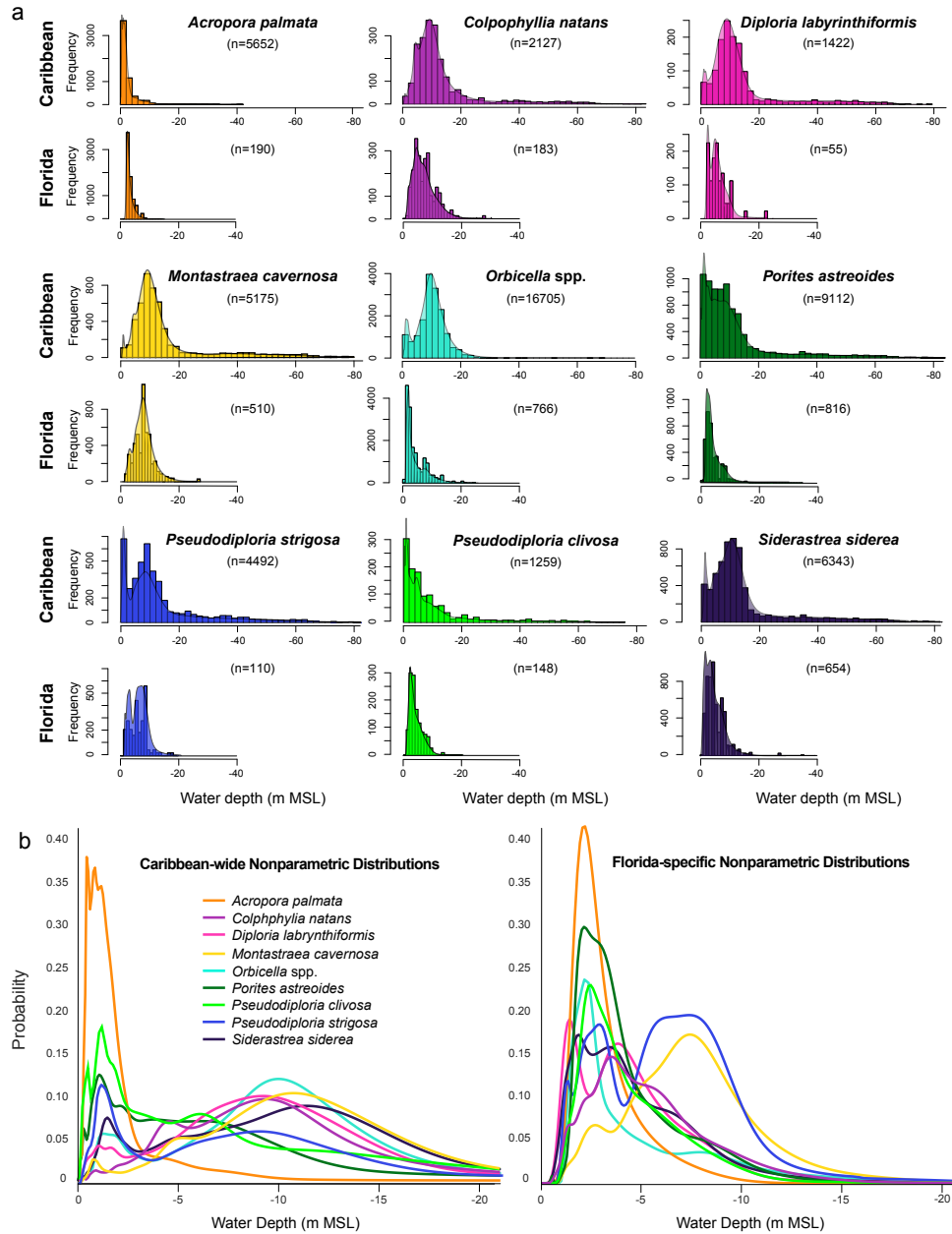


Figure 3.1: (a) Fitted distributions (shaded curves) and histograms of the 9 coral taxa, based on the Caribbean-wide modern depth data and Florida-specific modern depth data. (b) All fitted distributions for the Caribbean and for Florida up to 20 meters depth.

3.3.2 Comparison of different proxy data and their interpretation in the model framework

The data included in the Holocene case study from south Florida provide an opportunity to test the performance of the model under different data scenarios (Figure 3.2). This type of analysis can reveal information

about the existence of a ‘debated’ sea-level highstand in the Gulf of Mexico region (e.g., Donnelly and Giosan, 2008; Blum et al., 2008; Hawkes et al., 2016), provide constraints for GIA model parameters (e.g., Milne et al., 2005; Miller et al., 2013; Khan et al., 2017), or serve as a baseline with which to offer context for predicted RSL changes in the future (e.g., Lidz and Shinn, 1991; Törnqvist et al., 2002). Four of the six models produce similar patterns and estimated uncertainties (95% credible intervals [CIs]) of predicted RSL and rates of RSL change (estimated every 1000 years from 11 ka to present; Figures 3.2 and B.9). The most distinct differences in RSL estimates occur in PCCO, which predicts an anomalous highstand due to the wide parametric distribution (normal) of *Orbicella*, and in SDCL, where all of the corals are treated as marine limiting, which predicts higher RSLs in the early Holocene.

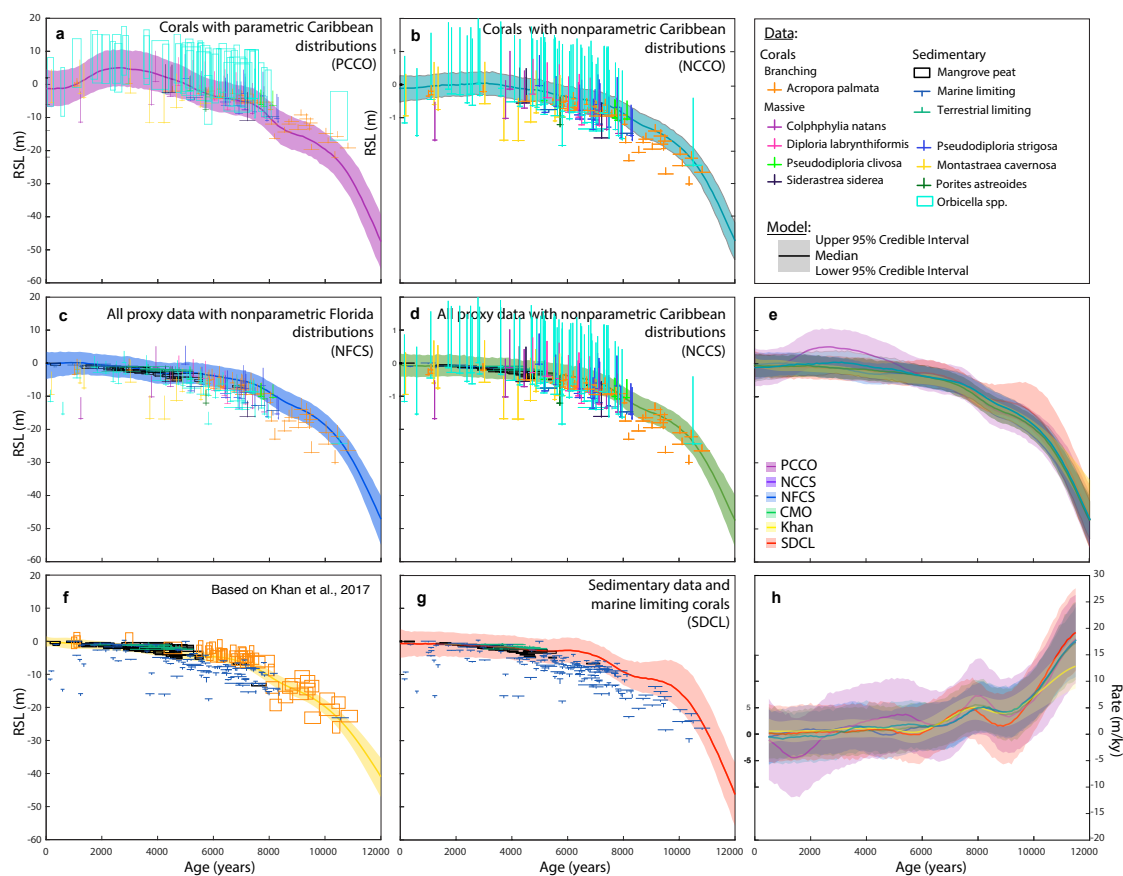


Figure 3.2: Models (a) PCCO, (b) NCCO, (c) NFCS, (d) NCCS, (f) Khan and (g) SDCL of Holocene RSL in south Florida. The individual model predictions and the interpretations of their data are plotted in the left and middle panels (a, b, c, d, f, and g) and the RSLs and rates of change from all six models are compared in the right panels (e and h) (see Figure B.9 for rates broken out into separate panels). Solid lines represent the median RSL or rate and shading represents the 95% credible interval.

3.4 Discussion

Because of the putatively large depth ranges of massive corals, these proxies have not generally been quantitatively incorporated into millennial-scale models of RSL (e.g., Khan et al., 2017). Instead, they have been interpreted by most researchers as marine limiting (e.g., Kopp et al., 2009), as in the SDCL model. Treating all corals as marine limiting results in higher estimates of RSL and larger uncertainties when there are no index points to anchor the RSL estimate, as in the early Holocene in model SDCL (Figure 3.2g).

Although massive coral RSL proxy records may be imprecise relative to mangrove peats, the taxa we evaluate can provide valuable constraints on RSL, when they supplement more precise proxy records; however, accurately constraining the relationship of these indicators to sea level is critical.

The multi-proxy models (NFCS, NCCS, and Khan) produce predictions that are in close agreement (Figure 3.2c,d,f). However, the reimplementation of the Khan model has smaller RSL prediction uncertainties (95% CI widths of 2.0–6.0 m, compared with 4.8–8.0 m for NFCS) and estimates the position of RSL to be ~ 0.5 m lower throughout the Holocene because the reimplementation of the Khan model is driven by the more precise sedimentary data and the inaccurate uniform distribution of the *A. palmata*, which record a lower RSL position. The offset observed between the models may be explained by biases associated with each type of proxy (see discussion below). The simplifying assumption of normality for all data in the reimplementation of the Khan model allows for increased computational efficiency; however, the empirical Bayesian model does not incorporate any uncertainty in model parameters, in contrast to the new framework. Although the distribution of *A. palmata* in the reimplementation of the Khan model is represented inaccurately and underestimates the tail of the distribution, the assumed uniform distribution approximated through a normal distribution does not vary considerably from the Caribbean-wide or Florida-specific nonparametric distributions. The general agreement between all three multi-proxy models justifies conclusions made in Khan et al. (2017) about RSL histories in the wider Caribbean region. Incorporating more proxy data with empirical likelihood distributions aids in estimating both RSL and its uncertainty more realistically. The additional information also provides a way to reduce the influence of potential biases associated with each proxy on its own.

Data with less precise distributions, such as massive coral taxa, can and should be used to augment more precise proxies of RSL; however, we do not recommend their use alone to generate RSL reconstructions, as the large uncertainties in these data increase the possibility of generating inaccurate predictions of RSL.

Using multi-proxy models with accurate estimates of empirical proxy distributions leads to predictions of RSL with the most accurate uncertainties, and potentially the least bias. Explicitly incorporating empirical coral depth distributions into RSL models provides quantitative data when or where more precise peat archives are not available and controls for possible biases of single-proxy models. Although full models may

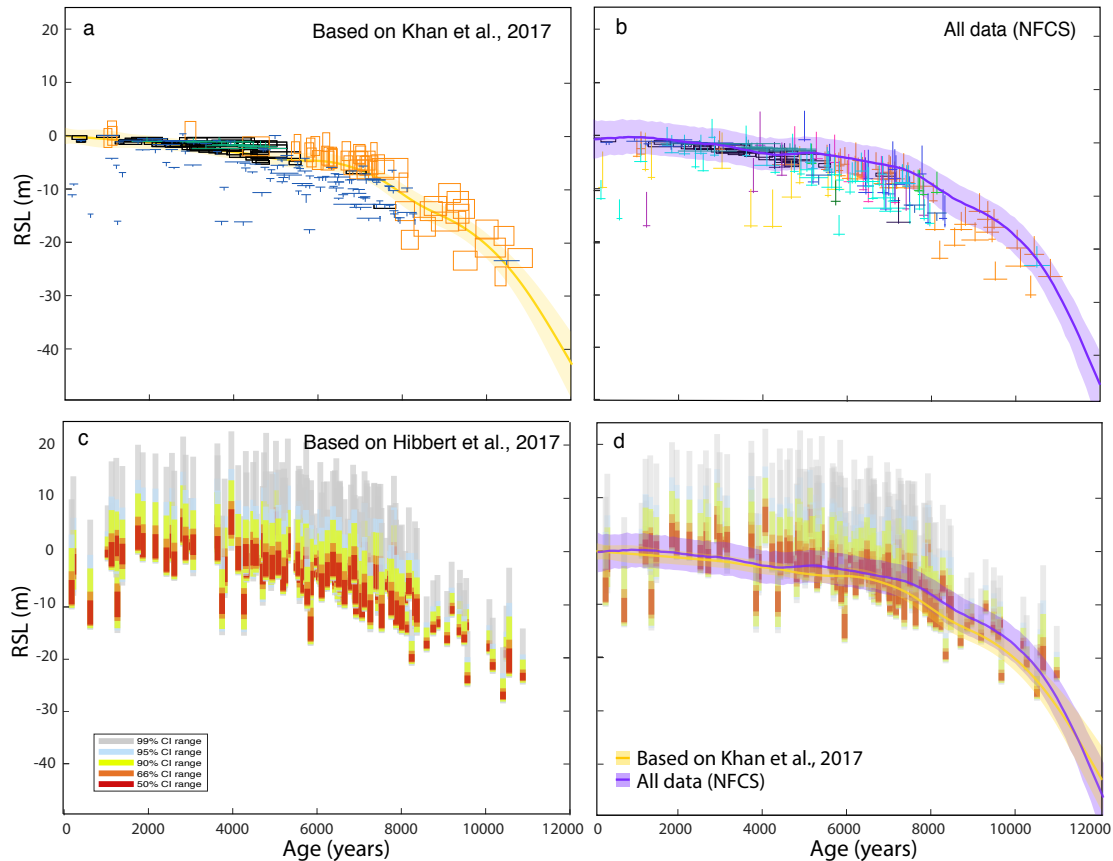


Figure 3.3: Comparison between two frameworks that incorporate corals as proxies for RSL and the current framework, using all available data. Khan et al. (2017) produced models that used spatial correlations to incorporate additional information, whereas Hibbert et al. (2016) used MCMC techniques to infer the probability of RSL at specific times based on modern empirical distributions, without considering correlations in time. Predictions of RSL (a-d) using our statistical framework with the Caribbean-wide coral distributions (CCS), Florida-specific coral distributions (FCS), and based on the statistical model developed by Khan et al. (2017) (Khan) and one similar to the coral framework of Hibbert et al. (2016).

have greater uncertainties in some cases (Figure 3.3), these uncertainties are likely to be more realistic as they incorporate more information. Our ‘database approach,’ which uses all available proxies, allows for the inclusion of a large number of sea-level data with varying degrees of precision and careful estimation of potential measurement errors associated with those data. This approach allows some inaccurate data without generating erroneous estimates of RSL. For example, the ‘Hibbert approach’ (Figure 3.3) uses the empirical distributions of each coral taxa, without statistically modeling the auto-correlation of the RSL process over time. This approach would predict a highstand from a single data point at ~ 4 ka and a drop in RSL at ~ 500 years ago based on another single data point. In contrast, our hierarchical models with an autocorrelated process level are robust to these sorts of data anomalies. Our new statistical framework for

including the depth distributions of multiple coral taxa, not just *A. palmata*, into models of RSL provides an important step forward in reconstructing RSL variability from low-latitude environments and a way to include previously underutilized additional proxies in other areas.

The depth distributions of both coral reefs and individual coral taxa exhibit some spatial variability as a result of environmental factors. The variability in the incident light reaching the water surface and other factors affecting the penetration of light to depth (e.g., water clarity or turbidity) are fundamental controls on the growth and abundance of corals across depths (Huston, 1985; Kleypas et al., 1999; Dullo, 2005). There are also local differences in light availability (Kleypas et al., 1999; Hubbard, 2009; Hibbert et al., 2016). For example, even putatively ‘shallow-water’ taxa like *A. palmata* have much broader depth distributions in Puerto Rico and the Virgin Islands (PRVI) than elsewhere in the Caribbean (Figure B.2; Hubbard, 2009). This is likely a result of both relatively clear waters and the presence of mesophotic (deeper water) coral reefs in this area (Smith et al., 2010). The depth uncertainties of all coral taxa, however, are largely dependent on the subset of data being used to model their relationship with depth. Therefore, care should be taken with the selection of data and the type of distribution used.

When applying nonparametric distributions in our model framework, the geographic differences in the likelihood distributions did not have a significant effect on predicted RSL models; however, the using the Florida-specific dataset seemed to result in more realistic estimates of RSL than using the Caribbean-wide dataset with parametric distributions. Although the full models using the Caribbean-wide and Florida-specific parametric depth distributions produce remarkably similar estimates of Holocene RSL, the coral-only model that uses the parametric Caribbean-wide distributions (PCCO) results in an anomalous highstand (Figure 3.2a) caused by the larger uncertainty in the normal distribution of the *Orbicella* spp. (Figure B.3). For reconstructions of Holocene RSL, using location-specific coral depth distributions based on robust empirical data may ideal for developing the most accurate coral-based models of RSL variability (Hibbert et al., 2016); on the other hand, some location specific-factors may have changed over time, which would argue for the use of distributions from a broader geographic area.

The use of empirical data distributions to characterize additional proxies for RSL, such as taxon-specific coral depth distributions, has the potential to improve both the accuracy and precision with which proxy data are included in models of Quaternary RSL variability. Nonetheless, the uncertainties of coral-based proxies may still be too large to reconstruct subtle RSL changes, such as melt-water pulses. Although it is beyond the scope of the present study, the empirical depth ranges applied to individual coral data could be further constrained by evaluating characteristics of the depositional environment and the taphonomy of the coral samples (Lighty et al., 1982; Neumann and Macintyre, 1985; Blanchon and Perry, 2004; Gischler and Hudson, 2004; Blanchon, 2005; Gischler, 2006; Perry and Hepburn, 2008; Hubbard, 2013) (See section B.6.7

in Appendix B for further discussion).

3.5 Conclusions

We develop a new technique for integrating non-Gaussian likelihoods into a hierarchical statistical framework to allow for a more realistic treatment of proxy uncertainties in probabilistic models of past RSL change. This approach is flexible, with the ability to include parametric and nonparametric likelihood distributions, and is compatible with approaches used in spatio-temporal hierarchical models of RSL. Our framework provides a method for incorporating empirical and parametric fitted depth distributions of a variety of proxies into RSL models, illustrated with coral taxa, and provides a way to incorporate new types of RSL proxies. Statistically reconstructing RSL within this hierarchical framework is necessary to achieve robust estimates of RSL. Our results suggest that using nonparametric distributions as likelihoods of proxy data in multi-proxy models provide the best estimates within the new framework.

The new framework developed in this study has broad applicability to the study of past RSL. Although we focus on a Holocene case study here, in order to assess the model in a time period that had overlapping constraints, a key application would be to areas where corals provide the only constraints (e.g., Barbados). This type of model can be used to assess rates of change during meltwater pulses by applying the model to deglacial datasets or to create more precise models to better understand interglacial periods. In addition, the incorporation of non-Gaussian likelihoods creates an opportunity to quantitatively integrate previously underutilized RSL proxy types, aside from corals, with the flexibility of distributions it can incorporate. Future work could expand the framework to include a spatial component, allowing nearby sites to share information with one another to improve the accuracy and precision of predictions of past sea level over a larger spatial scale.

Chapter 4

Half-meter sea-level fluctuations on centennial timescales from mid-Holocene corals of Southeast Asia

This chapter is adapted from Meltzner et al. (2017). The development, application, and description of the hierarchical sea-level models, as well as the results of the application of these models, were led by the author of this thesis, with guidance from Robert Kopp. The overall project was designed and led by Aron Meltzer, who led the writing of the overall manuscript. ¹

Abstract

Sea-level rise is a global problem, yet to forecast future changes, we must understand how and why relative sea level (RSL) varied in the past, on local to global scales. In East and Southeast Asia, details of Holocene RSL are poorly understood. Here we present two independent high-resolution RSL proxy records from Belitung Island on the Sunda Shelf and predict RSL and its uncertainty through an empirical hierarchical statistical model. The results of the model capture spatial variations, suggesting glacial isostatic adjustment and paleotidal range differences, and a common RSL signal between 6850 and 6500 cal years BP that includes two 0.6 m fluctuations, with rates of RSL change reaching 13 ± 4 mm per year (2σ). Proxy records along the south coast of China, although of a lower resolution, reveal fluctuations similar in amplitude and timing to those on the Sunda Shelf, which we model with an alternate version of the Belitung statistical model. The consistency of the Southeast Asian records, from sites 2,600 km apart, suggests that the records reflect regional changes in RSL that are unprecedented in modern times.

4.1 Introduction

More than 100 million people, mostly in East and Southeast Asia, live within 1m of sea level and are acutely susceptible to sea-level rise brought about by climate change (Li et al., 2009). Regional sea-level change

¹By Aron J. Meltzner^a, Adam D. Switzer^a, Benjamin P. Horton^b, **Erica L. Ashe**^b, Qiang Qiu^a, David Hill^c Sarah L. Bradley^{d,e}, Robert E. Kopp^b, Emma Hill^a, Jędrzej Majewski^a, Danny Natawidjaja^f, Bambang Suwargadi^f

^aNanyang Technological University, ^bRutgers University, ^cOregon State University, ^dUtrecht University, ^eDelft University of Technology, ^fIndonesian Institute of Sciences (LIPI)

is a superposition of secular eustatic trends and interannual regional oscillations, not all of which are well studied. The largest interannual variability of sea level occurs in the tropical Pacific and is related to the El Niño-Southern Oscillation (ENSO); early (1993-2001) satellite data showed high rates of sea-level rise in Southeast Asia that approached 30 mm per year (Church and White, 2006), though those extreme rates have not persisted (Zhang and Church, 2012; White et al., 2014).

Understanding the extent to which sea-level changes in East and Southeast Asia are affected by interannual sea-level variations is important to protecting vulnerable coastal assets in low-lying deltas (Syvitski et al., 2009) and atoll islands (McLean and Kench, 2015). But how interannual sea-level fluctuations will change in association with a projected increase in extreme ENSO and other patterns of atmosphere/ocean variability due to climate change remains unknown (Widlansky et al., 2015). Proxy-based paleo-sea level reconstructions characterize patterns of natural variability and provide a target for calibrating models of the relationship between climate and sea level, as well as a pre-Industrial background against which to compare recent trends (Kemp et al., 2011). These proxy reconstructions, however, have hitherto been hindered by accuracy and precision, particularly in East and Southeast Asia (Horton et al., 2005).

One relative sea level (RSL) proxy that has seen limited use in East and Southeast Asia is coral microatolls. Microatolls track RSL with accuracy and high precision. Prolonged subaerial exposure at times of extreme low water restricts the highest level to which the coral colonies can grow (e.g., Scoffin et al., 1978; Taylor et al., 1987; Zachariasen et al., 2000; Briggs et al., 2006). Portions of the coral living above this elevation die during a period of extreme low water, but portions below this continue to grow outward (and upward) until the next incidence of extreme low water. A microatoll's concentric annuli form as a result of this repeating sequence of slow upward growth and sudden diedowns, superimposed on longer-term RSL trends (Meltzner and Woodroffe, 2015).

With regard to microatolls, the term diedown refers to a partial mortality event on a coral colony in which the portion of a coral above a certain elevation dies, while coral polyps at lower elevations survive. Unlike a complete mortality of a coral colony, for which the interpretation of the cause of death is not always straightforward, a diedown to a uniform elevation around the perimeter of the coral is a clear indication that the diedown resulted from low water. The elevation above which all coral died is termed the highest level of survival (HLS) (Taylor et al., 1987). A related term, the highest level of growth (HLG) (Meltzner et al., 2010), reflects the highest elevation up to which a coral grew in a given year. Although both HLS and HLG refer to the highest living coral at a particular time of interest, HLG is limited by a coral's upward growth rate. Hence, in years during which no diedown occurs, HLG provides only a minimum estimate of the HLS that would theoretically be possible.

A microatoll's basic morphology reveals important information about RSL during the coral's lifetime.

Although a fall in RSL that triggers a diedown might be very short lived, such as during a single extreme low tide, multi-decadal trends in RSL can be established by comparing the elevations of several successive diedowns. Flat-topped microatolls record RSL stability; colonies with diedowns (HLS unconformities) that rise radially outward towards their perimeter reflect rising RSL during their decades of growth; corals with progressively lower diedowns reflect falling RSL. As RSL rises and falls over time, microatoll morphologies record these changes in RSL. Because these corals' skeletons have annual growth bands – a result of the contrasting density in growth at different times of the year – we can precisely count the years over which these changes occur.

We derive proxy records of mid-Holocene RSL from coral microatolls at two sites on Belitung Island, Indonesia, on the Sunda Shelf: TBAT, in the southeast; and TKUB, 80 km to the northwest (Figure 4.1). To extract climate-related rates of RSL change, we chose a region that is inferred to be tectonically stable (Simons et al., 2007), and sites where abundant granitic outcrops suggest minimal sediment compaction. Through an empirical hierarchical model, the Indonesian proxy records reveal 0.6-m swings in RSL over several centuries during the mid-Holocene. Accounting for systematic shifts in elevation between the time series at the two sites, and for peculiarities of microatoll growth over the 18.61-year nodal tidal cycle, the implementation of this hierarchical statistical model shows that a substantial majority of the multi-decadal scale fluctuations observed in each dataset can be explained by a shared sea-level curve. Consideration of reinterpreted data from an earlier study (Yu et al., 2009), which suggest coeval fluctuations of a similar amplitude 2,600 km away along the southern coast of China, argues that these changes were at least regional in scope.

4.2 Data

The proxy RSL records used in our analysis came from coral microatolls at two sites on Belitung Island, where we distinguish between four types of observations. At the TBAT site on southeastern Belitung, we found a population of microatolls, TBAT-F01, spread over a minimum distance of 200 m, with each microatoll at a similar elevation as one another. At the TKUB site on northwestern Belitung, no single coral recorded the complete RSL history from $\sim 6,750$ to $\sim 6,550$ cal years BP, but we compiled a RSL history for the period 6,800 to 6,440 cal years BP from five individual microatolls that all grew over a 3-km stretch, TKUB-F04, TKUB-F05, TKUB-F16, TKUB-F19 and TKUB-F23.

We distinguish between four types of observations from a coral slab: uneroded HLS elevations immediately following a diedown; uneroded HLG elevations immediately before a diedown; uneroded HLG elevations in years during which no diedown occurred, when the coral was in unrestricted upgrowth mode; and eroded HLG elevations (the highest level of preserved coral growth) for which it is unknown whether a diedown

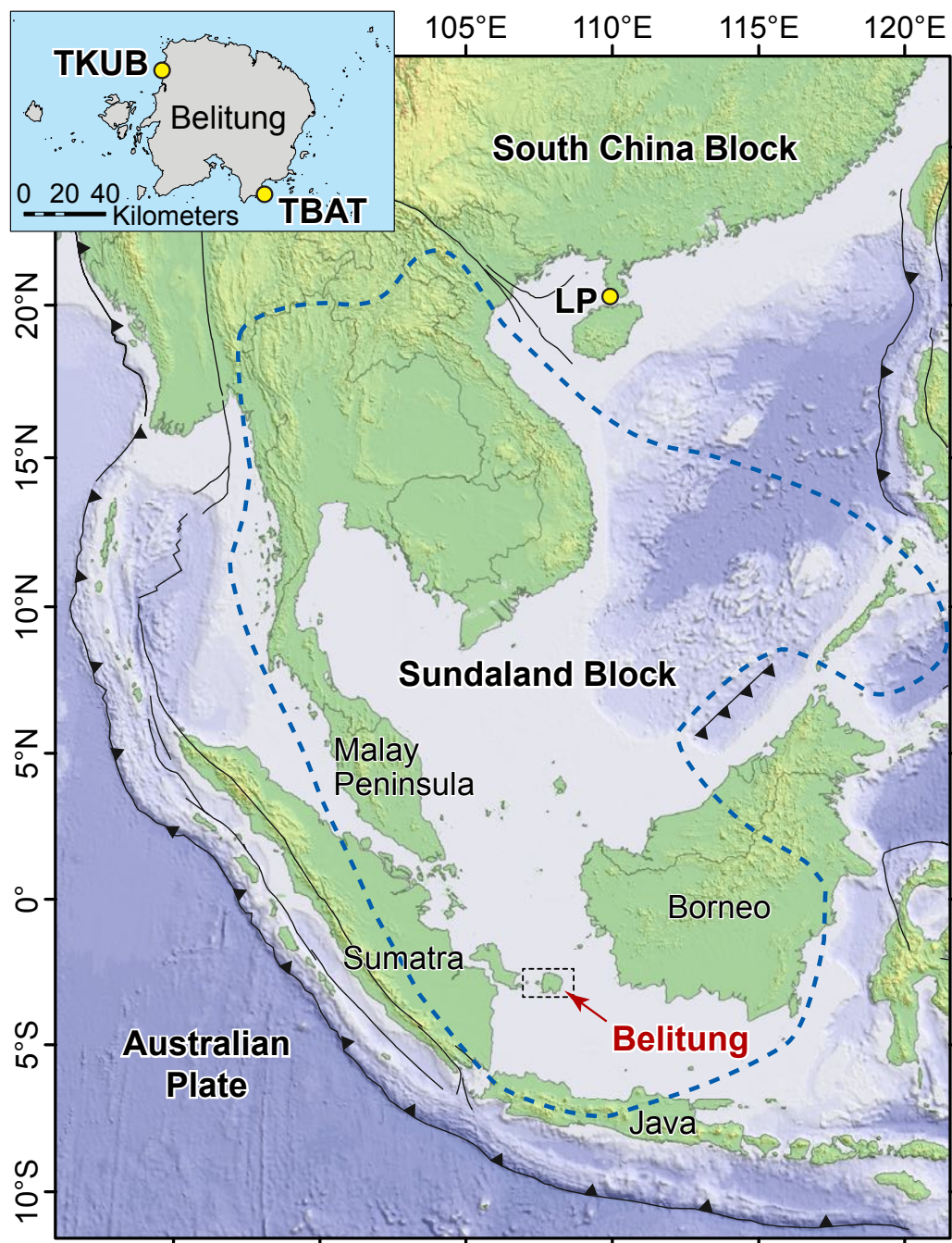


Figure 4.1: Map of the stable Sundaland block showing site locations. The extent of Sundaland, encompassed by the dashed blue curve, is approximated as the region deforming horizontally at ≥ 4 mm yr^{-1} relative to its core (Simons et al., 2007). Yellow circles mark coral microatoll study sites: LP, Leizhou Peninsula site (Yu et al., 2009); TKUB and TBAT (shown in inset), Tanjung Kubu and Tanjung Batuitam sites presented here. The inset location is denoted on the main map by a dashed box. Solid lines depict primary faults; barbed lines represent traces of subduction zones.

occurred. The first data type (HLS) is the most direct measurement of RSL, but it tracks only the most extreme low tides and may be biased by an unusual climate or weather event that results in a short duration lowering of sea level. The other data types (HLG) are all technically minimum bounds on low water level, because their elevations are controlled by the coral growth rate and not by RSL. The second data type (HLG just before a diedown) is considered to be a closer approximation to RSL than the third and fourth data types, but such data points are rarely preserved (Meltzner et al., 2010).

As proxies for sea level, we consider diedowns (HLS elevations) as sea-level index points. A sea-level index point estimates the unique position of RSL in space and time (Kelsey et al., 2015). HLG data are minimum limiting data, as they provide only a minimum bound on the theoretical HLS in a particular year. A perhaps counterintuitive consequence of microatoll growth over the 18.61-year tidal cycle is that the highest minimum limiting points in each cycle are expected to be up to 0.2 m higher than the lowest index points in the same cycle, even if RSL is stable over that interval. Any modeling methodology must account for this expected periodicity, and interannual trends and rates of RSL change may be meaningful only when averaged over periods longer than one 18.61-year cycle.

Because microatoll HLS is governed by extreme low water, diedowns tend to occur during portions of the 18.61-year cycle when the year-to-year lowest tides are becoming increasingly low, or when the tides are near their lowest levels. Subsequently, the year-to-year lowest tides rise more rapidly than corals can grow upward. For instance, if a microatoll at TKUB experienced a diedown during the lowest tide in 2006 and grew upward at 15 mm per year thereafter, it would have grown 0.15m vertically over the following 10 years, but its highest coral polyps (its HLG) would have been 0.20 m lower than the theoretical HLS in 2016 (Figure 4.2c). It would only be in 2020 that the upward coral growth would catch up to HLS, and with the lowest tides falling each year from 2020 until 2025, diedowns would be expected only in that interval. Similarly, diedowns at TKUB would have been expected in roughly the intervals 2001-2006, 1982-1987, 1964-1969 and so forth in the past. Transient meteorological conditions (such as rain, wind or cloud cover) and longer-term hydroclimatic oscillations (such as ENSO) also influence local sea level and coral diedowns, so minor deviations are expected in the actual timing and amplitude of the diedowns (for example, Figure 4.2d-g).

To determine the indicative meaning of coral HLS, we must determine the range of coral HLS elevations relative to tidal datums at each site. To calculate tidal datums, we used the Oregon State University regional tidal inversion for the Indian Ocean region (Egbert and Erofeeva, 2002). We extracted the harmonic constituents for each site and used them to calculate mean high water and mean low water (MLW) using formulas from the Manual of Harmonic Constant Reductions. We note that, because the Belitung region is characterized by diurnal tides, mean high water is equivalent to mean higher high water and MLW is equivalent to mean lower low water (MLLW) at each site. We also determined highest astronomical tide

and lowest astronomical tide (LAT) for each site by first computing predicted tide levels every hour over an 18.61-year tidal cycle, and then finding the maximum and minimum elevations. The tidal datums are shown in Figure 4.3; note the substantially larger tidal range to the northwest.

4.2.1 Chronological constraints and uncertainties

We distinguish between three kinds of chronological uncertainty in our study, and we treat the coral records as ‘floating chronologies,’ which we define as a groups of coral records with relative ages that are well-defined, with appropriate constraints from radiocarbon dating. First, the relative age uncertainty between two parts of an individual coral slab is simply the annual band-counting uncertainty, which is commonly less than ± 1 year. At the TBAT site, where the entire record comes from a single coral, relative age uncertainties are all in this category. In cases where two slabs have overlapping calibrated radiocarbon age estimates and matching diedown chronologies, those slabs can be coupled together as a single floating chronology, and the relative age uncertainty between various parts of those slabs is also determined from the band-counting uncertainty (Meltzner et al., 2010, 2012, 2015; Philibosian et al., 2014); this is the case for some of the TKUB corals, as discussed later.

Second, the relative age uncertainty between distinct corals at an individual site is governed by calibrated radiocarbon age errors. For radiocarbon dating of marine samples such as corals, a marine calibration curve is used (Reimer et al., 2009), and every site has a localized marine reservoir correction, ΔR , expressed as an offset (in years) from a global-mean value. Although site-specific ΔR values typically have uncertainties of decades to centuries, we extracted multiple samples from each slab for dating, and the exceptional consistency between the redundant dates on each coral (Meltzner et al., 2017) indicates that the ΔR value at each site did not vary temporally over the period of study. We can, therefore, ignore uncertainties in ΔR if we are interested only in the relative age of two corals at the same site. At the TKUB site, relative age uncertainties between the corals do not exceed 70-80 years (2σ). To estimate absolute ages, we assumed $\Delta R \approx +89$ years, based on a nearby sample from southwestern Borneo (Southon et al., 2002), but our primary conclusions do not depend upon knowing this correction accurately.

Third, absolute ages for each RSL proxy time series carry additional uncertainty resulting from the unmodeled error in ΔR . This uncertainty applies uniformly to each site’s RSL time series as a whole, based on the argument that ΔR at each site remained constant over the period of study, affecting the absolute timing of each curve, but not its shape. The uncertainty may be ± 85 years, based on the ΔR error of modern samples collected nearby (Southon et al., 2002) and mid-Holocene samples from the South China Sea (Yu et al., 2010). Each site’s RSL curve could therefore be shifted uniformly by up to ± 85 years.

A total of eight radiocarbon samples were dated from TBAT-F01 and at least two radiocarbon samples

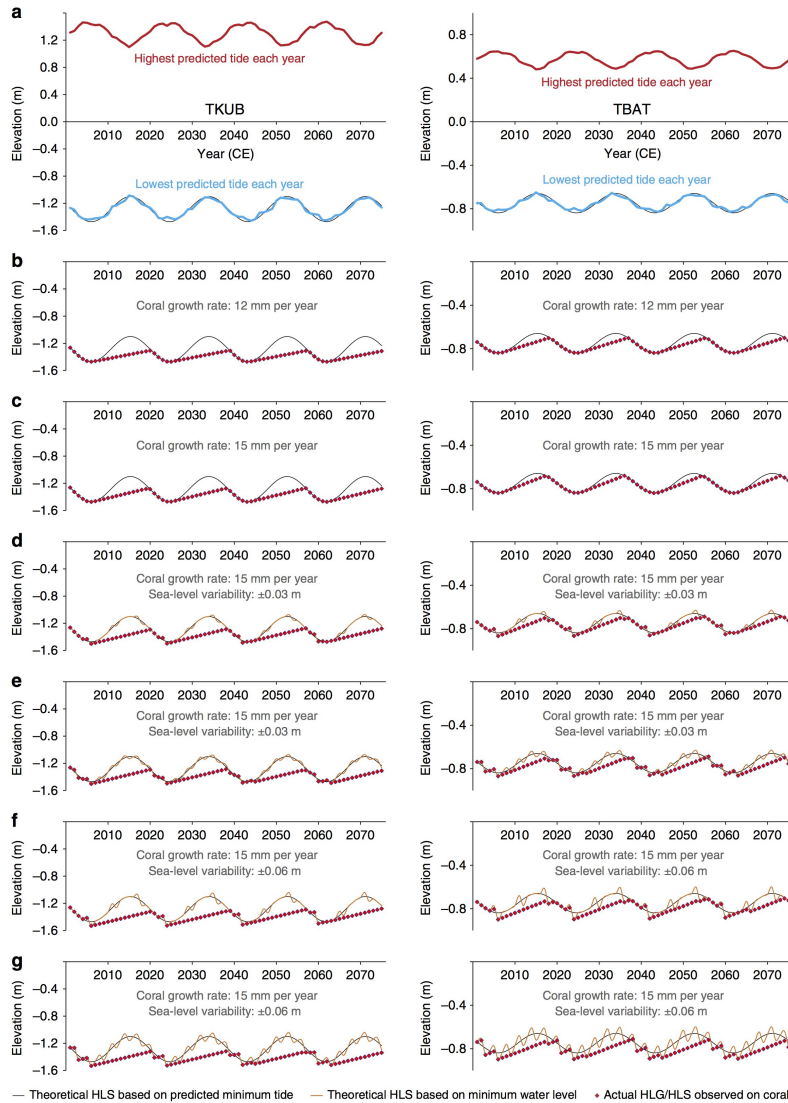


Figure 4.2: Schematic coral growth scenarios at the TKUB and TBAT sites. The observed propensity for and occasional clustering of coral diedowns toward the end of each 18.61-yr nodal tidal cycle is predicted by schematic models of coral growth over the 18.61-yr cycle. These models illustrate the year-to-year variability of the difference between the highest living coral polyps and the lowest water levels. (a) Highest and lowest tides in each calendar year predicted for each site by a tidal model. In black, we fit a sinusoid (fixed period: 18.61 yr) to the annual lowest tides; that sinusoid is reproduced in (b) through (g) as the “theoretical HLS based on predicted minimum tide.” (b, c) Expected highest level of growth (HLG) or highest level of survival (HLS) based on coral growth rates of 12 mm yr^{-1} (b) or 15 mm yr^{-1} (c) in light of the predicted annual minimum tides at each site. There is a nonzero vertical offset between coral HLS and minimum water level, but that offset is assumed to be constant over time and is ignored here for the sake of simplicity. (d, e) The scenario in (c), but with the added complexity of interannual, random sea-level variability of $\pm 0.03 \text{ m}$. (f, g) The scenario in (c), but with the added complexity of interannual, random sea-level variability of $\pm 0.06 \text{ m}$.

were dated from each TKUB coral. All dates were consistent with other coral samples from the same coral colony at 1σ . The radiocarbon dates were modeled using the OxCal calibration program (Ramsey, 2008). We applied the Marine13 radiocarbon age calibration curve (Reimer et al., 2009), assuming the marine reservoir correction $\Delta R \approx +89$ years, based on a value established from an early 20th century sample from southwestern Borneo (Southon et al., 2002). Although ΔR at TKUB may differ from ΔR at TBAT, the consistency among the unmodeled TKUB dates precludes significant variation in ΔR over the lifetime of each coral at the TKUB site. Additionally, although there is considerable uncertainty in any ΔR value and its extrapolation spatially and to samples from the mid-Holocene, we can establish that, whatever ΔR was at our sites at the time, it did not vary in a statistically significant way over the lifetimes of our mid-Holocene corals. This observation is crucial, because it allows us to ignore uncertainties in ΔR if we are concerned with only the relative age, or the difference in age, between two corals at the same site.

We use the following argument to demonstrate that ΔR at TBAT did not vary over time. Comparing the unmodeled calibrated radiocarbon dates, assuming for now that $\Delta R \approx +89$ years (with zero uncertainty about that assumed value) and accounting for the number of annual growth bands separating the various samples, seven of the eight ages agree at 1σ and all agree at 2σ (Meltzner et al., 2017). This is consistent with the hypothesis that the reported laboratory errors and the calibration curve correctly describe the uncertainty: 68% of data should agree at 1σ , and 95% should agree at 2σ . This agreement precludes significant variation in ΔR over the 250-year lifetime of TBAT-F01; if the marine reservoir correction varied by more than a few decades over that period, we would not expect such consistency among the unmodeled radiocarbon dates.

The proxy records from southeastern Belitung were reconstructed from a single coral microatoll slab (TBAT-F01), whereas the records from the northwestern Belitung were reconstructed from five shorter-lived coral slabs at different elevations (TKUB-F04, TKUB-F05, TKUB-F16, TKUB-F19 and TKUB-F23). Analyses of slab growth patterns and radiocarbon dates from each microatoll suggest that TKUB-F04 and TKUB-F05 were coeval and constitute a single floating chronology, while TKUB-F16 and TKUB-F19 also overlapped in time and form a second floating chronology; the TKUB-F23 record, by itself, is a third floating chronology at the TKUB site. See Meltzner et al., 2017 for more details on all coral microatoll slabs used in analysis.

4.2.2 Vertical uncertainties of microatoll data

We distinguish between two types of vertical uncertainty in our study. The first is aleatoric and quantifiable: random errors that affect the elevation of one part of a curve relative to another part of the same curve. This accounts for the natural distribution of HLS elevations in any population of corals, including the

possible effects of unrecognized ponding. Ponding is a phenomenon whereby some corals can survive at higher elevations than they could otherwise, in elevated enclosed pools that do not drain fully at low tide (Meltzner and Woodroffe, 2015; Hopley, 1982). Ponding is not always easy to recognize, as the effect can be gradual: one pool may raise the water level at extreme low tide by only a few centimetres over the level in an adjacent pool immediately seaward. Nonetheless, the cumulative effect of multiple subtle ponds at progressively higher elevations tends to exceed 0.1 m only on the wider and more physiographically complex reefs (Smithers and Woodroffe, 2000).

To estimate a formal uncertainty about the elevation of any one RSL proxy data point, we surveyed a distribution of HLG elevations on living corals (including some that were clearly ponded) at each site. We augmented this dataset with the elevation differences between coeval diedowns seen in slabs from two different living corals at the TKUB site (Meltzner et al., 2017). The standard deviation of differences in elevation of coeval HLG or HLS at each of our Belitung sites is 0.090 m. This is consistent with observations in Australia, but slightly larger than estimates from off the west coast of Sumatra (Meltzner and Woodroffe, 2015). The wider distribution of coral HLS on Belitung than off the west coast of Sumatra may occur because of the wider reefs on Belitung, and/or because the tidal range there is larger.

Because ponding is a concern in sea-level studies using coral microatolls, we specifically address whether our results might be biased by ponding in ways that we have not yet considered. At the TKUB site, because the RSL curve was constructed from five separate corals, it is possible that some of the higher and more landward corals (TKUB-F04, TKUB-F05 and/or TKUB-F23) were ponded by significant amounts, that is, by ≤ 0.1 m. However, the amplitude of the mid-Holocene oscillations is twice the range of HLS observed among living microatolls on the modern reef, even considering the highest ponded corals (Figure 4.3). At the TBAT site, ponding is less likely to explain the observed oscillations, as the oscillations are entirely recorded on individual microatolls. Finally, the two sites are located 80 km apart, on opposite sides of Belitung Island (Figure 4.1). This separation is sufficient that it would require a remarkable coincidence to explain the similar changes at the two sites if those changes were caused primarily by localized ponding at each site.

The second type of vertical uncertainty is epistemic and affects the elevation of the entire RSL curve as a whole. These systematic vertical errors are not shown on any figures in this chapter, but include uncertainty in the change in tidal range at each site; uncertainties in tectonic effects or compaction at each site; and uncertainty in the HLS elevation of living corals at each site, which is used as the reference elevation for past RSL (Meltzner and Woodroffe, 2015; Woodroffe et al., 2015). These errors are difficult to quantify, but they are likely small. Tide modeling (Meltzner et al., 2017) and tectonic modeling (Meltzner et al., 2017) suggest both of those effects are on the scale of centimeters, and neither compaction of the thin sediments underlying the fossil corals nor ponding of the living microatolls is likely to bias the RSL curve at a site by

more than ~ 0.1 m.

To estimate vertical uncertainties, we surveyed living coral microatolls at both the TBAT (southeastern) and TKUB (northwestern) sites (Meltzner et al., 2017). Ponding of water at low tide, particularly on a wide coral reef, is a known complication that allows individual corals to grow above the theoretical HLS (Meltzner and Woodroffe, 2015). We therefore considered a mix of ponded and open-ocean microatolls in our survey, classifying each colony as either clearly open-ocean, clearly ponded or possibly ponded. The result, shown in Figure 4.3, represents the distribution of HLS elevations immediately following a diedown. HLG elevations in subsequent years would be higher than the elevations shown, by an amount dependent upon the coral growth rate and the time since the most recent diedown. The standard deviation of modern HLS at each Belitung site, including ponded and open-ocean microatolls, is 0.09 m; we apply this as the error to the fossil (mid-Holocene) coral data as well.

4.3 Statistical methods

To analyze the RSL proxy data, we constructed an empirical hierarchical statistical model (Chapter 2), separated into three levels: a data level, which models the recording of RSL by proxies; a process level, which models RSL at the different sites; and a hyperparameter level, which characterizes key attributes of the first two levels.

At the data level, RSL index points (HLS elevations following diedowns) from Belitung are preserved typically once or twice per 18.61-year nodal tidal cycle, whereas minimum limiting data (HLG elevations, or minimum bounds on low water level) are resolved each year. We use all of the index points, as they are indicative of sea level. The selection of limiting data is more complicated, however, as our model treats limiting data as faithful sea-level indicators, yet in reality some limiting data are severe underestimates of sea level. Specifically, any limiting data from before a microatoll's initial diedown represent coral growth up to that initial HLS, and these data may be decimetres (or even metres) below HLS14. Even after a coral's initial diedown, some limiting data from our sites are expected to be as much as 0.20 m lower than the theoretical HLS (Figure 4.2); in these cases, the highest limiting data point within each 18.61-year cycle should be a reasonable approximation of theoretical HLS for that year, and therefore a useful proxy for RSL. In principle, erosion should also be considered at the data level, but because we selected slabs that were well preserved, erosion was negligible (~ 0.05 m or less) and can be ignored over most of the time series in our study. An exception to this is the later RSL peak at both sites, $\sim 6,600$ - $6,550$ years BP, where no diedowns are preserved and erosion may locally exceed 0.15 m. Because of this limitation, our model may underestimate the elevation of the second RSL peak, and the amplitude of the fluctuations we infer in our study should be considered a conservative minimum estimate.

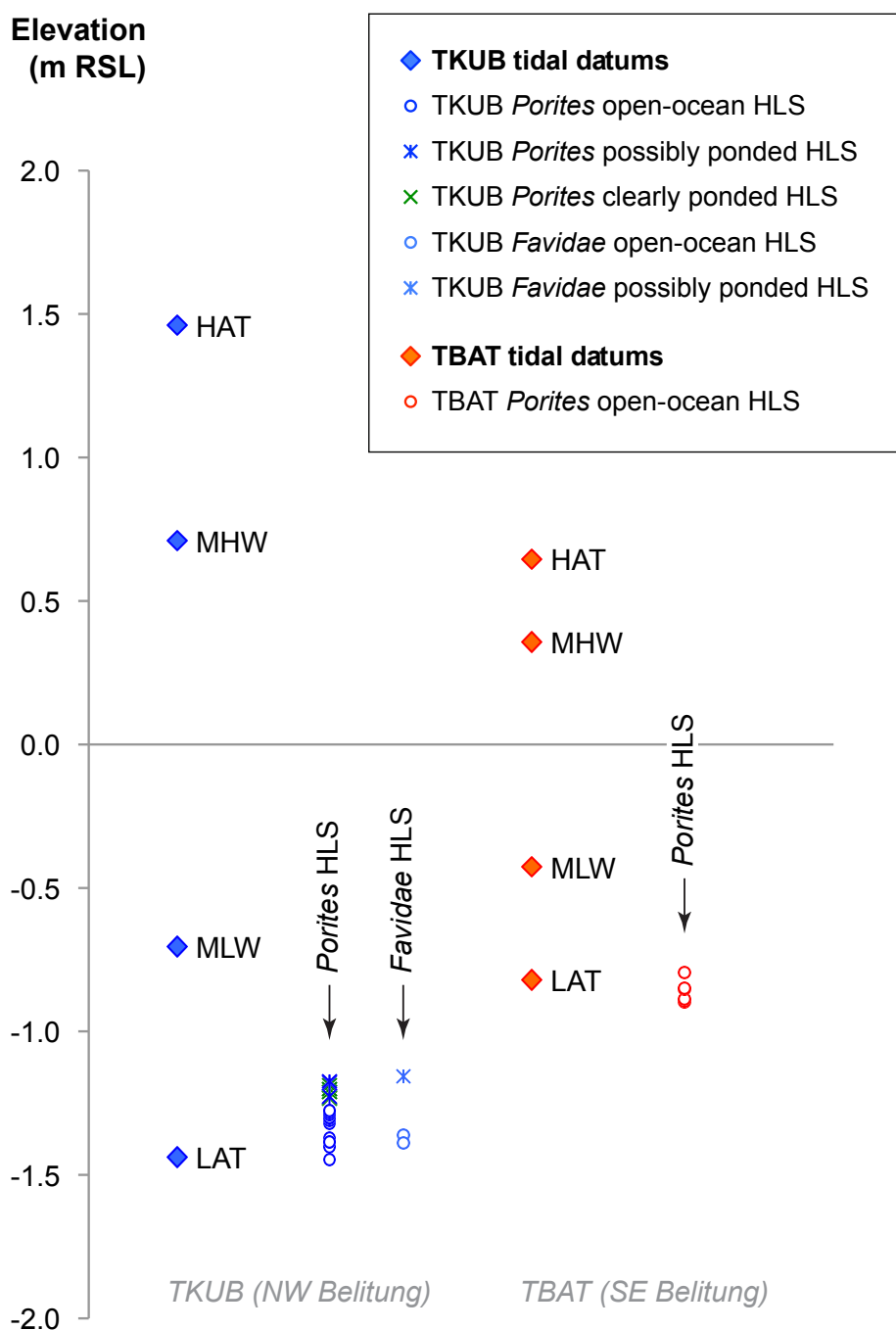


Figure 4.3: Living coral HLS at each site compared to tidal datums. Tidal datums are estimated from the Oregon State University regional tidal inversion for the Indian Ocean region (Parrenin et al., 2007). HAT, highest astronomical tide; MHW, mean high water; MLW, mean low water; LAT, lowest astronomical tide. See Meltzner et al. (2017) for details of the construction of this plot.

Our preferred strategy for modeling limiting data from the Belitung sites is therefore to subsample the limiting data by selecting only the highest limiting point in each 18.61-year bin (Figure 4.4); nonetheless, we also consider an alternative strategy, in which we use the highest limiting point available for each year (the only point available in most years), excluding only the early part of TKUB-F16, before the coral had grown up to HLS. The preferred strategy is an attempt to use only data that reliably approximate a given year’s theoretical HLS; the alternative strategy is an attempt to use as much of the limiting data as is possibly justifiable.

We model noisy proxy observations (y_i) of RSL elevation as:

$$y_i = f_j(t_i + \Delta_k) + \varepsilon_i, \quad (4.1)$$

where i indexes data points and j indexes sites, and the function $f_j(t)$ is true RSL at site j and time t . Each observation belongs to one of four floating chronologies (the entire record at TBAT, plus three discrete floating chronologies at TKUB), indexed by $k \in [0, 3]$; each floating chronology is associated with an age shift Δ_k . The sea-level observation errors, ε_i , are treated as uncorrelated and normally distributed, with σ of 0.09 m, determined as discussed in the data methods (Section 4.2.2).

Coral ages are constrained by radiocarbon dating methods. Because we can assume that the marine radiocarbon reservoir correction, ΔR , is fixed over time at each site, the relative age uncertainties between the three floating chronologies at the TKUB site are determined by the radiocarbon ages (Meltzner et al., 2017); these inter-slab age uncertainties result in the possibility that one, two or all three of the TKUB floating chronologies are as much as 21 years older. In addition, uncertainty in ΔR at each site allows for an inter-site relative age shift between the overall time series at the TKUB site and that at the TBAT site of up to approximately ± 120 years (the ± 85 -year uncertainty from each site added together in quadrature). Because the modeling depends only upon relative ages and not upon absolute ages, and because the inter-site relative age uncertainty is so much larger than the intra-site relative age uncertainties, we need only three age-shift parameters, $\Delta_0, \Delta_1, \Delta_2$, and we can define them in a way that is more intuitive than elicited by the formula above (we fix Δ_3 at 0 years). For convenience, we hold the time series at TBAT fixed to that determined assuming $\Delta R = +89$ years, as discussed in the text. Δ_0 is the overall age shift of the TKUB record relative to the TBAT record, and we allow $-120 \text{ years} \leq \Delta_0 \leq +120 \text{ years}$. Δ_1 and Δ_2 are the age shifts of the oldest and youngest floating chronologies at the TKUB site relative to the central floating chronology at the site, such that the sum of Δ_1 and Δ_2 is a maximum of 21 years (and a minimum of 0 year), where Δ_1 and Δ_2 are shifts in opposite directions, Δ_1 making the oldest slabs older and Δ_2 making the youngest slab younger. Age uncertainties within individual floating chronologies are not incorporated into the model, as the law of superposition prohibits swapping the order of data derived from successive

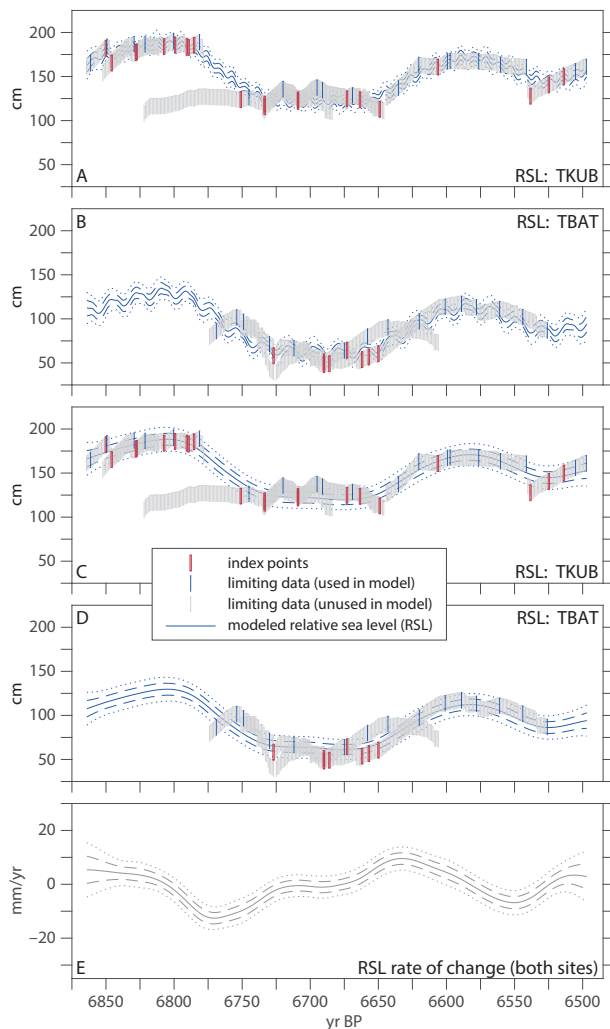


Figure 4.4: Posterior sea-level curves based on an empirical hierarchical model that includes a non-linear term, common to both sites, in addition to a site-specific constant vertical shift and a periodic term, tuned to simulated coral growth over the 18.61-yr nodal tidal cycle at each site. The timing of the TBAT site time series is fixed to that determined using $\Delta R = +89$, but the three floating chronologies for TKUB are individually allowed to float relative to the TBAT time series, as described in the text. Here all index points and the highest limiting data point within each 18.61-yr bin are conditioned upon in the model. (a, b) The full model, for sites TKUB and TBAT, including the 18.61-yr periodic term for each site. (c, d) The model with periodic terms excluded, to show only secular trends in RSL, for TKUB and TBAT. The modeled curves in (c) and (d) are identical, except for a uniform shift in RSL between the two sites. (e) Rates of change, averaged over 20-yr running windows, determined from the model in (c) and (d). For the index points and limiting data, symbols show $\pm 1\sigma$ vertical error bars (± 9 cm) and $\pm 2\sigma$ relative timing errors (± 0.5 yr band-counting uncertainties). For the models, dashed and dotted curves depict $\pm 1\sigma$ and $\pm 2\sigma$ error envelopes, respectively.

annual bands, effectively rendering the relative age uncertainty to be negligible.

At the process level, $f_j(t)$ is specified as the sum of a common (shared) regional sea-level signal $g(t)$, a

site-specific periodic signal representing the 18.61-year nodal tidal cycle $p_j(t)$, a site-specific offset c_j , and high-frequency variability $w_j(t)$:

$$f_j(t) = g(t) + p_j(t) + c_j + w_j(t) \quad (4.2)$$

The prior distribution of the shared signal, $g(t)$, is a mean-zero Gaussian process (GP) (Rasmussen and Williams, 2006) characterized by hyperparameters that comprise an amplitude σ_g and a timescale of variability τ ,

$$g(t) \sim \mathcal{GP} \{0, \sigma_g^2 \rho(t, t'; \tau)\}, \quad (4.3)$$

where ρ is the Matérn correlation function with smoothness parameter 3/2 and scale τ . The use of a smoothness parameter of 3/2 ensures that the first derivative of the process will be defined everywhere, but allows for abrupt changes in rate.

The prior distribution of the periodic signal representing coral growth over the nodal tidal cycle, $p_j(t)$, is a mean-zero GP characterized by hyperparameters that comprise an amplitude σ_p , a smoothness parameter ν_p and a fixed period corresponding to the nodal tidal period, 18.61 years (Haigh et al., 2011):

$$p_j(t) \sim \mathcal{GP} \left\{ 0, \sigma_p^2 \exp \left(\frac{-2 \sin^2 \left(\frac{\pi(t-t')}{18.61} \right)}{\nu_p^2} \right) \right\}, \quad (4.4)$$

where t and t_0 are defined in years. The hyperparameters of this periodic component are tuned for each site to simulations of coral growth under present-day nodal tidal cycles at the site. We assumed a coral growth rate r that is normally distributed with a mean of 12 mm per year and s.d. of 2 mm per year and a periodic cycle with tidal amplitudes (σ_p) of 0.186 and 0.089 m at TKUB and TBAT, respectively. For tuning these hyperparameters, simulated RSL is given by:

$$RSL(t) = \sigma_p^2 \left(1 + \cos \left(-\pi + \frac{2\pi t}{18.61} \right) \right) \quad (4.5)$$

The simulated coral height at any given time, $CH(t)$, is equal to the minimum of $RSL(t)$ and the potential growth of the coral according to the randomized growth rate, based on the coral height in the previous year, $CH(t-1) + r$:

$$CH(t) = \min[CH(t-1) + r, RSL(t)]. \quad (4.6)$$

We generate five random, 100-year-long time series at each site with random growth rates for each time series, and fit these synthetic coral height data to a mean-zero GP, equivalent to the periodic component of the process model plus white noise. We use these maximum-likelihood parameters from this exercise as the

amplitude and smoothness hyperparameters in $p_j(t)$ of the original process level, above.

The prior distribution of the constant site-specific offset, c_j , is normal with mean zero and variance σ_c^2 . We restrict this site offset to being constant because we do not expect any physical processes to give rise to significant centennial-scale or sub-centennial-scale variations in RSL between the two sites. The two sites should be exposed to essentially indistinguishable dynamic sea-level changes, and any tectonic deformation at these sites should be small and similar at the two sites (discussed later in Methods). While GIA and changes in tidal range do vary spatially, any changes due to these processes should be small enough on a centennial scale that they are well within any noise.

The prior distribution of the high-frequency variability in RSL, $w_j(t)$, is modeled as white noise, with a normal distribution with mean zero and variance σ_w^2 .

We employ an empirical Bayesian analysis method, in which the age-shift parameters $\Delta_0, \Delta_1, \Delta_2$ and the hyperparameters $\sigma_g, t, \sigma_c, \sigma_w$ are point estimates calibrated based on the data to maximize the likelihood of the model (optimized values are 0.7, 20.3, and 54.0 years for the age-shifts and 878 mm, 182.6 years, 590 mm, and .02 mm, respectively). The hyperparameters σ_p, ν_p are optimized as described above (optimized values are 66.3 mm and 0.98, respectively), based on the present-day tidal cycles and coral growth models at TKUB and TBAT, and are held constant during the optimization of the other hyperparameters. The key output of the empirical Bayesian model is an estimate of the posterior probability distribution of the RSL field, $f_j(t)$, conditional on the tuned hyperparameters (Figures 4.4 and 4.5).

4.3.1 Reinterpretation of published data from southern China

Yu et al. (2009) surveyed, sampled and dated a suite of coral microatolls from a site on the Leizhou Peninsula, along the southern coast of China. Unlike in our study, where we collected and analyzed full radial slabs of each microatoll, they presented primarily point data from the upper surfaces of microatoll annuli. In total, they published 13 dated samples, each of which was tied to the elevation from which it was collected. They also provided photos and cross-sectional sketches of each microatoll, so although those authors focused only on the upper surfaces, they provided enough information to estimate the timing and elevations of the more prominent diedowns.

We reinterpreted the RSL curve of Yu et al. (2009) (Figure 4.9) by estimating the timing and elevations of those more prominent diedowns. The reported ages were based on U-Th techniques (typically with small errors) and were all in the expected sequence (ages from the outer annuli of each microatoll were sequentially younger than ages from the inner annuli), so it was straightforward to estimate the timing of each diedown, and to correlate diedowns from one coral to another. Numerous points in each photograph were marked with surveyed elevations, providing a sense of scale, so we were able to estimate the elevations of those diedowns

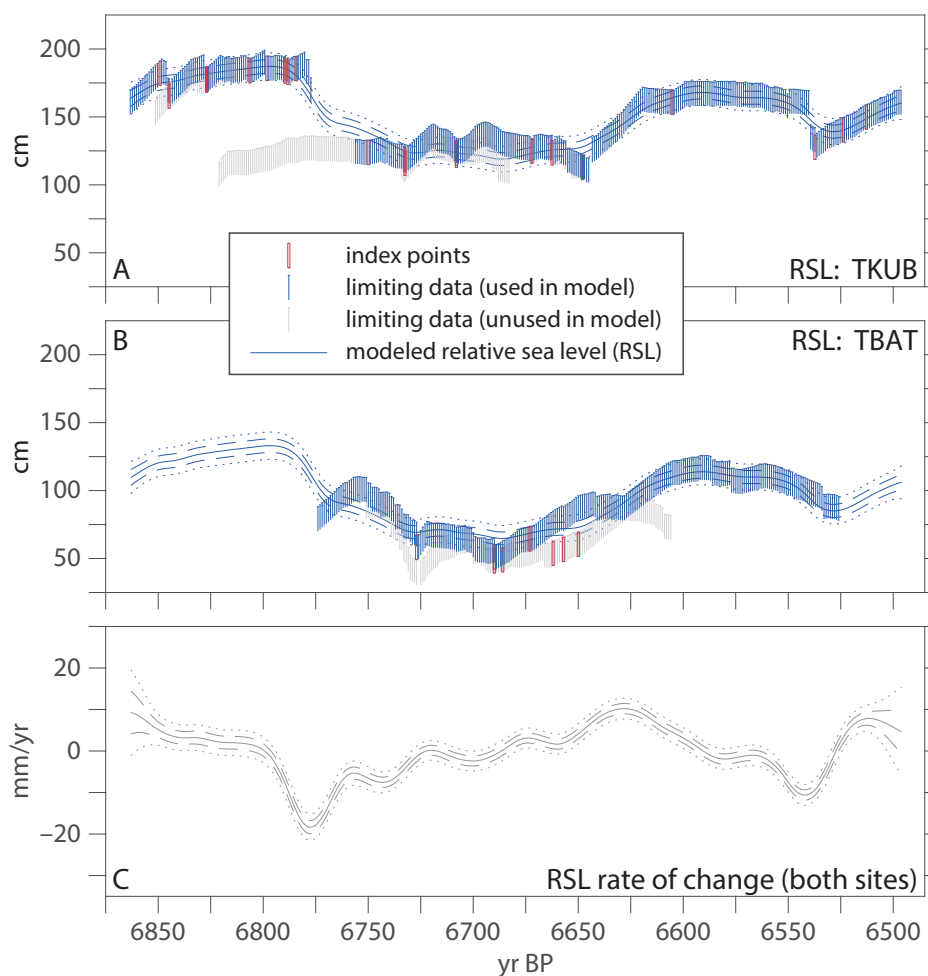


Figure 4.5: Posterior sea-level curves based on an empirical hierarchical model that includes a non-linear term, common to both sites, in addition to a site-specific constant vertical shift, excluding the periodic term. The timing of the TBAT site time series is fixed to that determined using $\Delta R = +89$, but the three floating chronologies for TKUB are individually allowed to float relative to the TBAT time series, as described in the text. Here all index points and the highest limiting data point available for each year (excluding the early part of TKUB-F16, before the coral had grown up to its highest level of survival, or HLS) are conditioned upon in the model. (a, b) The model with periodic terms excluded, to show only secular trends in RSL, for TKUB and TBAT. The modeled curves in (a) and (b) are identical, except for a uniform shift in RSL between the two sites. (c) Rates of change, averaged over 20-yr running windows, determined from the model in (a) and (b). For the index points and limiting data, symbols show $\pm 1\sigma$ vertical error bars (± 9 cm) and $\pm 2\sigma$ relative timing errors (± 0.5 yr band-counting uncertainties). For the models, dashed and dotted curves depict $\pm 1\sigma$ and $\pm 2\sigma$ error envelopes, respectively.

with sufficiently conservative vertical errors.

Last, we correlated coeval annuli from one coral to another based on their reported ages. Again, this was straightforward, as the microatolls provide a consistent, reproducible RSL history, with the same number

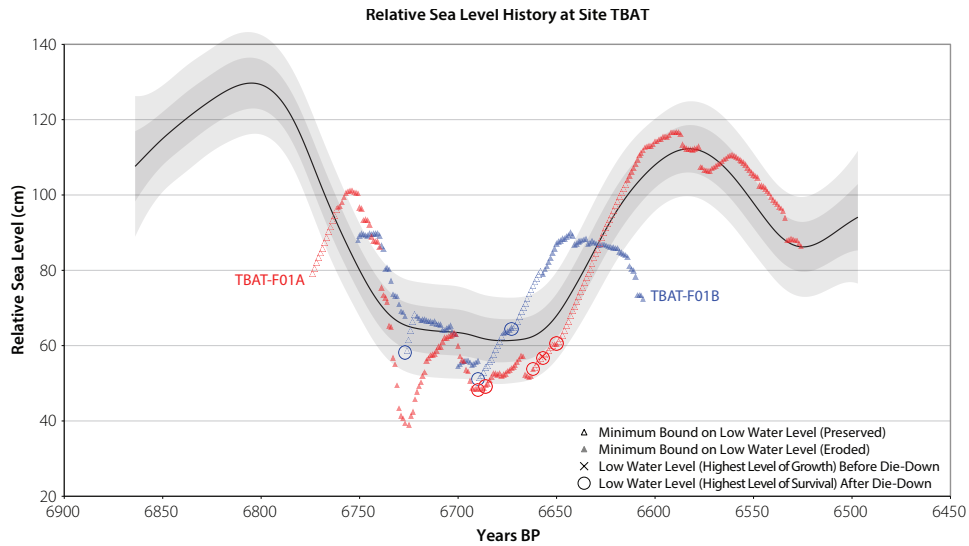


Figure 4.6: Mid-Holocene RSL proxy time series determined from the TBAT-F01 microatoll at the TBAT site on southeastern Belitung. Data from each of two slabs are shown in a different color. The relative age uncertainty between two observations at this site is simply the annual band-counting uncertainty, commonly less than ± 1 yr; however, unmodeled uncertainty in ΔR could affect absolute ages and would allow the entire curve to be shifted uniformly by up to ± 85 yr. In particular, ΔR at TKUB may differ from ΔR at TBAT within the bounds of uncertainty. Overlain on the data is the posterior estimate of the common regional RSL signal with the periodic term removed, conditioned upon all index points (HLS data; open circles) and the highest minimum limiting data point (triangles) within each 18.61-yr bin. Vertical uncertainties about each data point are uniformly ± 9 cm (1σ) but are not shown here for clarity. For the models, dark and light shading depict $\pm 1\sigma$ and $\pm 2\sigma$ error envelopes, respectively.

of prominent diedowns on the various microatolls between any two dates. The advantage of correlating the annuli manifests when considering the handful of U-Th ages in their study that had sizable errors. In the few cases where the chronological errors were so large that the sample age overlapped with sample ages from adjacent annuli, our effort to group the age-elevation data based on the coral morphologies allowed us to minimize the ambiguity of whether a particular sample belonged on one downward swing of the RSL curve or on the subsequent upward swing (Figure 4.9).

4.3.2 Model cross-validation

Cross-validation is used to compare the performance of different predictive modeling procedures. For the preferred model (Figure 4.8), we performed an exhaustive (64 runs, one for each training point) Leave-One-Out Cross-Validation of the model (. Since the model is tuned to envelop 95% of the data, we expect the point that is left out of the optimization of the model to be included $\sim 95\%$ of the time. Table 4.1 shows the number and percentage of data points that were within the 95% interval of our model's posterior predictive

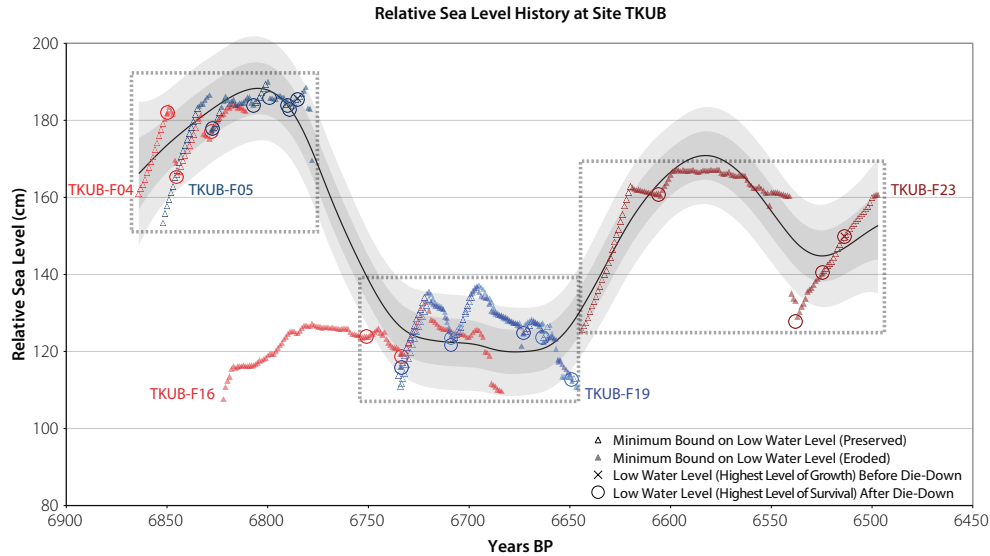


Figure 4.7: Mid-Holocene RSL proxy time series determined from coral microatolls at the TKUB site on northwestern Belitung, as in Figure 4.6, but with the timing of each discrete floating chronology (indicated by a dotted box) optimized by our model relative to the timing of the TBAT time series (Figure 4.8). Colors correspond to data from different corals. ΔR did not vary over the lifetime of corals at this site, and therefore uncertainty in ΔR can be ignored when calculating the relative (differential) age of these corals; however, unmodeled uncertainty in ΔR could affect absolute ages and would allow the entire curve to be shifted uniformly by up to ± 85 yr. In particular, ΔR at TKUB may differ from ΔR at TBAT within the bounds of uncertainty. Overlain on the data is the posterior estimate of the common regional RSL signal, conditioned upon all index points (HLS data; open circles) and the highest minimum limiting data point (triangles) within each 18.61-yr bin. Vertical uncertainties about each data point are uniformly ± 9 cm (1σ) but are not shown here for clarity. For the models, dark and light shading depict $\pm 1\sigma$ and $\pm 2\sigma$ error envelopes, respectively.

distribution. The model achieved 92.2% inclusion within the prediction interval. In addition, Table 4.1 shows the mean, median and median absolute value of all of the differences (or residuals) between predicted RSL and sea-level height of the data point. For the mean and median, over-predictions and under-predictions tend to cancel one another out, so values near zero suggest that the differences are randomly distributed. For a model that treats each training point as a sea-level index point, we expect such behavior. The median absolute error is the median of the absolute value of each difference, so values near zero suggest better predictive power of the model.

4.4 Results

We model the RSL proxy reconstructions as a combination of a shared non-linear signal and a site-specific offset, plus a periodic term to model microatoll growth over the 18.61-year tidal cycle. We constructed

Table 4.1: Model cross validation

Observations	95% Prediction Interval			Mean	Errors (mm)	
	Below	Within	Above		Median	Median Absolute
Actual Count (out of 64)	2	59	3	-1.1	7.5	64.7
Actual Percentage	3.1%	92.2%	4.7%			
Expected Count (out of 64)	1.6	60.8	1.6	0	0	
Expected Percentage	2.5%	95%	2.5%			

a hierarchical statistical model after Kopp et al. (2016), separated into three levels: a data level, which models the recording of RSL by proxies; a process level, which models RSL at the different sites; and a parameter level, which characterizes key attributes of the underlying RSL processes. This model optimizes the relative timing of each floating chronology, subject to appropriate radiocarbon dating constraints. It also allows separation of the non-linear and periodic signals and the site-specific offset. Details are given in the Statistical Methods, Section 4.3. The optimized model appears in Figure 4.8 with the chronologically optimized time series from the TKUB site.

In the end, the model based on our preferred strategy (selecting a subset of the coral data as index points) does a reasonable job of separating the non-linear and periodic signals (Figure 4.4), and the rates of RSL change it estimates should reflect secular trends, minimally biased by vagaries of coral growth variability over the 18.61-year tidal cycle. The alternative model, with a larger subset of data, selecting the maximum limiting point at each year (Figure 4.5), in contrast, does a poor job of separating out the periodic term, and it forces more high-frequency variability into the non-linear signal, likely overestimating short-term rates of sea-level change. Although we suspect that the high-frequency variability (period ~ 30 years) seen only in the alternative model (Figure 4.5c) is an artifact of that model trying to fit limiting data that severely underestimate theoretical HLS, the fact that both strategies yield fluctuations at a 200-year timescale with peak-to-trough amplitudes of 0.5-0.7 m and similar timing suggests that these model results are robust.

4.4.1 Common signal

Holding the timing of the TBAT curve fixed, we optimized three floating chronology shifts, assuming $\Delta R = \pm 89$ years. The TKUB curve is shifted 54 years older overall; the oldest floating chronology at TKUB (TKUB-F04 and TKUB-F05) is shifted an additional 20 years older relative to the central floating chronology (TKUB-F16 and TKUB-F19); and TKUB-23 is shifted 1 year younger relative to TKUB-F16 and TKUB-F19 (Figures 4.7 and 4.8). The 54-year shift of the overall TKUB curve is reasonable given that it is well within the ± 85 -year unmodeled error in ΔR , and the 20- and 1-year shifts between the floating chronologies at TKUB are at the limit of what is permitted by the uncertainties of the various 2σ calibrated radiocarbon age errors.

Collectively, the corals provided 25 sea-level index points (HLS elevations following diedowns) and annual

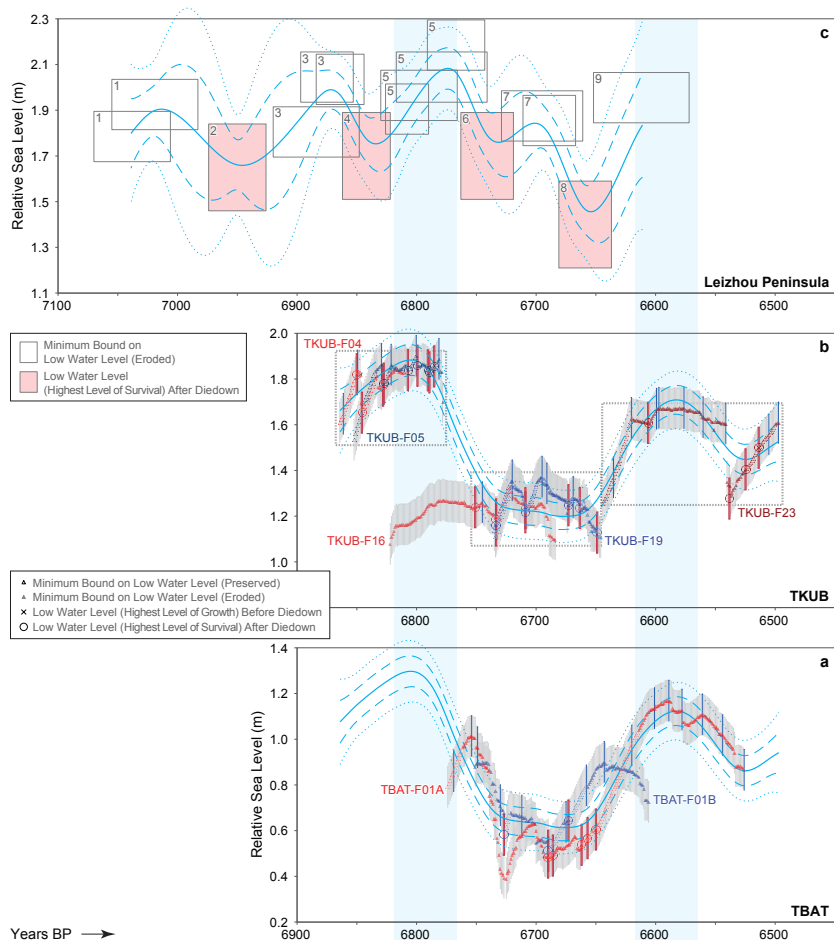


Figure 4.8: Modeled RSL histories. Posterior estimates of mid-Holocene RSL from the optimized model for the three sites: (a) TBAT; (b) TKUB; (c) Leizhou Peninsula (Yu et al., 2009). For TKUB, the timing of each discrete floating chronology (indicated by a dotted box) is shifted from based on model optimization. Unmodeled uncertainty in ΔR could allow the results for sites TKUB and TBAT to be shifted uniformly by several additional decades, allowing for a slightly improved fit (cyan bars) between the RSL histories at those sites and at the Leizhou Peninsula site. At Leizhou Peninsula, microatoll morphologies allow us to place groupings of data points (numbered 1-9 in the upper left corner of each box) in chronological sequence; this sequence was imposed on the reported U-Th ages (Meltzner et al., 2017), and the ages were then refined using the computer program OxCal (Ramsey, 2008). Amplitude hyperparameters for the Leizhou Peninsula site were scaled by a factor of 2 compared to those at the TKUB and TBAT sites, to compensate for poorer data quality at Leizhou Peninsula. Data show $\pm 1\sigma$ vertical and $\pm 2\sigma$ chronological uncertainties; dashed and dotted model curves depict $\pm 1\sigma$ and $\pm 2\sigma$ error envelopes.

minimum limiting data (minimum bounds on the theoretical HLS) for a span of ≥ 350 years (Figure 4.8). The results suggest an initial RSL peak at $\sim 6,800$ cal years BP; RSL then fell ~ 0.6 m and remained at a lowstand for 80-100 years, before rising 0.4-0.6 m to a second peak at $\sim 6,590$ cal years BP. Corals at TKUB record a second drop at $\sim 6,530$ cal years BP, with a third peak shortly thereafter. Although no data exist

from this later period at TBAT, this second drop in RSL could explain the death of TBAT-F01 at $\sim 6,530$ cal years BP.

The peak rate of RSL rise, averaged over a 20-year running time window over the period of study ($\sim 6,850$ - $6,500$ cal years BP), is $+9.6 \pm 4.2$ mm per year (2σ); the peak rate of RSL fall is 12.6 ± 4.2 mm per year (table X). If the 21-year shift between the floating chronologies at TKUB were reduced as contemplated in the previous paragraph, the peak rate of RSL fall ($\sim 6,770$ cal years BP) would be even faster.

4.4.2 Site-specific offset between TKUB and TBAT

Several possible mechanisms could explain the systematically higher elevations at the TKUB site. The primary cause of this offset is the interplay between two processes of glacial isostatic adjustment (GIA) that drove RSL change at far-field sites during the mid-Holocene: equatorial ocean syphoning and continental levering (Mitrovica and Peltier, 1991; Mitrovica and Milne, 2002). The possible mechanisms are discussed further in Meltzner et al. (2017).

4.4.3 Comparison to distal records

The Belitung RSL record is the highest resolution in the mid-Holocene yet obtained in East or Southeast Asia. Only one previous study from the region (Yu et al., 2009) resolves centennial-scale sub-meter fluctuations in RSL prior to 6000 cal yr BP. Interestingly, that dataset – a RSL history from southern China based on the surveyed elevations of the upper surfaces of coral microatolls – tells a story of similar rapid oscillations. We reinterpreted the published RSL curve, considering not only the upper surfaces of the microatolls but also the coral diedowns. The RSL curves from southern China and Belitung are plotted together in Figure 4.8 and all suggest a peak in RSL ~ 6800 cal yr BP, followed by a trough in RSL ~ 0.6 m lower, and then a second RSL peak ~ 6590 cal yr BP, ~ 0.2 m lower than the first. Additional minor fluctuations at the southern China site, with an intermediate peak ~ 6700 cal yr BP, may reflect additional complexity in ocean circulation that has a more profound impact north of Belitung Island.

4.5 Discussion

The similarities between the RSL curves from Belitung Island on the Sunda Shelf and from the southern coast of China, 2,600 km to the north, suggest that the records reflect widespread changes in sea level. To put the ~ 0.6 m mid-Holocene fluctuations in context, annual mean sea level in some modern tide-gauge records is seen to change by as much as 0.2-0.3 m on interannual timescales (Church and White, 2006), and the interannual s.d. of sea surface height between 1979 and 2013 approached 0.1 m in some portions of the

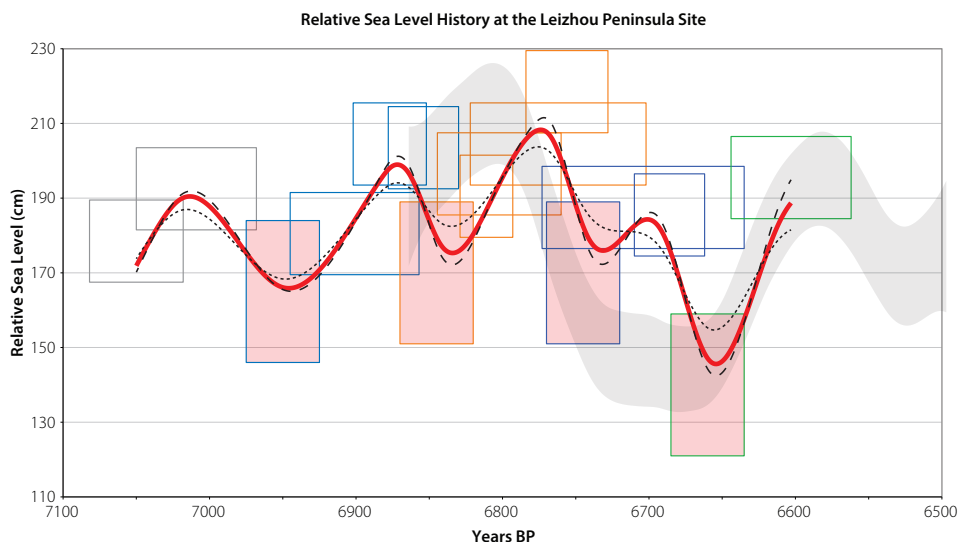


Figure 4.9: Reinterpreted RSL history at the Leizhou Peninsula site of Yu et al. (2009). The boxes with shaded red fill represent the four diedowns reflected in the microatoll morphology at the site. Dated samples, each tied to a surveyed elevation, are shown by open boxes, with 1σ vertical errors and 2σ temporal errors. All boxes are color-coded (for ease of visualization) to correspond to one of the sequential sea-level drops required by microatoll diedowns at the site, and the subsequent sea-level rise. Yu et al. (2009) did not consider the diedowns in their interpretation, nor did they consider the detailed morphology of the individual microatolls, but observations presented in their paper allow us to reconstruct the history as shown here. The solid red curve is our preferred model, with amplitude hyperparameters scaled by 2, as discussed in the Methods; dotted and dashed curves are the unscaled model, and the model with amplitude hyperparameters scaled by 3. Overlain on the plot is the Belitung RSL curve from Figures 4.8 (2σ error envelope in gray); the Belitung curve is shifted vertically to optimize the fit, but there has been no temporal shift. A different choice of ΔR for the TBAT site, which pins the timing of the Belitung chronology, would allow for a temporal shift of the Belitung curve and could improve the agreement between the sites further.

western Pacific (Widlansky et al., 2015). Using coupled climate models, Widlansky et al. (2015) project a 5-25% increase in the interannual standard deviation over most of that region for 2006-2100. Many of the regions of high sea-level variability were also areas of extraordinarily high rates of sea-level rise (approaching 30 mm per year) between 1993 and 2001 (Church and White, 2004), though those high rates have been shown to be biased by the aliasing of interannual and decadal variability into linear sea-level trends over the brief period of observation (Zhang and Church, 2012; White et al., 2014). Although the highest 1993-2001 rates are higher than those inferred from the mid-Holocene corals, the mid-Holocene rates were averaged over and sustained for considerably longer periods of time. Indeed, the amplitude of the mid-Holocene fluctuations on the Sunda Shelf and in the South China Sea exceeds any observed there in modern times. On the Great Barrier Reef in Australia, reconstructions of centennial scale ≥ 0.3 -m RSL fluctuations 5,500-5,100 years BP (Leonard, 2016), and 4,800-4,500 and 3,000-2,700 cal years BP (Lewis et al., 2008) suggest that oscillations may be more common than previously appreciated, particularly in the tropics, but sufficiently

high-resolution RSL proxy records are needed to identify them. If a similar oscillation were to occur in East and Southeast Asia in the next two centuries, it could directly impact tens of millions of people and associated infrastructure. If this oscillation were to begin with a RSL fall, it would (in the short term) mitigate regional effects of projected eustatic sea-level rise. But if it were to begin with a pronounced RSL rise, this would occur on top of, and exacerbate the effects of, projected long-term global sea-level trends.

The observed RSL fluctuations may result from changes in dynamic sea surface height, local steric effects or eustatic changes. The Southeast Asia-Northern Australia region has considerable interannual and decadal sea-level variability associated with phenomena such as ENSO, the Pacific Decadal Oscillation and the Asian-Australian monsoon (Church and White, 2006; Zhang and Church, 2012; White et al., 2014; Strassburg et al., 2015). Over the 17-year period from 1993 to 2009, ENSO and Pacific Decadal Oscillation-related signals raised sea-level trends by 4-6 mm per year north of Australia and by up to 12 mm per year in the tropical western Pacific. Effects of interannual and decadal climate variability on the Sunda Shelf and South China Sea have been smaller, but still significant (~ 2 mm/yr), since 1993 (Zhang and Church, 2012). If either of these climate oscillations entered a persistent strengthened or weakened state over sufficiently long timescales during the mid-Holocene, it is conceivable that they contributed to the sea-level fluctuations observed on Belitung and in southern China, through either dynamic or steric changes in sea level. A coral-based proxy record of tropical Pacific climate variability over the past 1,100 years reveals variations in the strength and frequency of ENSO activity at multi-decadal to centennial timescales – suggesting that variability in ENSO at relevant timescales is physically possible – but the amplitude of sea-level variability in Southeast Asia that would result from such climate fluctuations is unknown. Alternatively, the sea-level fluctuations documented in our study might have been triggered by a shift of the Inter-Tropical Convergence Zone, which would affect the strength of the monsoon. Today, sea-level extremes in the South China Sea (up to ± 0.25 m) are primarily monsoon driven, but it is unclear how this would be different under a stronger or weaker monsoon. Unfortunately, the poorer temporal resolution of existing regional paleoclimate proxy data from the mid-Holocene limits our ability to make meaningful comparisons. If the 0.6-m amplitude fluctuations within decades are a global signal, then they imply a heretofore-unknown instability in the mid-Holocene global ice budget. Beyond Southeast Asia, existing ice and sea-level records do not have the necessary resolution to test such a hypothesis (members, 2004; Parrenin et al., 2007), and models are equivocal as to whether such fluctuations are permissible (Golledge et al., 2014). High-resolution RSL proxy records from other tectonically stable sites in Southeast Asia, and records spanning more recent time periods, would permit a better understanding of the spatial scale of these sea-level oscillations and could provide insight into whether the period from 6,850 to 6,500 cal years BP was unique.

Chapter 5

Conclusions and further work

The hierarchical statistical models and innovations presented within this thesis suggest several prospective applications and directions for future research. In chapter 3, I illustrated the incorporation of non-Gaussian RSL proxies in a temporal hierarchical model in a location where RSL is well-constrained by a range of different proxies. The true utility of this framework, however, relates to spatio-temporal modeling in locations where other proxies, more conventionally modeled using statistical approaches, are not available. For example, applying the model to a deglacial dataset, such as the Barbados coral record (e.g., Abdul et al., 2016), will improve estimates of RSL and address open questions about melt-water pulses during the deglacial period (e.g., Blanchon, 2017). Adding a spatial component to the model can open up a wide range of opportunities to answer questions about the variability of sea level in the past by incorporating data from far-field and near-field locations that have previously been underutilized. In particular, applying a spatio-temporal version of the model introduced in chapter 3 to a pole-to-pole transect could help to constrain GIA. Similarly, applying the model to a region where GIA has large variability over short geographic scales, such as the region examined in Vacchi et al. (in review), could also help constrain GIA and ice-history parameters.

Spatio-temporal hierarchical models can be enriched by integrating knowledge about the physical drivers of RSL change into the process level of statistical models. One context in which this is useful is modeling RSL in situations where the data are quite sparse and the prior thus wields strong influence on the inferred spatio-temporal structure. Another context is where the goal is to infer the processes driving RSL change – for example, to constrain the solid-Earth or ice-history parameters of a model of glacial isostatic adjustment. Statistical emulation of complex physical models, including 1-D and 3-D GIA models and ice-sheet models, could provide a flexible way of explicitly embedding this knowledge in a hierarchical framework. Statistical emulation reduces the processing time of these physical models, which are computationally intensive; it produces continuous output, in contrast to the discrete sea-level curves that are output for each set of discrete input parameters; and it enables probabilistic conclusions about the input parameters driving the physical models. For example, applying an integrated hierarchical model with an emulated process level to datasets from the Last Interglacial could both yield a reassessment of GMSL during a time period analogous to the present and constrain the physical model parameters for use in improving the projections of future

sea-level rise.

A key methodological challenge is scaling spatio-temporal hierarchical modeling approaches for paleo-sea level data to large, yet still temporally noisy, datasets. Unlike Gaussian process models, whose computational complexity grows in proportion with the cube of the number of data points, the computational complexity of a Kalman smoother grows linearly. Adapting the Kalman smoother for temporally noisy data may provide an approach to overcoming the scaling problems described in chapter 2 and thus allow the simultaneous analysis of much larger proxy datasets. Recent work in the machine-learning literature exploring the translation between Gaussian process models and linear-Gaussian state space models (e.g., Hartikainen and Särkkä, 2010) may prove useful here. There are also several approximation and estimation techniques in the GP and machine-learning literature that have not yet been applied in a sea-level context, such as variational inference (Blei et al., 2017), which could speed up analyses and improve resolution with large datasets.

Appendix A

Supplement to Chapter 2

A.1 Covariance functions

Spatio-temporal covariance functions define a correlation (shared information) through time and space, which decays as the temporal and spatial distances increase (Rasmussen and Williams, 2006). Some frequently used covariance functions for modeling RSL using GPs include dot-product (e.g., Khan et al., 2017), powered-exponential (e.g., Cahill et al., 2015a), rational quadratic (e.g., Kopp, 2013; Hay et al., 2015), and Matérn (e.g., Hay et al., 2015; Khan et al., 2015; Kopp et al., 2016; Khan et al., 2017) function. Each covariance function has distinct characteristics and requires different parameters. For example, a dot-product covariance function ($K(t_1, t_2) \propto t_1 \cdot t_2$) produces a linear trend, which would be appropriate to model GIA over centennial scales. A squared-exponential covariance function ($K(t_1, t_2) \propto e^{-\frac{(t_2-t_1)^2}{\theta}}$) is infinitely differentiable, and is thus very smooth. Therefore the squared-exponential function would be inappropriate for tectonics, since it would not adequately capture the abrupt changes. The powered-exponential covariance function (see equation A.1) and the Matérn (see equation A.2) family of functions are highly generalizable and allow specification of the degree of differentiability (and therefore smoothness), while having a small number of parameters:

$$K(t_i, t_j) = \nu^2 \rho^{|t_i - t_j|^\kappa} \tag{A.1}$$

where $\rho \in (0, 1)$ is the correlation parameter and $\kappa \in (0, 2]$ is the smoothness parameter. The IGP employed in Cahill et al. (2015a) placed a zero-mean GP prior, with a powered-exponential covariance function on the rate process $f'(t)$. The squared-exponential function is powered-exponential with a smoothness parameter of two. As the smoothness parameter decreases, the function becomes more rough. For the Matérn,

$$k_{Matern}(r) = \frac{2^{1-\nu}}{\Gamma\nu} \left(\frac{\sqrt{2\nu}r}{l} \right)^\nu K_\nu \left(\frac{\sqrt{2\nu}r}{l} \right), \tag{A.2}$$

where r is the difference in time or space, ν is a positive smoothness parameter, l is a positive characteristic length-scale parameter, and K_ν is a modified Bessel function. When ν is a half-integer, the covariance

function is the product of an exponential and a polynomial, and it is simpler. For example,

$$k_{\nu=3/2}(r) = \left(1 + \frac{\sqrt{3}r}{l}\right) \exp\left(-\frac{\sqrt{3}r}{l}\right), \quad (\text{A.3})$$

$$k_{\nu=5/2}(r) = \left(1 + \frac{\sqrt{5}r + \frac{5r^2}{3l^2}}{l}\right) \exp\left(-\frac{\sqrt{5}r}{l}\right), \quad (\text{A.4})$$

There is some trade-off between the Matérn exponent values and the characteristic length scale parameter: the selection of a lower exponent (which creates a less smooth function) is somewhat comparable to a longer length scale with a greater exponent (Hay et al., 2015).

The sum of several covariance functions can be used to model the RSL field, with each term separated by spatial or temporal scales. While it may not be possible to explicitly distinguish between sea-level processes through the characteristic scale hyperparameters alone, information from physical models can be incorporated into the covariance structure of GPs. For example, in the GP model from Hay et al. (2015), the melt component $M(\mathbf{x}, t)$ was the sum of individual ice sheets or mountain glaciers, where each had a linear term and a rational quadratic term, both of which were dependent in time. The sum of the two terms was multiplied by a spatial weighting B^M , which applied the sea-level fingerprint associated with the melt for each land-based ice source. The covariance of the GP prior for the melt was:

$$\sum_{j=1}^n M(\mathbf{x}, t) = \sum_{j=1}^n \left(m_a \cdot \Delta t_{q,p} + c \left(1 + \frac{\Delta t_{q,p}^2}{2\alpha\tau_M^2} \right)^{-\alpha} \right) B^M \quad (\text{A.5})$$

where j represents each ice sheet or glacier, t_q and t_p represent the time at the q th and p th time step, $\Delta t_{q,p}$ represents the time difference between the steps, and m , c , α , and τ_M are hyperparameters that defined the prior standard deviation of the linear rate, the prior standard deviation on non-linear variability and the roughness and characteristic timescale of non-linear variability. These parameters were estimated by maximizing their likelihood, using published reconstructions of the time series of glacier and ice sheet estimates.

The choice of prior covariance function(s) characterize stationarity, isotropy, smoothness, and periodicity in Gaussian processes (2.5.3). For a full treatment of covariance functions, see Rasmussen and Williams (2006), Chapter 4.

A.2 Analysis choice details

A.2.1 Regional averaging

One form of regional averaging separates the ocean into pre-defined oceanic regions or basins. The methodology averages two monthly-mean tide gauges together, creating a virtual station located at the halfway point between the two original stations. This averaging is repeated until one virtual station exists in each region. The global average is then computed by averaging all of the virtual stations. Jevrejeva et al. (2006, 2008) also removed 2-30 year variability using a method based on Monte Carlo Singular Spectrum Analysis.

In an extension of the original virtual station technique of Jevrejeva et al. (2006, 2008), Dangendorf et al. (2017) computed regional mean sea-level rates from subsets of tide gauges after first correcting for processes that affect RSL and SSH, such as GIA, vertical land motion, and geoid changed due to glacier melting. The regional averages were then combined by weighting each region by the area of the ocean it represents.

A.2.2 Kalman smoother

In the Kalman smoother, \mathbf{y}_k , which are observations of RSL at each time step taken from a global network of tide gauge sites, are modeled as:

$$\mathbf{y}_k = \mathbf{H}\mathbf{x}_k + \mathbf{v}_k \quad (\text{A.6})$$

where the observation matrix, \mathbf{H} , maps the state vector into the observation space, and the measurement noise, \mathbf{v}_k , is assumed to have a mean of zero with covariance \mathbf{R} .

Equation 2.13 can be reframed in KS terminology, where the spatial sea-level field \mathbf{f}_k is a vector of local RSLs at time step k and locations of interest, and β_k is a vector that contains the melt rates M_j of 18 mountain glaciers, 3 ice sheets, and a globally uniform term, $g(t)$. At each time step, the filter constructs a prior estimate of the state vector, \mathbf{x}_k , defined as:

$$\mathbf{x}_k = \begin{bmatrix} \mathbf{f}_k \\ \beta_k \end{bmatrix} = \mathbf{\Phi}\mathbf{x}_{k-1} + \mathbf{B}\mathbf{u}_k + \mathbf{w} \quad (\text{A.7})$$

where $\mathbf{\Phi}$ is the state transition matrix, \mathbf{u}_k is the input control parameter, \mathbf{B} maps the input control parameter into the state vector, and \mathbf{w} is the zero-mean process noise with covariance \mathbf{Q} . The normalized sea-level fingerprints (FP_j from equation 2.13), which connect local RSL to the eustatic melt rates being estimated, are contained in $\mathbf{\Phi}$, and \mathbf{u}_k includes the rates of local sea-level change controlled by both GIA and ocean dynamics (see Hay et al., 2013 for an explicit description of each matrix).

The Kalman filter consists of two main steps: the time update step and the measurement update step. In the time update step, the filter constructs a prior estimate of the state vector, $\hat{\mathbf{x}}_k^-$, and its covariance, \mathbf{P}_k^- , at time step k conditioned upon the state vector at time $k-1$. The superscript minus sign, $-$, indicates that the estimate is computed in the time update stage (prediction) and represents the prior estimate of the states.

$$\hat{\mathbf{x}}_k^- = \Phi \mathbf{x}_{k-1} + \mathbf{B} \mathbf{u}_k \quad (\text{A.8})$$

$$\mathbf{P}_k^- = \Phi \mathbf{P}_{k-1} \Phi^T + \mathbf{Q} \quad (\text{A.9})$$

The time update step, described by equations A.8 and A.9, contains all the process-based physical models of the drivers of sea-level change.

In the measurement update step, the prior estimates, $\hat{\mathbf{x}}_k^-$ and \mathbf{P}_k^- , are conditioned upon the available observations \mathbf{z}_k at time k . The goal is to find the optimal estimate of the state vector, $\hat{\mathbf{x}}_k$, and covariance, \mathbf{P}_k , that combines the prior estimates with the observations:

$$\hat{\mathbf{x}}_k = \hat{\mathbf{x}}_k^- + K_k (\mathbf{z}_k - \mathbf{H} \hat{\mathbf{x}}_k^-) \quad (\text{A.10})$$

$$\mathbf{P}_k = (\mathbf{I} - \mathbf{K}_k \mathbf{H}) \mathbf{P}_k^- \quad (\text{A.11})$$

Here \mathbf{K}_k is the Kalman gain matrix defined as

$$\mathbf{K}_k = \mathbf{P}_k^- \mathbf{H}^T (\mathbf{H} \mathbf{P}_k^- \mathbf{H}^T + \mathbf{R})^{-1} \quad (\text{A.12})$$

The prediction and measurement steps (equations A.8, A.9, A.10, and A.11) are recursively computed through time until all observations have been assimilated (Kalman, 1960).

Once the forward pass is complete, the Kalman filter is run backwards in time and a weighted combination of the forward and backwards passes is computed. This three-pass-filter (Gelb et al., 1974) ensures that in every year the optimal estimate of the state vector and its covariance includes all observations over the analysis time window.

The final component of the multi-model Kalman smoother implemented by Hay et al. (2015) is the multi-model step. In this step, the likelihood of obtaining the observations, given the model, is computed. These probabilities are then used to compute a weighted sum of the Kalman smoother estimates (Blom and Barshalom, 1988).

Within the KS terminology, the state vector \mathbf{x} contains $g(t)$, and Φ contains $M(\mathbf{x}, t)$, whereas \mathbf{u} maps to $DSL(\mathbf{x}, t)$ and $GIA(\mathbf{x}, t)$ from equation 2.13.

In Hay et al. (2015), the melt rates $M_j(\mathbf{x}, t)$ along with their associated covariance, are summed to produce an estimate of GMSL over the 20th century. Unmodeled local processes, such as tectonics and groundwater withdrawal, are not explicitly modeled in the Kalman smoother and are therefore not mapped into GMSL. Instead, these unmodeled effects are captured by the process noise term. While the unmodeled local processes are not included in GMSL, they are present in the Kalman-smoother reconstructed tide gauge and global sea-level time series. An alternative approach for reconstructing the local sea-level time series is to use the Kalman smoother posterior estimates of the melt rates (with the normalized fingerprints), uniform sea-level change, GIA, and ocean dynamics. The site-specific components of each of these processes can be summed together to reconstruct the local sea-level field. This field will not contain the local processes that are observed in the data since they are not mapped into the individual components estimated in the smoother. It will, therefore, be an inherently smoother reconstruction and will have lower uncertainties than the field estimated within the Kalman smoother (Hay et al., 2017).

A.3 Details of implementations

The hyperparameters for each of the time-series implementations are summarized in figure A.1.

Table A.1: RSL predictions (m) with 95% CI below from EST-GPR

Site	Lat	Lon	14 ka	13 ka	12 ka	11 ka	10 ka	9 ka	8 ka	7 ka	6 ka	5 ka	4 ka	3 ka	2 ka	1 ka	0 ka												
New Jersey	39.09	284.77	-59.0	-51.2	-43.0	-35.1	-28.1	-22.4	-18.2	-14.6	-11.4	-9.1	-7.0	-4.9	-3.4	-1.7	-0.1												
			-63.9	-54.1	-47.8	-45.3	-40.7	-36.7	-33.5	-29.2	-27.0	-23.1	-21.6	-18.7	-17.7	-15.1	-14.1	-11.8	-11.0	-9.4	-8.8	-7.3	-6.7	-5.2	-4.7	-3.6	-3.2	-1.9	-1.6
North Carolina	34.98	283.8	-53.1	-45.2	-36.9	-29.0	-22.0	-16.4	-12.5	-9.4	-6.9	-5.4	-4.2	-2.9	-2.0	-1.3	0.1												
			-57.5	-48.7	-48.0	-42.4	-38.6	-35.2	-30.2	-27.7	-23.1	-20.8	-17.5	-15.3	-13.5	-11.4	-10.3	-8.5	-7.6	-6.2	-5.9	-4.8	-4.6	-3.7	-3.2	-2.5	-2.2	-1.8	-1.4
Inner Delaware	38.75	284.88	-58.6	-50.8	-42.5	-34.7	-27.7	-22.0	-17.8	-14.3	-11.2	-8.9	-6.9	-4.9	-3.4	-1.7	-0.1												
			-57.5	-48.7	-48.0	-42.4	-38.6	-35.2	-30.2	-27.7	-23.1	-20.8	-17.5	-15.3	-13.5	-11.4	-10.3	-8.5	-7.6	-6.2	-5.9	-4.8	-4.6	-3.7	-3.2	-2.5	-2.2	-1.8	-1.4

Table A.2: Predicted rates (m/ky) averaged over 1000 year periods from EST-GP with 95% CI below

	13-14 ka	12-13 ka	11-12 ka	10-11 ka	9-10 ka	8-9 ka	7-8 ka	6-7 ka	5-6 ka	4-5 ka	3-4 ka	2-3 ka	1-2 ka	0-1 ka													
New Jersey	7.8	8.2	7.9	7.0	5.7	4.2	3.6	3.2	2.3	2.1	2.1	1.5	1.7	1.7													
	5.9	9.7	6.7	9.7	6.8	9.0	6.2	7.8	5.1	6.4	3.7	4.7	3.2	4.0	2.8	3.6	2.0	2.7	1.8	2.4	1.8	2.4	1.2	1.8	1.5	1.9	1.5
North Carolina	8.0	8.3	7.9	7.0	5.5	4.0	3.1	2.5	1.5	1.2	1.3	0.9	0.7	1.3													
	6.07	9.8	6.8	9.8	6.9	9.0	6.3	7.7	5.0	6.1	3.5	4.5	2.6	3.6	2.0	2.9	1.1	2.0	0.8	1.6	0.9	1.7	0.6	1.2	0.5	1.0	1.2
Inner Delaware	7.8	8.2	7.9	7.0	5.7	4.2	3.5	3.1	2.2	2.0	2.0	1.5	1.7	1.6													
	5.9	9.7	6.7	9.7	6.8	9.0	6.2	7.8	5.0	6.3	3.6	4.7	3.1	4.0	2.7	3.5	1.9	2.6	1.7	2.4	1.7	2.3	1.2	1.7	1.5	1.9	1.5

A.4 Data

The data used in the models of chapter 2 can be found in the following file:

Holocene_Data.xlsx

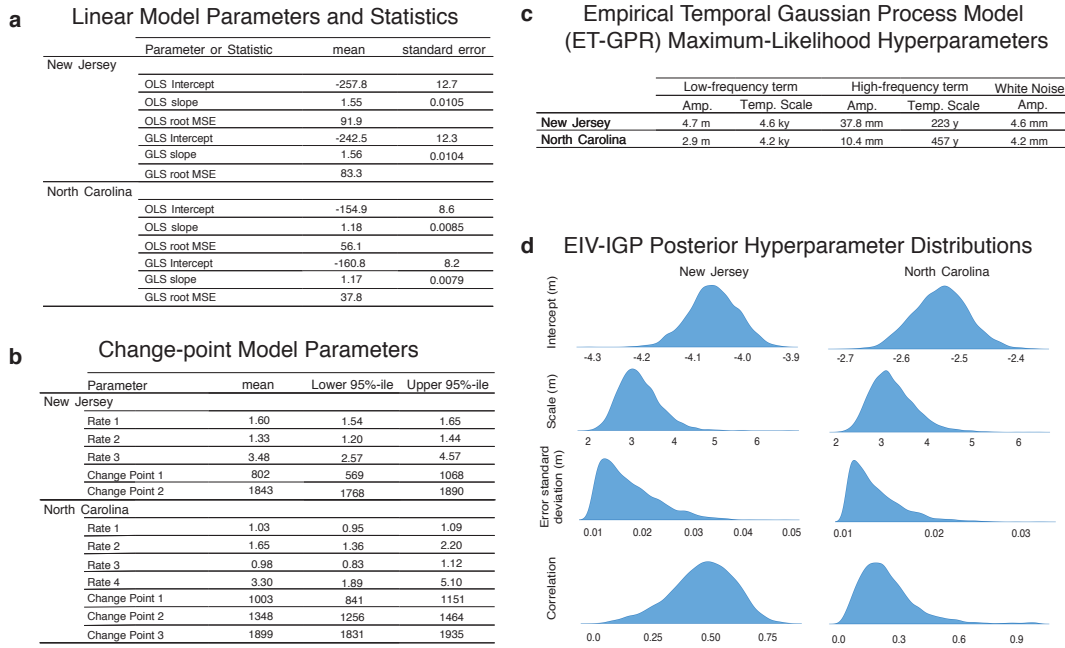


Figure A.1: (a) Table showing linear model parameters and statistics, including intercept and slope with their standard errors and root mean squared error, for two versions of least-squares linear implementation (OLS and GLS). (b) Table showing change points fit to continuous core records at New Jersey and North Carolina, where the mean and 95% credible intervals are shown for the rates and change points. (c) Bayesian EIV-IGP posterior distributions of hyperparameters for each of the independent models at New Jersey and North Carolina. The intercept is α in equation 2.9, the scale is ν in equation A.1, the error standard deviation is σ as in equation 2.3, and the correlation is ρ from equation A.1. (d) Table of maximum-likelihood hyperparameters for independent empirical-temporal GP models in New Jersey and North Carolina, including prior amplitude and temporal-scale parameters of the low-frequency and high-frequency terms, the white noise amplitude.

Appendix B

Supplement to Chapter 3

Caribbean-wide coral distributions	Normal	Exponential	Half Normal	Log-Normal	Minimum AIC
<i>Acropora palmata</i>	29946.6	22523.7	24798.8	21696.1	21696.1
<i>Colpophyllia natans</i>	16812.3	15421.3	15543.7	15024.3	15024.3
<i>Pseudodiploria clivosa</i>	10061.6	8392.9	8919.8	8291.1	8291.1
<i>Diploria labyrinthiformis</i>	11438.9	10451.5	10560.0	10431.7	10431.7
<i>Pseudodiploria strigosa</i>	37151.9	32951.6	33826.3	33644.4	32951.6
<i>Montastraea cavernosa</i>	47519.0	42346.2	43459.2	42555.2	42346.2
<i>Orbicella</i> spp.	98444.0	110438.8	104478.2	107321.7	98444.0
<i>Porites astreoides</i>	74356.4	64261.0	66893.8	64449.2	64261.0
<i>Siderastrea siderea</i>	53605.7	48437.6	49251.6	48702.6	48437.6

Florida-specific coral distributions	Normal	Exponential	Half Normal	Log-Normal	Minimum AIC
<i>Acropora palmata</i>	693.9	850.0	780.6	560.3	560.3
<i>Colpophyllia natans</i>	1009.2	1096.9	1041.6	961.4	961.4
<i>Pseudodiploria clivosa</i>	698.4	730.3	694.9	616.5	616.5
<i>Diploria labyrinthiformis</i>	298.8	309.3	297.4	268.3	268.3
<i>Pseudodiploria strigosa</i>	578.6	619.2	589.2	567.2	567.2
<i>Montastraea cavernosa</i>	2681.9	3060.6	2878.1	2647.4	2647.4
<i>Orbicella</i> spp.	4212.1	3828.8	3822.4	3584.3	3584.3
<i>Porites astreoides</i>	4022.9	3941.0	3813.8	3677.5	3677.5
<i>Siderastrea siderea</i>	3509.6	3514.9	3391.2	3387.5	3387.5

Figure B.1: Akaike information criteria (AIC) for Caribbean-wide and Florida-specific distributions, where the highlighted box indicates which distribution fits the data best, out of the parametric distributions tested, according to the AIC.

In cases where the modern elevation data are insufficient to justify using a nonparametric distribution, a parametric distribution, such as the log-normal density, can be substituted.

B.1 Parametric distributions of living Caribbean corals

B.1.1 Local variability of coral distributions

The regional-scale analyses of *A. palmata*, *Orbicella* spp., and *P. clivosa* suggest that there is considerable variability in the depth distributions of Caribbean corals by location. The fitted parametric depth distributions of *A. palmata* are approximately log-normal for all five locations; however, there are regional differences

in the fitted distributions (Figure B.2). Whereas the peak abundances of this taxon are at similar depths to the Caribbean-wide mode (-0.8 m MSL) in the Bahamas (-0.9 m MSL), southern Cuba (-0.7 m MSL), and Belize (-1.6 m MSL), *A. palmata* is most abundant at a considerably deeper water depth in Florida (-2.9 m MSL) and Puerto Rico and the Virgin Islands (-3.8 m MSL).

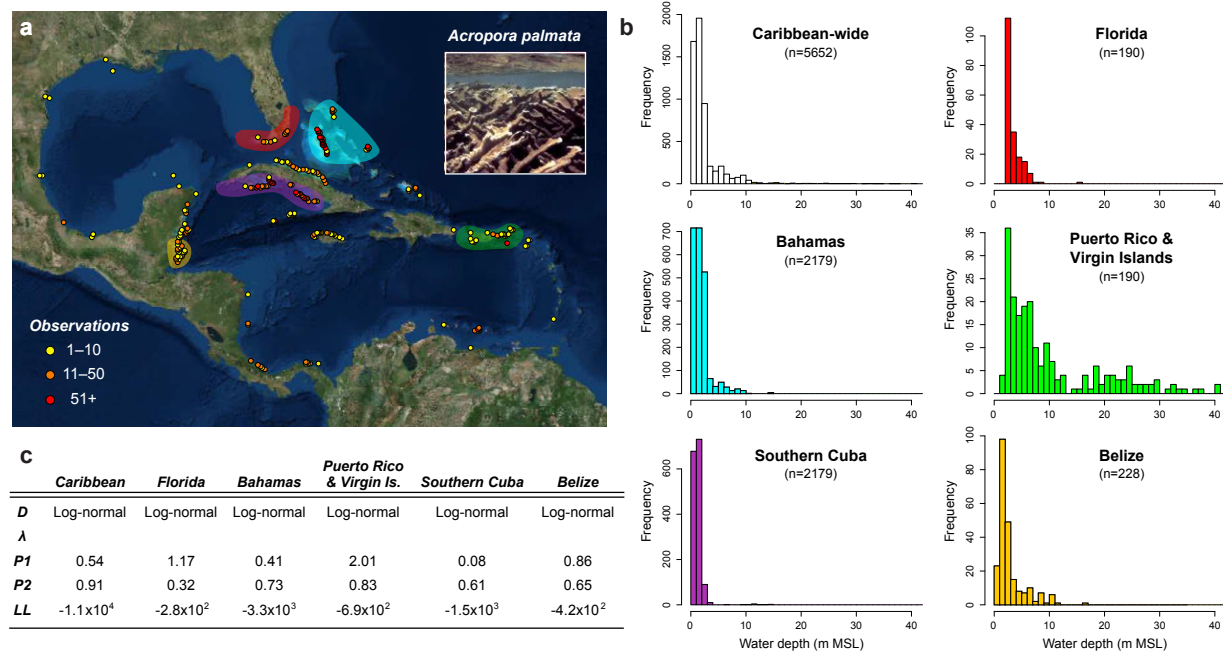


Figure B.2: Histograms (b) and fitted distribution (c) of *A. palmata* throughout the Caribbean and in five distinct sub-regions indicated by the colored shading on the map (a). The distribution of data of this species in the OBIS database is indicated by the colored points on the map.

B.1.2 Caribbean-wide coral depth distributions

The modern depth distributions of the Caribbean corals that we analyzed were generally best fit by log-normal probability distributions when considering only parametric distributions (Figure B.3). The only exception was the *Orbicella* spp. complex, whose depth distribution was best fit by a normal distribution. As expected, *A. palmata*, has the shallowest depth distribution, occurring in peak abundance at -0.8 m MSL, followed by *P. clivosa*, *P. strigosa*, *A. cervicornis*, and *P. astreoides*, which peak between -1.1 and -2.1 m MSL. In contrast, the majority of corals with massive morphologies are most abundant at intermediate depths (-4.9 to -10.0 m MSL).

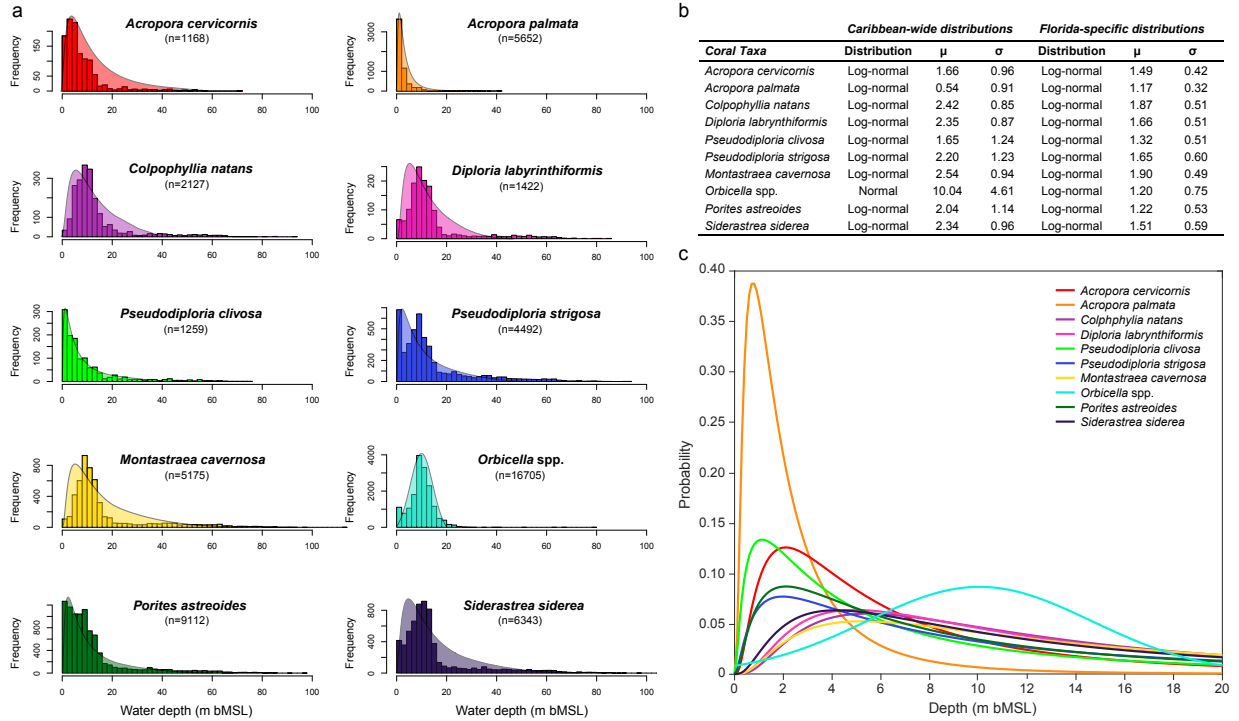


Figure B.3: Parametric depth distributions of the 9 coral taxa used in the statistical model: a) histograms of the Caribbean-wide modern occurrences of the taxa by depth with fitted distributions over-laid (note: frequencies are not on the same scales), b) table showing the Caribbean-wide and Florida-specific fitted distributions and parameters (μ and σ , which are the mean and standard deviation for normal distributions and the scale and shape parameters for log-normal distributions), and c) the probability density function of the best-fit parametric Caribbean-wide distributions for each taxon.

B.1.3 Florida-specific depth distributions

The modern depth distributions of the corals, based on the Florida-specific dataset, were all well-fit by log-normal distributions (Figure B.3b), when considering only parametric distributions. These fitted distributions are generally shallower than in the Caribbean-wide dataset. All of the coral taxa we analyzed, except for *M. cavernosa*, peaked at depths shallower than -5 m MSL. Interestingly, *A. palmata* is the only coral that has a deeper (but narrower) distribution in Florida than in the broader Caribbean.

B.2 Model implementation

B.2.1 Noisy-input Gaussian process (NIGP) method

Age uncertainties are incorporated using the NIGP method of McHutchon and Rasmussen (2011), which uses the first-order Taylor-series approximation (a linear expansion about each input point) to translate errors in

the independent variable (time) into equivalent errors in the dependent variable (RSL), such that temporal error is recast as sea-level error proportional to the squared gradient of the GP posterior mean (McHutchon and Rasmussen, 2011).

$$f(t_i) \approx f(\hat{t}_i) + \gamma_i^t \frac{\partial f(\hat{t}_i)}{\partial \hat{t}} \quad (\text{B.1})$$

where $f(t_i)$ is the sea-level process at time, t_i , γ is the temporal error, and $\partial f(\hat{t}_i)/\partial \hat{t}$ is the partial derivative of f with respect to \hat{t} . Age uncertainties are assumed to be normally distributed, such that $\gamma_i \sim \mathcal{N}(0, \tau_i^2)$:

$$\mathbf{z} = f(\mathbf{t} + \boldsymbol{\gamma}) + \boldsymbol{\delta}, \quad (\text{B.2})$$

where $\boldsymbol{\delta}$ is the normally distributed elevation measurement uncertainty in Section 3.2.1, such that $\delta_i \sim \mathcal{N}(0, \varepsilon_i^2)$ (from equation 3.6). The approximation of \mathbf{z} is:

$$\mathbf{z} \approx f(\hat{\mathbf{t}}) + \boldsymbol{\gamma} \frac{\partial f(\hat{\mathbf{t}})}{\partial \hat{\mathbf{t}}} + \boldsymbol{\delta} \quad (\text{B.3})$$

The predictive posterior distribution is a GP with mean, $\bar{\mathbf{f}}_*$, and variance $\mathbb{V}[\mathbf{f}_*]$:

$$\mathbb{E}[\mathbf{f}_* | \hat{\mathbf{t}}, \mathbf{z}, \mathbf{t}_*] = k(\mathbf{t}_*, \hat{\mathbf{t}}) [K(\hat{\mathbf{t}}, \hat{\mathbf{t}}) + \boldsymbol{\varepsilon}^2 I + \text{diag}\{\boldsymbol{\Gamma}_{\bar{\mathbf{f}}} \boldsymbol{\Sigma}_t \boldsymbol{\Gamma}_{\bar{\mathbf{f}}}^T\}]^{-1} \mathbf{z} \quad (\text{B.4})$$

$$\mathbb{V}[\mathbf{f}_* | \hat{\mathbf{t}}, \mathbf{z}, \mathbf{t}_*] = k(\mathbf{t}_*, \mathbf{t}_*) - k(\mathbf{t}_*, \hat{\mathbf{t}}) [K(\hat{\mathbf{t}}, \hat{\mathbf{t}}) + \boldsymbol{\sigma}_z^2 I + \text{diag}\{\boldsymbol{\Gamma}_{\bar{\mathbf{f}}} \boldsymbol{\Sigma}_t \boldsymbol{\Gamma}_{\bar{\mathbf{f}}}^T\}]^{-1} k(\hat{\mathbf{t}}, \mathbf{t}_*) \quad (\text{B.5})$$

where $\boldsymbol{\varepsilon}^2$ is the vector of all ε_i^2 , $\boldsymbol{\Sigma}_t$ is the temporal noise matrix, $\boldsymbol{\Gamma}$ is the matrix of derivatives, K is the original training covariance matrix, k is the covariance between test \mathbf{t}_* and training points, and $\boldsymbol{\Gamma}_{\bar{\mathbf{f}}} \boldsymbol{\Sigma}_t \boldsymbol{\Gamma}_{\bar{\mathbf{f}}}^T$ is the corrective variance term added to output noise, so that inputs (times) can be treated as deterministic. See McHutchon and Rasmussen (2011) for more details.

B.2.2 Markov Chain Monte Carlo (MCMC) sampling

The MCMC samples of \mathbf{z} and $\boldsymbol{\Theta}_s$, conditional on $\hat{\mathbf{y}}$ and $\boldsymbol{\Theta}_d$, are generated using a Metropolis-within-Gibbs algorithm based on the following derivation. Assuming an uninformative prior on $\boldsymbol{\Theta}_s$,

$$p(\boldsymbol{\Theta}_s, \mathbf{z} | \hat{\mathbf{y}}, \hat{\mathbf{t}}, \boldsymbol{\Theta}_d) \propto p(\hat{\mathbf{y}} | \mathbf{z}, \boldsymbol{\Theta}_d, \boldsymbol{\Theta}_s) \cdot p(\mathbf{z} | \hat{\mathbf{t}}, \boldsymbol{\Theta}_d, \boldsymbol{\Theta}_s). \quad (\text{B.6})$$

Since \hat{y}_i depends only on z_i and $\boldsymbol{\Theta}_d$ for all i , the first term on the right-hand side simplifies to $\prod_i p(\hat{y}_i | z_i, \boldsymbol{\Theta}_d)$. If we know the values of all z except z_i (denoted \mathbf{z}_{-i}), we can estimate the posterior probability of z_i ,

$p(z_i|z_{-i}, \hat{\mathbf{t}}, \Theta_s, \Theta_d)$ analytically from the NIGP predictive equations of McHutchon and Rasmussen (2011) (Section B.2.1), which incorporate temporal uncertainty. Therefore, samples of $p(\Theta_s, \mathbf{z}|\hat{\mathbf{y}}, \hat{\mathbf{t}}, \Theta_d)$ are created according to the likelihood of each randomly generated z'_i by calculating and multiplying $p(z'_i|z_{-i}, \hat{\mathbf{t}}, \Theta_s, \Theta_d)$ and $p(\hat{y}_i|z_i, \Theta_d)$ and accepting or rejecting proposed samples based on the ratio A :

$$A = \min \left(1, \frac{p(\hat{y}_i|z'_i, \Theta_d) \cdot p(z'_i|z_{-i}, \hat{\mathbf{t}}, \Theta_s, \Theta_d)}{p(\hat{y}_i|z_i, \Theta_d) \cdot p(z_i|z_{-i}, \hat{\mathbf{t}}, \Theta_s, \Theta_d)} \right) \quad (\text{B.7})$$

Proposed samples of Θ_s are equivalently accepted or rejected based on the ratio A' :

$$A' = \min \left(1, \frac{p(\theta'_i|\mathbf{z}, \theta_{-i})}{p(\theta_i|\mathbf{z}, \theta_{-i})} \right), \quad (\text{B.8})$$

where θ_i represents each hyperparameter in Θ_s .

The entire algorithm is summarized in the following four steps:

1. **Modern coral distribution fitting:** The indicative meanings each type of coral taxa are analyzed and fit to parametric distributions (Section 3.2.2). These distributions and their parameters Θ_d for each taxa are used as likelihoods in the sampling module (2).
2. **Sampling module:** This step generates samples of RSL (\mathbf{z}) and RSL process hyperparameters (Θ_s). Inputs comprise $\hat{\mathbf{y}}$, $\hat{\mathbf{t}}$, and $f(t)$ (GP prior distributions, see equations 3.13).
 - (a) Initialize \mathbf{z} , Θ_s (the vector of sea-level hyperparameters $\{\alpha_m, \beta_m, \alpha_w\}$), and all step sizes.
 - (b) Sequentially sample new z'_i , based on NIGP and likelihood, with acceptance probability A (Supplemental equation B.7) and each θ'_s with acceptance probability A' (Supplemental equation B.8).
 - (c) Every 80th iteration, reassign step size (proposals are randomly sampled from a normal distribution with standard deviation of the initialized or recalculated step size) to optimize acceptance ratio (Gelman et al., 2013) according to:
 - If accept ratio > 0.3 or accept count < 5, increase step size standard deviation.
 - If accept ratio < 0.2, decrease step size standard deviation.
3. **Estimate \mathbf{f} , conditional upon the paired samples of \mathbf{z} and Θ_s :** Combine samples of noisy RSL and RSL hyperparameters: $\mathbf{f}|\mathbf{z}, \hat{\mathbf{t}}, \Theta_s, \Theta_d$ from the NIGP predictive equations of McHutchon and Rasmussen (2011) (Section B.2.1).
4. **Draw samples & pool:** Generate estimates of final posterior distribution of RSL by drawing 10 random samples from each combined pair of \mathbf{z} and Θ_s . Pool all samples to generate an estimate of

$$p(f, \Theta_s, t | \hat{y}, \hat{t}, \Theta_d).$$

B.3 Results

All of the coral-only models are similar, except for the one based on the parametric Caribbean-wide data. The model uses a wide normal distribution to estimate the likelihood for *Orbicella* spp., which creates a highstand in the late Holocene, when other data are not present to anchor the RSL signal (Figure B.4).

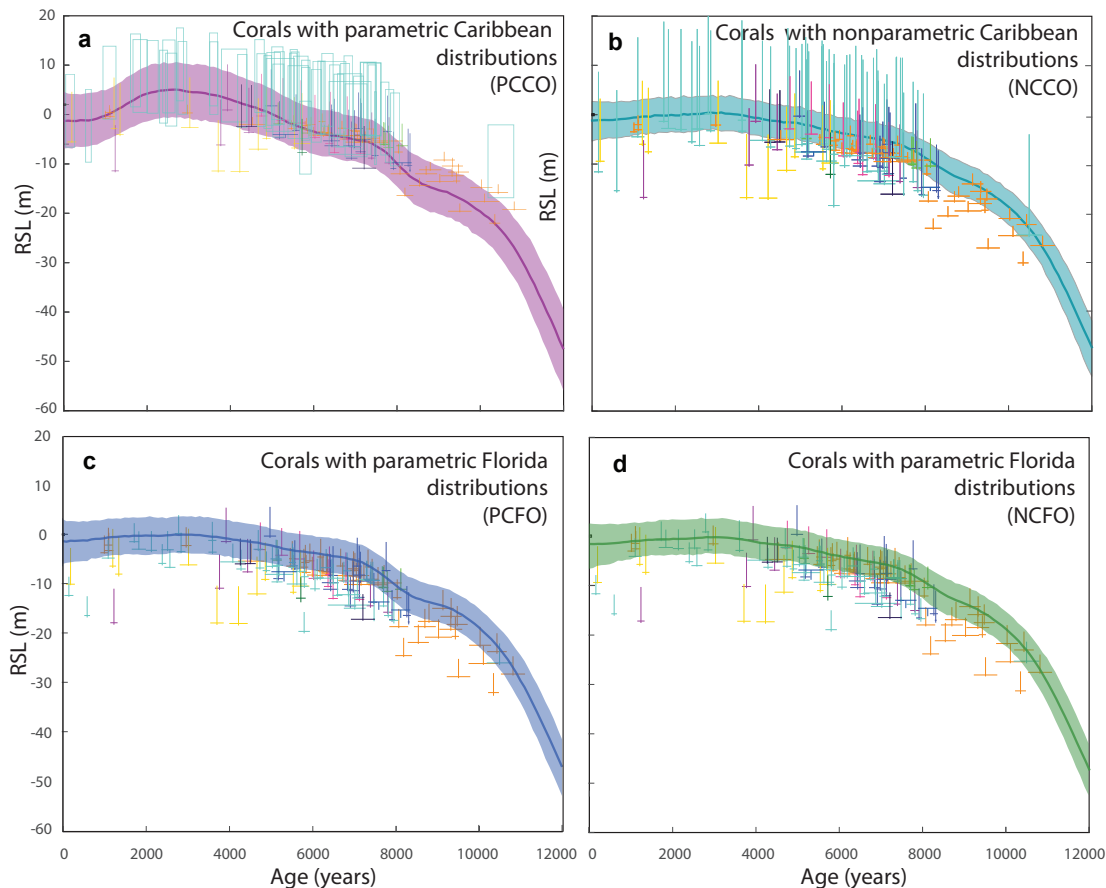


Figure B.4: Comparison between the four models that only use corals.

B.4 Simulation and synthetic analysis

B.4.1 Synthetic tests

To determine the data requirements necessary to detect RSL changes characteristic of interglacial and deglacial periods, we employ synthetic data tests to identify the quantity, type, precision, and temporal

distribution of data needed to accurately and precisely reconstruct these patterns. We construct two synthetic RSL time series to approximate the rates of RSL change observed during the best constrained and most recent interglacial and deglacial periods: the Holocene and the last deglaciation. The first synthetic RSL time series, “SL1” (Figure B.5a), uses a sine curve to simulate rates of change representative of the Holocene epoch, ranging from ~ -10 to $\sim +10$ m/ky. The second synthetic RSL time series, “SL2” (Figure B.5a), contains abrupt changes, simulating meltwater pulses, which occurred during deglaciation with rates of change up to ~ 40 m/ky (e.g., Abdul et al., 2016; Rohling et al., 2008; Lambeck et al., 2014). Both time series extend over 12000 year time periods.

To evaluate model performance, we apply it to a total of 81 synthetic datasets for each of the two RSL time series. These 81 datasets include every combination of the following 4 factors : 1) the number of data points (25, 50, or 100), 2) the percentage of data with log-normally distributed uncertainties (25%, 50%, or 75%; the remaining data are normally distributed), 3) the uncertainty of the normally distributed data (σ of 1 m, 5 m, or 10 m), and 4) the uncertainty of log-normally distributed data (scale and shape parameters of LN 1: (0.7,1.0), LN 2: (1.7, 1.1), or LN 3: (2.5, 1.2); Figure B.5b). The normal and log-normal synthetic data distribution parameters are based on the uncertainties observed in, and the fitted distributions of, the modern coral data. Percentiles of the synthetic data distributions are presented in Figure B.5, and the factors for each individual test and description of the synthetic data generation are detailed in Section B.4.1.

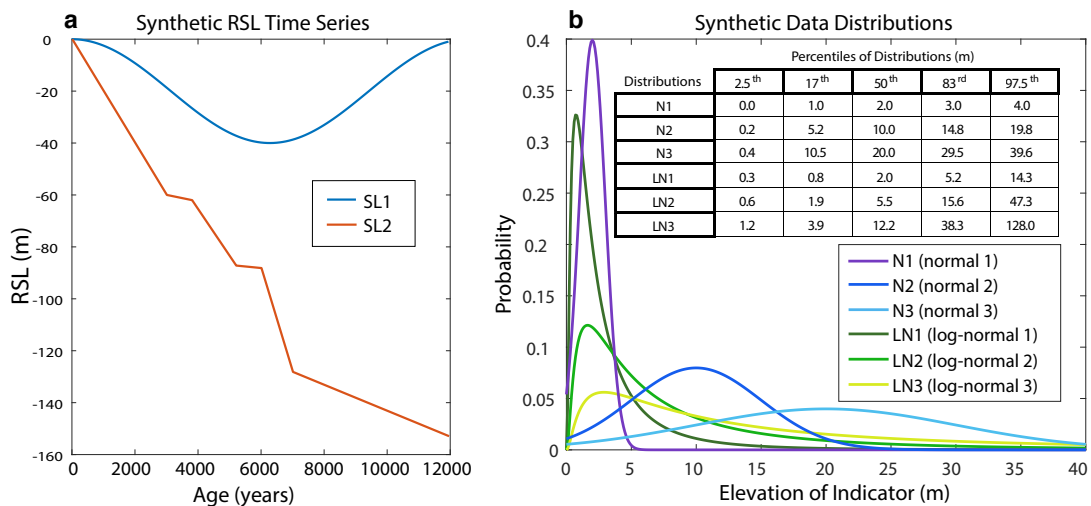


Figure B.5: (a) Synthetic RSL time series SL1 and SL2, which simulate rates characteristic of the Holocene and the last deglaciation, respectively; (b) probability density functions of log-normal and normal synthetic data distributions, which incorporate different levels of data precision in the synthetic tests.

We apply the statistical framework to model sea level from the synthetic data, taking 20,000 MCMC samples for each of the 81 tests. We run each set of tests with 5 starting seeds (random numbers for

replication) in order to maximize the randomness and increase sample size for accurate statistical evaluation of the models. Each model run produces a distribution of predicted RSL and its rates of change at 100-year intervals in addition to the following summary statistics, which describe the precision and accuracy of the modeled sea-level curve relative to ‘true’ (synthetic) sea level:

RSL Precision [=mean(CI width for RSL)]: The posterior uncertainty of predicted RSL averaged over 100-yr predictions for 67% and 95% CIs.

Mean Absolute Error [=mean(|median(f)-true RSL|)]: The average absolute error in predicted sea level averaged over 100-yr predictions.

RSL Bias [=mean(median(f)-true RSL)]: The mean difference between the predicted and true sea level. If the average bias is positive (negative), the model is predicting RSLs that are too high (low).

Rate Precision [=mean(CI width for rate)]: The posterior uncertainty (67% and 95% CIs) in predicted rate of change, which is averaged over 500-yr intervals for predictions every 100 years.

Rate Accuracy [=mean(|median rate-true rate|)]: The average absolute error in the predicted rate.

Maximum Rate Distribution [=distribution of max(rate)]: The median and 95% CI of max(rate) over all samples (where rates are averaged over 500-yr intervals and calculated every 100 years). This metric can be compared with the maximum ‘true’ rate of change of the synthetic sea-level curve.

RSL Coverage Ratio [= $\frac{\text{count of true RSL within CI}}{\text{count of total}}$]: Quantifies the accuracy of the 67% and 95% credible intervals. If coverage for a 95% CI is greater (less) than 95%, then the CIs are too wide (narrow).

Rate of Change Coverage Ratio [= $\frac{\text{count of true rate within CI}}{\text{count of total}}$]: Quantifies the accuracy of the rate credible interval, as described for the RSL Coverage Ratio.

B.4.2 Synthetic data generation

For each synthetic test, we generate random sea-level index points based on the parameters defined by the factors of that test. The ages are defined based on

$$\hat{t}_i = t_i + \gamma_i \tag{B.9}$$

where t is the true age drawn from a uniform distribution between 0 and 12 ka ($t_i \sim U(0, 12000)$ BP), γ is age error, such that $\gamma_i \sim \mathcal{N}(0, \tau_i^2)$, and τ is drawn from a normal distribution with a mean of 140 years, and a standard deviation of 75 years, but must be at least 11 years ($\tau_i \sim \max[11, \mathcal{N}(140, 75^2)]$ years), and \hat{t}_i is

the noisy age. This choice was informed by the age uncertainties from the south Florida dataset analyzed in this study (Section 3.2.3).

For each true age, the true RSL is z_i , and the index point’s observed elevation \hat{y} is shifted according to the assigned relationship (normal or log-normal) by a random draw from that distribution as well as a random draw from $\mathcal{N}(0,1)$ to account for measurement error.

B.4.3 Synthetic test results

The synthetic analyses test the performance of the new model framework under distinct sea-level scenarios with different combinations of quantity and quality of data. The models that perform well are those that accurately and precisely detect true RSL and rates of change (e.g., Figure B.6a,d for SL1 and Figure B.6g,h,j,k for SL2), whereas poorly performing models have low accuracy and/or precision (e.g., Figure B.6b,c,e,f for SL1 and Figure B.6i,l for SL2). Details of the effects of each data factor and results of each test are in Section B.4.1. We summarize the overall trends below.

Consistent with statistical expectations, higher quantity and quality (precision) of data leads to higher accuracy (lower error) in posterior predictions of RSL with similar results in both synthetic sea-level scenarios, SL1 and SL2. Comparing the Mean Absolute Error of each test to its “precision factor,” defined as a ranking (which is highest for the most precise data) of the combined precisions of the two data distributions used as input (Table B.1), and its sample size reveals a strong relationship (Figure B.7). In both sea-level scenarios, the average Mean Absolute Error decreases monotonically as the precision factor increases for a sample size of 100 data points. In contrast, with only 25 data points in both sea-level scenarios, the average Mean Absolute Error is lower for precision factor 8 (N1,LN3) than 7 (N2,LN1) and for precision factor 5 (N2,LN3) than 4 (N2,LN1), suggesting that the low precision data has little value when sample size is low. Overall, this visualization demonstrates that increasing precision of data has a similar effect to increasing sample size.

B.5 Evaluation of proxy and model performance using synthetic data

The synthetic analyses demonstrate that the most important factors determining the accuracy and precision of the models are the quantity and quality of the data, but the required data criteria (minimum sample size and precision) vary for different underlying sea-level scenarios.

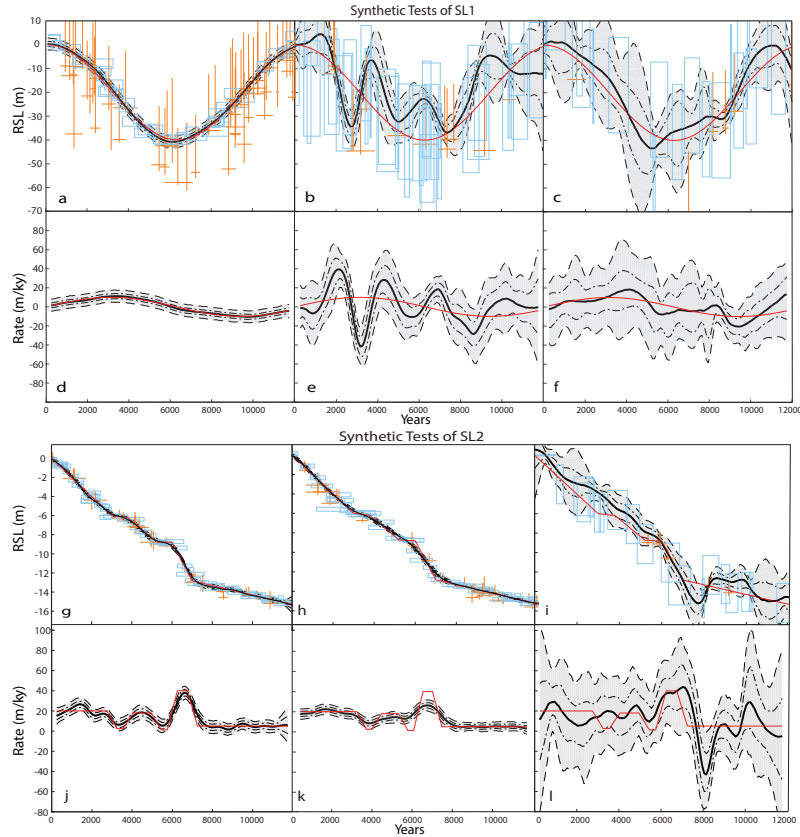


Figure B.6: Comparison between RSL predictions (SL1: a–c and SL2: g–i) and rate predictions (SL1: d–f and SL2: j–l) of tests with different factors. Median (solid black line) with 67% and 95% CIs (dashed lines) are compared with true RSL/rate (red lines). For SL1: (a,d) test 22, $n=100$, 50% log-normal, data distributions N1 and LN2; (b,e) test 72, $n=50$, 25% log-normal, data distributions N3 and LN2; (c,f) test 33, $n=25$, 25% log-normal, data distributions N3 and LN2. For SL2: (g,j) test 6, $n=100$, 25% log-normal, data distributions N1 and LN1; (h,k) test 6, $n=100$, 25% log-normal, data distributions N1 and LN1 (i,l) and test 15 (25 data points, 25% of which are log-normal, using distributions N3 and LN1

B.6 Results and discussion of synthetic analyses

The factors for each synthetic test are given in the following file:

Synthetic_Test_Factors.xlsx

The average results of the analyses are in Tables B.2 & B.3, and the results of the individual synthetic tests are given in the following files:

Synth_Results_1.xlsx

Synth_Results_2.xlsx

Synth_SL1_SL2_Output.xlsx

Table B.1: Precision Factor: a metric that combines the precisions of the two synthetic data distributions used as input for each synthetic test.

Precision factor	Normal data distributions	Log-normal data distributions
10	N1	LN1
9	N1	LN2
8	N1	LN3
7	N2	LN1
6	N2	LN2
5	N2	LN3
4	N3	LN1
3	N3	LN2
2	N3	LN3

B.6.1 Sample size:

As expected, increasing the number of data points in a model increases the accuracy and precision of the predictions (Tables B.2 & B.3). Doubling the number of data points increases RSL Precision (by 13% & 43% for SL1, 32% & 49% for SL2) and RSL Accuracy (by 21% & 28% for SL1, 29% & 36% for SL2) in all cases, but less, on average, for synthetic time series SL1, where RSL change is more gradual, than the more abruptly varying SL2. The impact of doubling the sample size from 25 to 50 is also more moderate than doubling it from 50 to 100. Rate Precision is less sensitive to changing sample size, with negligible increases ($\leq 3\%$) in all cases except when doubling from 50 to 100 points for SL1, which produces $\sim 20\%$ increase in Rate Precision. The RSL Coverage Ratio is not particularly sensitive to changes in sample size and is generally too high for SL1, especially for the 67% CI ($\sim 96\%$ for the 95% CI and $\sim 77\%$ for the 67% CI) and too low for SL2, especially for the 95% CI ($\leq 88\%$ for the 95% CI and $\sim 63\%$ for the 67% CI). The RSL Bias is significantly higher with 25 data points for SL2 than in any other scenario, but RSL Bias, which is always positive, decreases with increasing sample size and is negligible in predictions of SL1 with 100 data points. The Maximum Rate Distribution for SL1 is centered consistently above the true maximum (10 m/ky) and shifts upward with increased sample size. For SL2, the trend of increasing Maximum Rate Distribution with increasing sample size is the same, but more data allow the model to more accurately approach the true maximum rate of 40 m/ky. The Rate Coverage Ratios are significantly higher than expected (99.2% and 93.7% on average 95% and 67% CIs, respectively) for SL1, but do not change significantly with the amount of data. For SL2, the Rate Coverage Ratio is too low for the 95% CIs, but is only marginally lower than expected for the 67% CIs. The Rate Coverage Ratios do not vary consistently with changing sample size. A further discussion of coverage ratios is presented in Appendix section B.6.5.

Table B.2: Test results for synthetic time series SL1, with notable values highlighted in *bold italics*.

	RSL Prec. (width m)		Mean Abs. Err. (m)	RSL Bias (m)	RSL Cov. Ratio	
	95% CI	67% CI	Abs. Error	Ave. Error	95% CI	67% CI
N = sample size						
25	14.3	6.8	2.5	0.5	96.2%	77.0%
50	12.6	6.0	2.0	0.3	96.3%	77.4%
100	8.9	4.2	1.6	0.2	96.6%	78.4%
% Log-norm.						
25	12.6	6.0	2.1	0.5	96.0%	77.1%
50	12.7	6.0	2.3	0.2	96.0%	77.1%
75	10.5	4.9	1.7	0.2	97.1%	78.7%
Normal sd						
1	5.9	2.8	0.8	0.0	98.7%	85.0%
5	9.2	4.3	1.5	0.1	97.5%	76.8%
10	20.7	9.8	3.8	0.9	92.9%	71.0%
Log-norm. dist.						
LN1 (0.7, 1.0)	7.6	3.6	1.1	0.2	97.7%	82.9%
LN2 (1.7, 1.1)	11.3	5.4	1.9	0.4	96.3%	76.2%
LN3 (2.5, 1.2)	16.9	8.0	3.0	0.3	95.1%	73.7%

	Rate Prec. (width)		Rate Acc.	MRD (m/ky)			Rate Cov. Ratio	
	95% CI	67% CI	Abs. Error	Median	83%ile	17%ile	95% CI	67% CI
N = sample size								
25	28.4	13.0	3.0	14.0	20.6	7.8	99.4%	95.2%
50	30.0	14.0	3.2	16.4	23.9	10.1	99.3%	94.0%
100	23.8	10.9	2.9	17.6	24.7	11.7	98.8%	92.0%
% Log-norm.								
25	29.0	13.5	3.0	16.2	24.2	9.8	99.3%	93.7%
50	29.3	13.6	3.1	18.0	25.2	11.3	98.7%	92.3%
75	23.9	10.9	3.0	13.8	19.7	8.4	99.4%	95.3%
Normal sd								
1	12.3	5.8	2.9	10.9	13.8	8.1	99.8%	97.5%
5	20.2	9.2	3.0	11.2	15.8	6.5	100.0%	97.5%
10	49.7	23.0	3.2	25.9	39.6	15.0	97.7%	86.2%
Log-norm. dist.								
LN1 (0.7, 1.0)	16.7	7.7	2.8	11.6	15.5	7.9	99.6%	96.1%
LN2 (1.7, 1.1)	25.8	11.9	2.8	14.1	21.0	8.5	99.5%	94.4%
LN3 (2.5, 1.2)	39.8	18.4	3.5	22.3	32.6	13.2	98.4%	90.7%

Table B.3: Test results for synthetic time series SL2, with notable values highlighted *bold italics*.

	RSL Prec. (width m)		RSL Acc. (m)	RSL Bias (m)	RSL Cov. Ratio	
	95% CI	67% CI	Abs. Errr	Ave. Err.	95% CI	67% CI
N = sample size						
25	18.8	8.9	4.1	1.6	86.1%	64.7%
50	14.2	6.8	3.2	0.6	87.9%	63.1%
100	9.6	4.6	2.3	0.4	85.5%	61.0%
% Log-norm.						
25	13.9	6.6	3.1	0.9	86.1%	62.5%
50	15.2	7.3	3.5	0.7	86.8%	64.0%
75	13.5	6.4	3.1	1.0	86.6%	62.3%
Normal sd						
1	8.4	4.1	2.0	0.4	87.8%	67.3%
5	10.9	5.2	2.8	0.6	84.1%	58.1%
10	23.3	11.1	4.9	1.6	87.6%	63.4%
Log-norm. dist.						
LN1 (0.7, 1.0)	10.1	4.8	2.4	0.9	86.6%	64.0%
LN2 (1.7, 1.1)	13.0	6.2	3.1	1.0	85.2%	61.2%
LN3 (2.5, 1.2)	19.5	9.3	4.1	0.7	87.7%	63.7%

	Rate Prec. (width)		Rate Acc.	MRD (m/ky)			Rate Cov. Ratio	
	95% CI	67% CI	Abs. Err.	Med.	83%ile	17%ile	95% CI	67% CI
N = sample size								
25	37.8	17.4	6.6	28.5	37.6	20.7	88.5%	68.5%
50	34.1	16.0	6.2	33.7	42.0	25.9	89.8%	69.8%
100	25.5	11.9	4.4	33.6	40.1	27.8	85.9%	64.3%
% Log-norm.								
25	32.2	14.8	5.8	30.9	38.9	23.9	88.9%	69.0%
50	35.0	16.4	6.7	34.1	42.4	26.5	88.6%	67.5%
75	30.2	14.1	4.9	30.9	38.5	24.0	86.7%	66.2%
Normal sd								
1	18.4	8.7	4.1	28.7	33.2	24.4	86.0%	67.5%
5	23.5	10.7	5.1	26.2	31.8	20.8	85.3%	63.3%
10	55.4	25.8	7.0	41.0	54.8	29.2	92.9%	71.8%
Log-norm. dist.								
LN1 (0.7, 1.0)	22.4	10.4	4.9	28.9	34.3	23.7	85.6%	65.1%
LN2 (1.7, 1.1)	29.1	13.5	5.8	30.5	37.5	24.0	87.2%	66.3%
LN3 (2.5, 1.2)	45.9	21.4	5.3	36.5	48.0	26.7	91.4%	71.3%

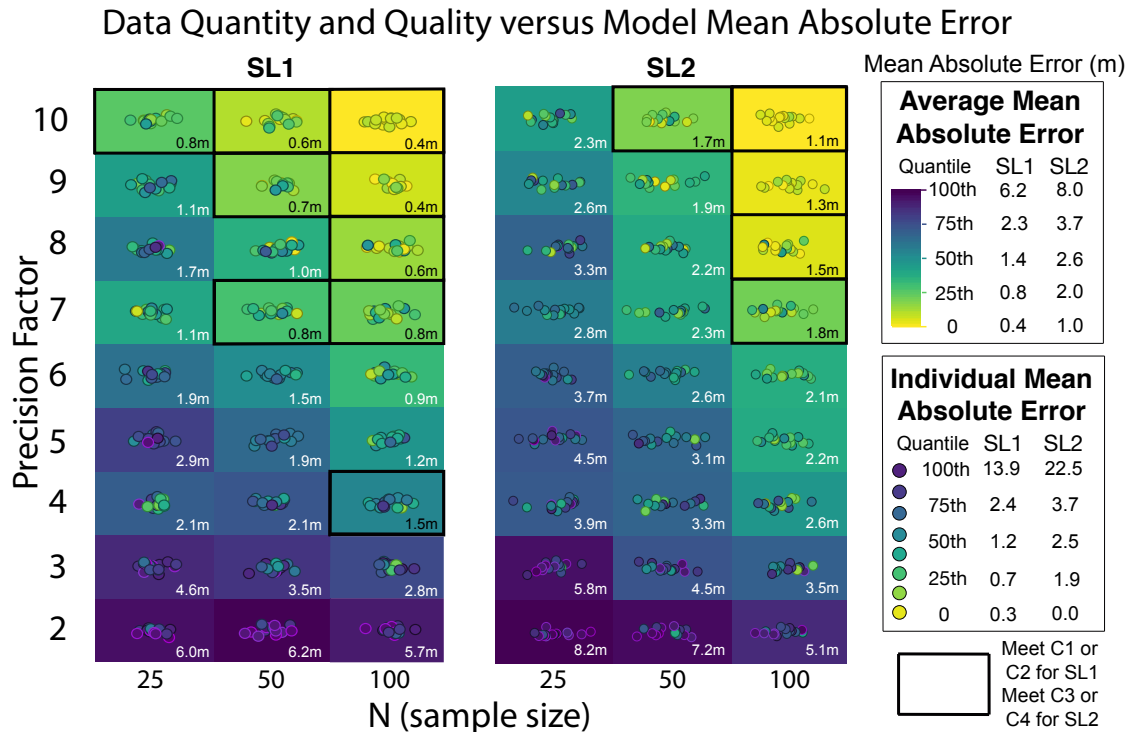


Figure B.7: Sample size and precision of input data versus test model's Mean Absolute Error: The precision factor has a notable effect on the accuracy of the resulting model. A similar pattern can be seen in the the results of the SL1 and SL2 models, but the scale of the accuracy measures is different. The Average Mean Absolute Error for the group of tests with the same precision factor and sample size is shown by the color in each box, and is also labeled in the lower right corner. Each test is represented by a single point, the color of which depicts its Individual Mean Absolute Error, and each test within a box has the same sample size and precision factor.

B.6.2 Percent Log-normal:

Increasing the number of log-normally distributed data points, relative to normally distributed data, has more variable impacts on precision and accuracy, with an increasing proportion of log-normal data increasing precision and accuracy in some cases, but having no impacts in others. For SL1, increasing the percentage of log-normal data from 25% to 50% results in no change in accuracy or precision, whereas increasing the percentage of log-normally distributed data points from 50% to 75% increases RSL Accuracy (by ~18%) and RSL Precision (by ~17%); RSL Bias only decreases when the percentage of log-normal data increases from 25% to 50%. For SL2, RSL Precision and RSL Accuracy both increase with the 25% to 50% increase in log-normal data and then decrease by similar amounts for the subsequent increase from 50% to 75% log-normal data. Conversely, the Maximum Rate Distribution, for SL2, shifts upwards and then back downwards with increases in the relative number of log-normal data points, suggesting that lower precision and accuracy may allow for higher maximum rates predicted by the models. The same trend is observed for SL1 and the

decrease in Maximum Rate Distribution when the percentage of log-normal data is increased from 50% to 75% results in a maximum predicted rate that is closer to the true maximum of 10 m/ky and is accompanied by an increase in Rate Precision. For SL2, increasing the percent log-normal does not have a significant impact (less than 2% increase or decrease) on the Rate Precision nor on the Rate Coverage Ratio.

B.6.3 Normal uncertainty:

Increasing the uncertainty (decreasing the precision) of the normally distributed data, by increasing the standard deviations on their distributions, has significant effects on precision and accuracy, as expected. Increasing the standard deviation from 1 to 5 m decreases RSL Precision by over 50% for SL1 and $\sim 28\%$ for SL2. Increasing normal uncertainty again from 5 m to 10 m decreases RSL Precision by over 110% for both SL1 and SL2. Increasing uncertainty from 1 to 5 m decreases RSL Accuracy by 79% for SL1 and 41% for SL2. Increasing uncertainty from 5 to 10 m decreases RSL Accuracy by 164% for SL1 and 75% for SL2. As uncertainty increases, RSL Bias increases significantly, with a bias towards higher predictions of RSL, likely as a result of the zero-mean prior. Rate Precision also decreases for SL1 (by $\sim 60\%$ for 1 to 5 m & $\sim 150\%$ for 5 to 10 m), and both Rate Precision and Rate Accuracy decrease for SL2 (Rate Precision by $\sim 30\%$ & $\sim 115\%$, Rate Accuracy by $\sim 40\%$ & $\sim 75\%$). The Maximum Rate Distribution shift upwards for SL1 and SL2 precision decreases. Whereas this results in predicted maximum rates for SL1 that are significantly higher than the true maximum rate, it increases the probability of the model predicting the true maximum rate of 40 m/ky for SL2, despite the accompanying decrease to Rate Precision. The RSL and Rate Coverage Ratios generally decrease for SL1 as normal uncertainties in the data increase. Conversely, coverage ratios decrease when increasing normal uncertainty from 1 to 5 m and then increase when increasing from 5–10 m for SL2. Although the 95% CI coverage ratios are generally higher than expected for SL1, they are generally slightly smaller than expected for the 95% CIs for SL2.

B.6.4 Log-normal uncertainty:

Increasing the uncertainty (or decreasing precision) in the log-normally distributed data, by changing the parameters on the distribution (Section B.4.1; Figure B.5), also has significant effects on precision and accuracy of the models. Decreasing the precision of the data for SL1 decreases RSL Precision by about 49% and Rate Precision by about 54% for both distribution changes, while decreasing RSL Accuracy by 70% (from LN 1 to LN 2) and 57% (from LN2 to LN3). The same changes in uncertainty for SL2 decrease RSL Precision by $\sim 28\%$ and 50%, respectively, and decrease RSL Accuracy by $\sim 28\%$ and 33%, respectively. The RSL Bias increases and then decreases for both synthetic time series with the successive increases in the uncertainties of the log-normal distributions. The RSL Rate Precision decreases by $\sim 30\%$ when changing

from LN1 to LN2, and $\sim 58\%$ when changing from LN2 to LN3 for both SL1 and SL2. The Maximum Rate Distribution shifts upwards for both synthetic time series and both decreases in log-normal data precision, with the central tendency of the distribution becoming larger than the true maximum rate for SL1, but closer to the true maximum rate for SL2. The RSL and Rate Coverage Ratios decrease when increasing uncertainty in the log-normal data, but always stay above their expected 95% and 67% for SL1, which indicates that both RSL and Rate CIs should be narrower than their predictions in all models. The RSL Coverage Ratios for SL2 do not change significantly, whereas the Rate Coverage Ratios increase when the precision of the data decrease indicating that the CIs for rate should be wider for the more precise log-normal data.

B.6.5 Evaluating the results of synthetic coverage ratios

Table B.4: Results of synthetic tests with 25 data points and most precise data versus all other tests

	RSL Prec. (width m)		RSL Acc. (m)	RSL Bias (m)		RSL Cov. Ratio	
	95% CI	67% CI	Abs. Error	Ave. Error	95% CI	67% CI	
N=25, N1, LN1	6.2	3	0.8	0	99.6%	86.2%	
All other tests	12.2	5.8	2.1	-0.3	96.3%	77.3%	

	Rate Prec. (width m/ky)		MRD (m/ky)			Rate Cov. Ratio	
	95% CI	67% CI	Median	83%ile	17%ile	95% CI	67% CI
N=25, N1, LN1	11.1	5.3	10.3	13	7.7	100.0%	98.0%
All other tests	28	12.9	16.2	23.4	9.9	99.1%	93.6%

Many of the models of synthetic time series SL1 overcover their credible intervals ($\sim 94\%$ & $\sim 97\%$ for 73%CI and 77%CI, respectively), in the sense that their coverage ratios are greater than the CI percentages that they predict. Although some tests produce accurate coverage ratios ($\sim 15\%$ are within 2–3% of the correct coverage), more than half of the tests we performed generated 95% CIs that included the true RSL and the true rate 100% of the time (by definition, this should only occur 95% of the time). For example, some models have inflated coverage ratios despite, or possibly due to, lacking precision (e.g., Figure B.6c,f). One possible explanation for this is that the model is designed (with hyperparameter ratios between amplitude and temporal scale) to detect more rapid changes in rate than SL1 exhibits. We see in the analysis of SL2 that this over-coverage disappears.

Many of the predicted CIs for both RSL and rate of change for SL2 are too narrow, such that the coverage ratios average 87% to 89% instead of the expected 95% coverage ($\sim 83\%$ & $\sim 60\%$ undercover, for 95% and 67% CI, respectively). The tests of SL2 that produce coverage ratios closest to 95% tend to be those incorporating data with higher precision (e.g., Figure B.6g,j) whereas those that do not meet the expected coverage tend to have hyperparameter combinations that are distinct from those models that do meet the expected coverage.

In particular, the models that do not have sufficient coverage, on average, have lower amplitude to temporal-scale hyperparameter ratios (ATHR), possibly due to unrealistic hyperparameter combinations. Higher frequency variability can be picked up either with a short temporal scale, or a long temporal scale with large amplitude (thus rendering the higher frequency variability a relative small proportion of the total). These ATHRs could be the result of a combination of factors, including poor temporal coverage of the data, which allows a gap during more extreme rates of change or when rates accelerate or decelerate. A predicted curve could be too smooth (resulting from low ATHR, e.g., Figure B.6h,l), where it is unable to detect abrupt changes in true RSL or too bumpy (resulting from high ATHR), where the model predicts changes in RSL that are not present in the underlying process. Another possible explanation for the disparity between expected and true coverage is a combination of high precision but poor temporal coverage in the data, which results in the smaller CIs that are unable to capture the underlying curve.

B.6.6 Case study data

This section provides a detailed description of samples used in the Holocene case study from south Florida, how they were analyzed, and how the uncertainties of those data were treated. We also provide a supplementary figure that shows the estimated rates of change from each iteration of the model.

OBIS data can be found in the files:

Florida_distribution_data.xlsx

Caribbean-wide_distribution_data.xlsx

Parametric distribution fitting results and data for each taxon can be found in the following files:

Regional_Pseudodiploria_strigosa_distribution_data.xlsx

Regional_Orbicella_spp_distribution_data.xlsx

Regional_Acropora_palmata_distribution_data.xlsx

Depth_distribution_analysis.xlsx

The coral and sedimentary archive data used for the case study can be found in the following file:

Coral_and_sedimentary.xlsx

Corals

Coral data are derived from published records of Holocene drill cores, surface grab samples, and sub-merged trench exposures sampled from southeast Florida, the Florida Keys, and Dry Tortugas (Shinn

et al., 1977; Shinn, 1980; Robbin, 1984; Shinn et al., 1981; Lighty et al., 1982; Mallinson et al., 2003; Lidz et al., 2003; Toscano and Macintyre, 2003; Reich et al., 2006; Banks et al., 2007; Reich et al., 2009; Brock et al., 2010; Stathakopoulos and Riegl, 2014; Toth et al., 2015, 2017). Whenever possible, published data on coral elevations are cross-referenced against physical samples using the core archive at the U.S. Geological Survey Coastal and Marine Science Center, in St. Petersburg, Florida (Reich et al., 2012; <https://olga.er.usgs.gov/coreviewer/>). The modern depth distributions of the coral are used to model their relationship to sea level. Three unidentified coral taxa and one sample from *Stephanocoenia intercepta* are interpreted to be marine limiting because their modern depth distributions are unknown.

Sedimentary records

Compilation and interpretation of sedimentary data was previously described in Khan et al. (2017). The 60 sedimentary records include 14 samples from estuarine or bay sediments, which place a lower bound on the past position of sea level (i.e., marine-limiting points) and 16 samples from freshwater peats, muds and soilstone crusts, which place an upper bound of the past position of sea level (i.e., terrestrial-limiting points). The 30 mangrove peats are assumed to form within a normal distribution $\mathcal{N}(\mu, \sigma^2)$ between MTL (mean tide level) and HAT (highest astronomical tide) (see Section 3.2 for details on indicative meaning). RWL and IR are directly related to the tides, where μ ranges from 0.29 m to 0.42 m, and σ ranges from 0.15 m to 0.21 m, in our database.

Dating

The majority of Holocene coral and sedimentary records from south Florida are dated using radiocarbon methodologies. Radiocarbon ages are measured by either accelerator mass spectrometry (AMS) or bulk radiometric dating by gas proportional counting or liquid scintillation counting measurements. Most samples using bulk radiometric dating were analyzed prior to the 1970s, before correction of ^{14}C ages for isotopic fractionation became routine procedure (Stuiver and Polach, 1977; Törnqvist et al., 2015). Isotopic fractionation of $\delta^{13}\text{C}$ values is accounted for using normally distributed uncertainty with 2σ of 4‰ (mangrove/freshwater plant tissue or peat: $-23 > \delta^{13}\text{C} > -31$ ‰; Vane et al. (2013); marine carbonates: $4 > \delta^{13}\text{C} > -4$ ‰; Stuiver and Polach, 1977; Polach, 1976), which equates to ~ 64 ^{14}C yr. We corrected for this effect by normalizing for $\delta^{13}\text{C}$ using the ‘dcorr’ spreadsheet of the CALIB radiocarbon calibration program (CALIB, 2017). Additionally, bulk sediment or peat samples from the Florida dataset may have incorporated contaminating sources of older carbon from dissolved CO_2 or HCO_3^- derived from radiocarbon-dead limestone or transported marine organic matter, or younger carbon from contemporary mangrove rootlets penetrating older sequences beneath the sediment surface. Following analysis by Hu (2010) of ^{14}C ages from bulk peat and

plant macrofossils, a ± 100 ^{14}C yr uncertainty is applied to bulk sedimentary samples to account for sample contamination (Törnqvist et al., 2015). The total ^{14}C uncertainty of these samples is calculated as the quadratic sum of analytical (measurement), bulk, and isotopic fractionation uncertainties (Törnqvist et al., 2015), and conventional ages (including total ^{14}C uncertainty) are calibrated using IntCal13. Radiocarbon ages from marine environments are calibrated using the global marine calibration curve (Reimer et al., 2013) and are corrected for local variations in marine reservoir age by using the time-varying estimates of the local reservoir correction (ΔR) for the marine environments of south Florida modeled by Toth et al. (2017). Ages are presented as thousands of calibrated years before present (ka), where “present” is 1950 CE (Stuiver and Polach, 1977).

Ages of two Holocene corals from south Florida are determined with U-series dating by multiple collector-inductively coupled plasma-mass spectrometry (MC-ICP-MS). The U-series ages and 2σ uncertainties are recalculated using the most recent decay constants (Cheng et al. (2013) for ^{230}Th and ^{234}U and by Jaffey et al. (1971) for ^{238}U). Both U-series ages pass the screening criteria suggested by the IntCal Working Group (Reimer et al., 2009).

Measurement uncertainties

Estimation of measurement uncertainties to determine sample elevation follow Hijma et al. (2015) and Khan et al. (2017) and include uncertainties associated with determining sample depth in a core (e.g., sampling, core shortening, non-vertical drilling uncertainties) and measuring the absolute elevation of core boreholes (e.g., tidal, water depth, leveling, and differential GPS (dGPS) uncertainties). For coral archives from drill cores, sampling uncertainties within the core are based on the estimated proximity of the sample to a measured breakpoint (i.e., a boundary between successive core barrels) in the cores, which by convention is given in feet. A 2σ sampling uncertainty of 0.5 feet (0.15 m) is assigned if the sample was taken within 0.5 feet of the top of a core, and a 2σ sampling uncertainty of 1 foot (0.30 m) is assigned if the sample was taken within 0.5 feet of a measured breakpoint. In all other cases, a 2σ sampling uncertainty of 2 feet (0.61 m) is assigned, which is roughly the maximum distance a sample could move within a standard 5-foot core section, given typical recovery. Elevations of a number of the Holocene coral records are measured precisely *in situ* using differential GPS or bathymetric surveys. In these cases, the instrumental uncertainties are used for estimating water-depth uncertainties. For Holocene coral records where reliable water depths are measured using underwater depth gauges (in feet), we assign water-depth uncertainties of 1 foot (0.30 m; i.e., the precision of the depth gauges) and correct the depths to MSL wherever possible. In cases where water depth measurement was unreliable or when there was disagreement among data sources (i.e., published manuscripts, unpublished field journals, notes on core boxes), an error of 2 feet (0.61 m) is assigned.

B.6.7 Discussion of biases

There are a number of factors that may alter the elevation or distribution of sedimentary proxies and cause apparent changes in RSL. For example, sedimentary proxies are susceptible to the effects of sediment autocompaction, which causes the downward displacement of a dated sedimentary record from the elevation at which it initially formed and results in a lower apparent position of RSL (Allen, 2000; Shennan et al., 2000; Edwards and Horton, 2006; van Asselen et al., 2009; Horton and Shennan, 2009; Brain et al., 2015). Previous studies from mangroves and temperate wetlands estimate that over Holocene timescales compaction may reduce the thickness of sedimentary sequences by 13–55% (Bloom, 1964; Kaye and Barghoorn, 1964; Stout and Spackman, 1989; Haslett et al., 1998; Bird et al., 2004; Törnqvist et al., 2008; Hijma et al., 2015), although there are approaches to minimize or correct for this effect by considering the stratigraphic position of a sample in a sedimentary column (e.g., Jelgersma, 1961; Shennan and Horton, 2002; Törnqvist et al., 2004; Horton et al., 2013; Khan et al., 2017) or using geotechnical approaches (using physical properties of sediments to assess or correct for compaction, e.g., Paul and Barras, 1998; Bird et al., 2007; Brain et al., 2012, 2015). Additionally, because the distribution of sedimentary proxies are primarily controlled by inundation frequency, non-stationarity of tides could result in higher or lower apparent changes in RSL over time. Such non-stationarity could arise due to local geomorphic changes, regional to global-scale changes in tidal dissipation or the natural frequency of ocean basins (e.g., Shennan et al., 2000; Uehara et al., 2006; Hill et al., 2011; Horton et al., 2013; Kemp et al., 2017c), changing wave climate (which affects inundation frequency), or changing base level of river flows due to variability in regional storm climatology or hydroclimate (e.g., Otvos, 1995, 2000; Friedrichs and Aubrey, 1994; Donnelly and Giosan, 2008; Komar and Allan, 2008; Jay et al., 2011; Hawkes et al., 2016).

A significant caveat of coral-based reconstructions of RSL is the difficulty of confirming that coral samples were not subject to post-depositional transport to different depth zones on a reef (Gischler and Hudson, 2004; Blanchon, 2005; Hubbard, 2013; Blanchon et al., 2017), which may result in a higher or lower elevation of apparent RSL depending on the direction of transport. Hubbard et al. (1990) and Blanchon et al. (2017) both suggest that many reefs in the western Atlantic are characterized by allochthonous deposits rather than *in situ* framework, which is why many researchers have suggested that careful analysis of reef facies and coral samples is critical for coral-based sea-level reconstructions (e.g., Gischler, 2006; Blanchon, 2005; Hubbard, 2013). Turbidity and coral mortality are two other potential sources of bias in coral-based reconstructions. High turbidity can truncate the depth distributions of corals, and can even prevent reef growth entirely (Neumann and Macintyre, 1985). If local water clarity is not taken into consideration when modeling coral depth distributions, then coral data from turbid reefs could result in anomalously low estimates of RSL. Corals are also sensitive to a variety of additional environmental perturbations including both high and low

temperature, salinity changes, nutrient inputs, and wave energy (Geister, 1977; Kleypas et al., 1999; Dullo, 2005). Significant changes in any of these environmental parameters could have caused local mortality of individual corals or entire reefs in the past, which could limit the availability of coral-based archives of RSL in some locations. For example, some researchers (e.g., Shinn et al., 2003; Hubbard et al., 2005; Precht and Miller, 2007; Hubbard, 2013; Stathakopoulos and Riegl, 2014) have suggested that both *A. palmata* and *A. cervicornis* were absent from some locations in the western Atlantic during periods in the Holocene and Pleistocene.

Careful consideration of the complete reef facies associated with a given coral sample is important not only for ensuring that the sample was collected *in situ* (Lighty et al., 1982; Gischler and Hudson, 2004; Blanchon, 2005), but also because it may allow researchers to narrow the most likely range of depths in which the coral grew (Neumann and Macintyre, 1985; Blanchon and Shaw, 1995). For example, transitions from slowly accreting facies dominated by massive species to more rapidly accreting sequences that include *A. palmata* have been characterized as shallowing-upward sequences that indicate a reef is growing closer to sea level through time (Neumann and Macintyre, 1985). Massive corals growing just below *A. palmata* in such a sequence are likely growing in the shallower end of their depth range. In contrast, depositional transitions from monospecific *A. palmata* framework to a reef with mixed *A. palmata* and massive facies, could suggest that the reef is getting deeper through time and the youngest *A. palmata* in the sequence may have grown in relatively deep water (Neumann and Macintyre, 1985; Blanchon et al., 2002). Similarly, because most coral taxa are known to grow in a variety of reef zones, which occur in different depths (i.e., reef crests, reef flats, lagoons, etc.), a complete characterization of the reef facies and an understanding of the reef's geomorphology is important for interpreting the depositional setting, and therefore the depth range, of coral archives.

The coral samples themselves can also provide valuable information about the depositional environment. Coralline orientation, skeletal growth patterns, and the presence of basal attachment surfaces can all be used to confirm the orientation of sub-fossil coral colonies in core records and to demonstrate whether the coral was collected *in situ* (Lighty et al., 1982; Blanchon and Perry, 2004; Blanchon et al., 2017). Taphonomic characteristics of coral skeletons may also provide justification for truncating the depth ranges of coral data (Lighty et al., 1982; Blanchon et al., 2002; Blanchon and Perry, 2004; Perry and Hepburn, 2008). For example, thick crusts of certain species of encrusting coralline algae, the presence of encrusting organisms such as the foraminifera *Homotrema rubrum* or vermetid gastropods, and evidence of certain bioeroding taxa, have all been shown to be characteristic of *A. palmata* growing on shallow-water reef crests (i.e., ≥ -2 m MSL; Blanchon and Perry, 2004; Perry and Hepburn, 2008). The precision of future models of RSL using coral-based archives could be improved by incorporating all available prior information on the characteristics

of coral samples and their depositional environments. To do this, databases need standardized metadata that can inform likelihood selection.

Bibliography

- Abdul, N.A., Mortlock, R.A., Wright, J.D., Fairbanks, R.G., 2016. Younger Dryas sea level and meltwater pulse 1B recorded in Barbados reef crest coral *Acropora palmata*. *Paleoceanography* 31, 330–344. doi:10.1002/2015PA002847.
- AGRRA, 2017. Atlantic Gulf Rapid Reef Assessment. Ocean Research & Education Foundation, Inc.
- Aitken, A.C., 1934. On Least-squares and Linear Combinations of Observations. *Proceedings of the Royal Society of Edinburgh* 55, 43–48.
- Allen, J.R.L., 2000. Holocene coastal lowlands in NW Europe: autocompaction and the uncertain ground. Geological Society, London, Special Publications 175, 239–252. doi:10.1144/GSL.SP.2000.175.01.18.
- Allison, M., Yuill, B., Törnqvist, T.E., Amelung, F., Dixon, T.H., Erkens, G., Stuurman, R., Jones, C., Milne, G.A., Steckler, M., Syvitski, J., Teatini, P., 2016. Global risks and research priorities for coastal subsidence. *Eos, Transactions American Geophysical Union* 97. doi:doi.org/10.1029/2016E0055013.
- van Andel, T.J., 1994. *New Views on an Old Planet: A History of Global Change*. Cambridge University Press, New York. doi:10.1002/joc.3370151110.
- Antonov, J.I., Levitus, S., Boyer, T.P., 2002. Steric sea level variations during 1957–1994: Importance of salinity. *Journal of Geophysical Research: Oceans* 107, 1803. doi:10.1029/2001JC000964.
- van Asselen, S., Stouthamer, E., van Asch, T., 2009. Effects of peat compaction on delta evolution: A review on processes, responses, measuring and modeling. *Earth-Science Reviews* 92, 35–51. doi:10.1016/j.earscirev.2008.11.001.
- Austermann, J., Mitrovica, J.X., Huybers, P., Rovere, A., 2017. Detection of a dynamic topography signal in last interglacial sea-level records. *Science Advances* 3, 1–8. doi:10.1126/sciadv.1700457.
- Banks, K.W., Riegl, B.M., Shinn, E.A., Piller, W.E., Dodge, R.E., 2007. Geomorphology of the Southeast Florida continental reef tract (Miami-Dade, Broward, and Palm Beach Counties, USA). *Coral Reefs* 26, 617–633. doi:10.1007/s00338-007-0231-0.

- Bard, E., Hamelin, B., Fairbanks, R.G., Zindler, A., 1990. Calibration of the ^{14}C timescale over the past 30,000 years using mass spectrometric U-Th ages from Barbados corals. *Nature* 345, 405–410. doi:10.1038/345405a0.
- Bayes, T., 1763. LII. An essay towards solving a problem in the doctrine of chances. By the late Rev. Mr. Bayes, F. R. S. communicated by Mr. Price, in a letter to John Canton, A. M. F. R. S. *Philosophical Transactions* 53, 370–418.
- Bird, M., Fifield, L., Teh, T., Chang, C., Shirlaw, N., Lambeck, K., 2007. An inflection in the rate of early mid-Holocene eustatic sea-level rise: A new sea-level curve from Singapore. *Estuarine, Coastal and Shelf Science* 71, 523–536. doi:10.1016/j.ecss.2006.07.004.
- Bird, M.I., Fifield, L.K., Chua, S., Goh, B., 2004. Calculating sediment compaction for radiocarbon dating of intertidal sediments. *Radiocarbon* 46, 421–435. doi:10.1017/S0033822200039734.
- Blanchon, P., 2005. Comments on “Corrected western Atlantic sea-level curve for the last 11,000 years based on calibrated ^{14}C dates from *Acropora palmata* framework and intertidal mangrove peat. *Coral Reefs* 24, 183–186. doi:10.1007/s00338-004-0472-0.
- Blanchon, P., 2017. *Encyclopedia of Modern Coral Reefs: Structure, Form and Process*. Springer Netherlands. chapter Meltwater Pulses. pp. 683–690.
- Blanchon, P., Eisenhauer, A., Fietzke, J., Liebetrau, V., 2009. Rapid sea-level rise and reef back-stepping at the close of the last interglacial highstand. *Nature* 458, 881–884. doi:10.1038/nature07933.
- Blanchon, P., Jones, B., Ford, D.C., 2002. Discovery of a submerged relic reef and shoreline off Grand Cayman: further support for an early Holocene jump in sea level. *Sedimentary Geology* 147, 253–270. doi:10.1016/S0037-0738(01)00143-9.
- Blanchon, P., Perry, C.T., 2004. Taphonomic differentiation of *Acropora palmata* facies in cores from Campeche Bank Reefs, Gulf of México. *Sedimentology* 51, 53–76. doi:10.1046/j.1365-3091.2003.00610.x.
- Blanchon, P., Richards, S., Bernal, J.P., Cerdeira-Estrada, S., Ibarra, M.S., Corona-Martinez, L., Martell-Dubois, R., 2017. Retrograde Accretion of a Caribbean Fringing Reef Controlled by Hurricanes and Sea-level Rise. *Frontiers in Earth Science* 5. doi:10.3389/feart.2017.00078.
- Blanchon, P., Shaw, J., 1995. Reef drowning during the last deglaciation: Evidence for catastrophic sea-level rise and ice-sheet collapse: Comment and Reply. *Geology* 23, 957–959.

- Blei, D.M., Kucukelbir, A., McAuliffe, J.D., 2017. Variational inference: A review for statisticians. *Journal of the American Statistical Association* 112, 859–877.
- Blom, H.A.P., Barshalom, Y., 1988. The Interacting Multiple Model Algorithm for Systems with Markovian Switching Coefficients. *Ieee Transactions on Automatic Control* 33, 780–783. doi:10.1109/9.1299.
- Bloom, A.L., 1964. Peat accumulation and compaction in a Connecticut coastal marsh. *Journal of Sedimentary Research* 34, 599–603.
- Blum, M.D., Tomkin, J.H., Purcell, A., Lancaster, R.R., 2008. Ups and downs of the Mississippi Delta. *Geology* 36, 675–678. doi:10.1130/G24728A.1.
- Brain, M.J., Kemp, A.C., Horton, B.P., Culver, S.J., Parnell, A.C., Cahill, N., 2015. Quantifying the contribution of sediment compaction to late Holocene salt-marsh sea-level reconstructions, North Carolina, USA. *Quaternary Research* 83, 41–51.
- Brain, M.J., Long, A.J., Woodroffe, S.A., Petley, D.N., Milledge, D.G., Parnell, A.C., 2012. Modelling the effects of sediment compaction on salt marsh reconstructions of recent sea-level rise. *Earth and Planetary Science Letters* 345, 180–193.
- Braun, J., 2010. The many surface expressions of mantle dynamics. *Nature Geoscience* 3, 825–833.
- Briffa, K., Shishov, V., Melvin, T., Vaganov, E., Grudd, H., Hantemirov, R., Eronen, M., Naurzbaev, M., 2008. Trends in recent temperature and radial tree growth spanning 2000 years across northwest Eurasia. *Philos Trans R Soc Lond B Biol Sci* 363, 2271–2284.
- Briggs, R.W., Sieh, K., Meltzner, A.J., Natawidjaja, D., Galetzka, J., Suwargadi, B., Hsu, Y.j., Simons, M., Hananto, N., Suprihanto, I., Prayudi, D., Avouac, J.P., Prawirodirdjo, L., Bock, Y., 2006. Deformation and Slip Along the Sunda Megathrust in the Great 2005 Nias-Simeulue Earthquake. *Science* 311, 1897–1901.
- Brock, J., Palaseanu-Lovejoy, M., Poore, R.Z., Nayegandhi, A., Wright, C.W., 2010. Holocene aggradation of the Dry Tortugas coral reef ecosystem. *Coral Reefs* 29, 857–868.
- Brown, J.H., 1984. On the Relationship between Abundance and Distribution of Species. *The American Naturalist* 124, 255–279.
- Budd, A.F., Stemann, T.A., Johnson, K.G., 1994. Stratigraphic Distributions of Genera and Species of Neogene to Recent Caribbean Reef Corals. *Journal of Paleontology* 68, 951–977.

- Cahill, N., 2018. IGP (Version 1.0) [Computer software]. Retrieved February 25, 2018, from <http://github.com/ncahill89/IGP>.
- Cahill, N., Kemp, A.C., Horton, B.P., Parnell, A.C., 2016. A Bayesian hierarchical model for reconstructing relative sea level: from raw data to rates of change. *Climate of the Past* 12, 525–542. doi:10.5194/cp-12-525-2016.
- Cahill, N., Kemp, A.C., Horton, B.P., Parnell, A.C., et al., 2015a. Modeling sea-level change using errors-in-variables integrated Gaussian processes. *The Annals of Applied Statistics* 9, 547–571.
- Cahill, N., Rahmstorf, S., Parnell, A.C., 2015b. Change points of global temperature. *Environmental Research Letters* 10, 084002. doi:10.1088/1748-9326/10/8/084002.
- Calafat, F.M., Chambers, D.P., Tsimplis, M.N., 2014. On the ability of global sea level reconstructions to determine trends and variability. *Journal of Geophysical Research: Oceans* 119, 1572–1592.
- CALIB, 2017. Conventional radiocarbon ages corrected for isotope fractionation. URL: <http://calib.qub.ac.uk/calib/fractionation.html>.
- Camoin, G.F., Webster, J.M., 2015. Coral reef response to Quaternary sea-level and environmental changes: State of the science. *Sedimentology* 62, 401–428.
- Carson, J., Crucifix, M., Preston, S., Wilkinson, R.D., 2018. Bayesian model selection for the glacial–interglacial cycle. *Journal of the Royal Statistical Society: Series C (Applied Statistics)* 67, 25–54.
- Cheng, H., Edwards, R.L., Shen, C.C., Polyak, V.J., Asmerom, Y., Woodhead, J., Hellstrom, J., Wang, Y., Kong, X., Spötl, C., Wang, X., Jr., E.C.A., 2013. Improvements in 230th dating, 230th and 234u half-life values, and u–th isotopic measurements by multi-collector inductively coupled plasma mass spectrometry. *Earth and Planetary Science Letters* 371–372, 82–91. doi:10.1016/j.epsl.2013.04.006.
- Church, J.A., Clark, P.U., Cazenave, A., Gregory, J.M., Jevrejeva, S., Levermann, A., Merrifield, M.A., Milne, G.A., Nerem, R.S., Nunn, P.D., Payne, A.J., Pfeffer, W.T., Stammer, D., Unnikrishnan, A.S., 2013a. Sea Level Change, in: Stocker, T.F., Qin, D., Plattner, G.K., Tignor, M., Allen, S.K., Boschung, J., Nauels, A., Xia, Y., Bex, V., Midgley, P.M. (Eds.), *Climate Change 2013: The Physical Science Basis. Contribution of Working Group I to the Fifth Assessment Report of the Intergovernmental Panel on Climate Change*. Cambridge University Press, Cambridge, United Kingdom, and New York, NY, USA.
- Church, J.A., Monselesan, D., Gregory, J.M., Marzeion, B., 2013b. Evaluating the ability of process based models to project sea-level change. *Environmental Research Letters* 8, 014051. doi:10.1088/1748-9326/8/1/014051.

- Church, J.A., White, N.J., 2004. Estimates of the regional distribution of sea level rise over the 1950-2000 period. *Journal of Climate* 17, 2609–2625.
- Church, J.A., White, N.J., 2006. A 20th century acceleration in global sea-level rise. *Geophysical Research Letters* 33. doi:10.1029/2005GL024826.
- Church, J.A., White, N.J., 2011. Sea-Level Rise from the Late 19th to the Early 21st Century. *Surveys in Geophysics* 32, 585–602. doi:10.1007/s10712-011-9119-1.
- Clark, J.A., Farrell, W.E., Peltier, W.R., 1978. Global changes in postglacial sea level: A numerical calculation. *Quaternary Research* 9, 265–287. doi:10.1016/0033-5894(78)90033-9.
- Clark, P.U., Dyke, A.S., Shakun, J.D., Carlson, A.E., Clark, J., Wohlfarth, B., Mitrovica, J.X., Hostetler, S.W., McCabe, A.M., 2009. The Last Glacial Maximum. *Science* 325, 710–714. doi:10.1126/science.1172873.
- Clark, P.U., Mix, A.C., 2002. Ice sheets and sea level of the Last Glacial Maximum. *Quaternary Science Reviews* 21, 1–7.
- Conrad, C.P., Husson, L., 2009. Influence of dynamic topography on sea level and its rate of change. *Lithosphere* 1, 110–120. doi:10.1130/L32.1.
- Cressie, N., Wikle, C.K., 2015. *Statistics for spatio-temporal data*. John Wiley & Sons, Ltd Sons.
- Dangendorf, S., Marcos, M., Wöppelmann, G., Conrad, C.P., Frederikse, T., Riva, R., 2017. Reassessment of 20th century global mean sea level rise. *Proceedings of the National Academy of Sciences* 114, 5946–5951.
- DeConto, R.M., Pollard, D., 2016. Contribution of Antarctica to past and future sea-level rise. *Nature* 531, 591–597.
- Dirren, S., Hakim, G.J., 2005. Toward the assimilation of time-averaged observations. *Geophysical Research Letters* 32. doi:10.1029/2004GL021444.
- Domingues, C.M., Church, J.A., White, N.J., Gleckler, P.J., Wijffels, S.E., Barker, P.M., Dunn, J.R., 2008. Improved estimates of upper-ocean warming and multi-decadal sea-level rise. *Nature* 453. doi:doi:10.1038/nature07080.
- Donnelly, J.P., Giosan, L., 2008. Tempestuous highs and lows in the Gulf of Mexico. *Geology* 36, 751–752. doi:10.1130/focus092008.1.

- Douglas, B.C., 1991. Global Sea-Level Rise. *Journal of Geophysical Research-Oceans* 96, 6981–6992. doi:10.1029/91jc00064.
- Douglas, B.C., 1997. Global sea rise: A redetermination. *Surveys in Geophysics* 18, 279–292. doi:10.1023/A:1006544227856.
- Dullo, W.C., 2005. Coral growth and reef growth: a brief review. *Facies* 51, 33–48.
- Dura, T., Engelhart, S.E., Vacchi, M., Horton, B.P., Kopp, R.E., Peltier, W.R., 2016. The Role of Holocene Relative Sea-Level Change in Preserving Records of Subduction Zone Earthquakes. *Current Climate Change Reports* 2. doi:10.1007/s40641-016-0041-y.
- Düsterhus, A., Rovere, A., Carlson, A.E., Horton, B.P., Klemann, V., Tarasov, L., Barlow, N.L.M., Bradwell, T., Clark, J., Dutton, A., Gehrels, W.R., Hibbert, F.D., Hijma, M.P., Khan, N., Kopp, R.E., Sivan, D., Törnqvist, T.E., 2016. Palaeo-sea-level and palaeo-ice-sheet databases: problems, strategies, and perspectives. *Climate of the Past* 12, 911–921. doi:10.5194/cp-12-911-2016.
- Dutton, A., Carlson, A.E., Long, A.J., Milne, G.A., Clark, P.U., DeConto, R., Horton, B.P., Rahmstorf, S., Raymo, M.E., 2015. Sea-level rise due to polar ice-sheet mass loss during past warm periods. *Science* 349. doi:10.1126/science.aaa4019.
- Dutton, A., Lambeck, K., 2012. Ice Volume and Sea Level During the Last Interglacial. *Science* 337, 216–219.
- Edwards, R.J., Horton, B.P., 2006. Developing detailed records of relative sea-level change using a foraminiferal transfer function: an example from North Norfolk, UK. *Philos Trans A Math Phys Eng Sci* 364, 973–971.
- Egbert, G.D., Erofeeva, S.Y., 2002. Efficient Inverse Modeling of Barotropic Ocean Tides. *Journal of Atmospheric and Oceanic Technology* 19, 183–204.
- Engelhart, S.E., Horton, B.P., 2012. Holocene sea level database for the Atlantic coast of the United States. *Quaternary Science Reviews* 54, 12–25. doi:10.1016/j.quascirev.2011.09.013.
- Engelhart, S.E., Horton, B.P., Douglas, B.C., Peltier, W.R., Törnqvist, T.E., 2009. Spatial variability of late Holocene and 20th century sea-level rise along the Atlantic coast of the United States. *Geology* 37, 1115–1118. doi:10.1130/G30360A.1.
- Fairbanks, R.G., 1989. A 17,000-year glacio-eustatic sea level record: influence of glacial melting rates on the younger dryas event and deep-ocean circulation. *Nature* 342, 1476–4687.

- Farrell, W.E., Clark, J.A., 1976. On postglacial sea level. *Geophysical Journal International* 46, 647–667.
- Flemming, N.C., Roberts, D.G., 1973. Tectono-eustatic Changes in Sea Level and Seafloor Spreading. *Nature* 243, 19–22.
- Friedrichs, C.T., Aubrey, D.G., 1994. Tidal propagation in strongly convergent channels. *Journal of Geophysical Research: Oceans* 99, 3321–3336.
- Fritts, H., 1991. Reconstructing large-scale climatic patterns from tree-ring data. The University of Arizona Press, Tucson.
- Fukumori, I., Wang, O., 2013. Origins of heat and freshwater anomalies underlying regional decadal sea level trends. *Geophysical Research Letters* 40. doi:10.1002/grl.50164.
- Gabriel, K.R., Zamir, S., 1979. Lower rank approximation of matrices by least squares with any choice of weights. *Technometrics* 21, 489–498.
- Gehrels, W.R., Belknap, D.F., Black, S., Newnham, R.M., 2002. Rapid sea-level rise in the Gulf of Maine, USA, since AD 1800. *The Holocene* 12, 383–389.
- Geister, J., 1977. The Influence of Wave Exposure on the Ecological Zonation of Caribbean Coral Reefs, in: *Proceedings of the 3rd International Coral Reef Symposium*.
- Gelb, A., Kasper, J., Nash, R., Price, C.F., Sutherland, A., 1974. *Applied Optimal Interpolation*. M.I.T. Press, Cambridge.
- Gelman, A., Brooks, S., Jones, G.L. (Eds.), 2011. *Handbook of Markov Chain Monte Carlo*. Chapman & Hall/CRC Press.
- Gelman, A., Carlin, J.B., Stern, H.S., Dunson, D.B., Vehtari, A., Rubin, D.B., 2013. *Bayesian Data Analysis*. Third ed., Chapman & Hall/CRC Press, London.
- Gharineiat, Z., Deng, X., 2015. Application of the Multi-Adaptive Regression Splines to Integrate Sea Level Data from Altimetry and Tide Gauges for Monitoring Extreme Sea Level Events. *Marine Geodesy* 38. doi:10.1080/01490419.2015.1036183.
- Gill, A.E., Niller, P.P., 1973. The theory of the seasonal variability in the ocean. *Deep Sea Research and Oceanographic Abstracts* 20, 141–177.
- Gischler, E., 2006. Comment on “Corrected western Atlantic sea-level curve for the last 11,000 years based on calibrated 14C dates from *Acropora palmata* framework and intertidal mangrove peat” by Toscano and

- Macintyre. *Coral Reefs* 22:257–270 (2003), and their response in *Coral Reefs* 24:187–190 (2005). *Coral Reefs* 25, 273–0279.
- Gischler, E., Hudson, J.H., 2004. Holocene development of the Belize Barrier Reef. *Sedimentary Geology* 164, 223–236.
- Goldberger, A.S., 1962. Best Linear Unbiased Prediction in the Generalized Linear Regression Model. *Journal of the American Statistical Association* 57, 369–375.
- Golledge, N.R., Menviel, L., Carter, L., Fogwill, C.J., England, M.H., Cortese, G., H., L.R., 2014. Antarctic contribution to meltwater pulse 1A from reduced Southern Ocean overturning. *Nature Communications* 5. doi:10.1038/ncomms6107.
- Golub, G., 1973. Some modified matrix eigenvalue problems. *SIAM Review* 15, 318–344.
- Golub, G., Hansen, J., O’Leary, D., 1999. Tikhonov regularization and total least squares. *SIAM Journal on Matrix Analysis and Applications* 21, 185–194.
- Gornitz, V., Lebedeff, S., Hansen, J., 1982. Global Sea Level Trend in the Past Century. *Science* 215, 1611–1614.
- Guilbault, J.P., Clague, J.J., Lapointe, M., 1996. Foraminiferal evidence for the amount of coseismic subsidence during a late holocene earthquake on vancouver island, west coast of canada. *Quaternary Science Reviews* 15, 913–937.
- Haigh, I.D., Eliot, M., Pattiaratchi, C., 2011. Global influences of the 18.61 year nodal cycle and 8.85 year cycle of lunar perigee on high tidal levels. *Journal of Geophysical Research: Oceans* 116. doi:10.1029/2010JC006645.
- Hartikainen, J., Särkkä, S., 2010. Kalman filtering and smoothing solutions to temporal Gaussian process regression models, in: *IEEE International Workshop on Machine Learning for Signal Processing (MLSP)*. doi:10.1109/MLSP.2010.5589113.
- Haslett, J., Whiley, M., Bhattacharya, S., Salter-Townshend, M., Wilson, S.P., Allen, J.R.M., Huntley, B., Mitchell, F.J.G., 2006. Bayesian palaeoclimate reconstruction. *Journal of the Royal Statistical Society: Series A (Statistics in Society)* 169, 395–438.
- Haslett, S.K., Davies, P., Curr, R.H.F., Davies, C.F.C., Kennington, K., King, C.P., Margetts, A.J., 1998. Evaluating late-Holocene relative sea-level change in the Somerset Levels, southwest Britain. *The Holocene* 8, 197–207. doi:10.1191/095968398669499299.

- Hastings, W., 1970. Monte Carlo sampling methods using Markov chains and their application. *Biometrics* 57, 97–190.
- Hawkes, A.D., Kemp, A.C., Donnelly, J.P., Horton, B.P., Peltier, W.R., Cahill, N., Hill, D.F., Ashe, E., Alexander, C.R., 2016. Relative sea-level change in northeastern Florida (USA) during the last 8.0 ka. *Quaternary Science Reviews* 142, 90–101. doi:10.1016/j.quascirev.2016.04.016.
- Hay, C., Mitrovica, J.X., Gomez, N., Creveling, J., Austermann, J., Kopp, R.E., 2014. The sea-level fingerprints of ice-sheet collapse during interglacial periods. *Quaternary Science Reviews* 87, 60–69.
- Hay, C.C., Morrow, E., Kopp, R.E., Mitrovica, J.X., 2013. Estimating the sources of global sea level rise with data assimilation techniques. *Proceedings of the National Academy of Sciences of the United States of America* 110, 3692–3699.
- Hay, C.C., Morrow, E., Kopp, R.E., Mitrovica, J.X., 2015. Probabilistic reanalysis of twentieth-century sea-level rise. *Nature* 517, 481–484.
- Hay, C.C., Morrow, E., Kopp, R.E., Mitrovica, J.X., 2017. On the robustness of Bayesian fingerprinting estimates of global sea-level change. *Journal of Climate* 30, 3025–3038.
- Hay, W.W., Leslie, M.A., 1990. *Studies in Geophysics: Sea-Level Change*. National Academy Press. chapter Could Possible Changes in Global Groundwater Reservoir Cause Eustatic Sea-Level Fluctuations?
- Hays, J.D., Pitman, W.C., 1973. Lithospheric Plate Motion, Sea Level Changes and Climatic and Ecological Consequences. *Nature* 246, 18–22.
- Hibbert, F.D., Rohling, E.J., Dutton, A., Williams, F.H., Chutcharavan, P.M., Zhao, C., Tamisiea, M.E., 2016. Coral indicators of past sea-level change: A global repository of U-series dated benchmarks. *Quaternary Science Reviews* 145, 1–56. doi:10.1016/j.quascirev.2016.04.019.
- Hijma, M., Engelhart, S.E., Törnqvist, T.E., Horton, B.P., Hu, P., Hill, D.F., 2015. *Handbook of Sea-Level Research*. John Wiley & Sons, Ltd. chapter A protocol for a geological sea-level database. doi:10.1002/9781118452547.ch34.
- Hill, D.F., Griffiths, S.D., Peltier, W.R., Horton, B.P., Törnqvist, T.E., 2011. High-resolution numerical modeling of tides in the western Atlantic, Gulf of Mexico, and Caribbean Sea during the Holocene. *Journal of Geophysical Research: Oceans* 116. doi:10.1029/2010jc006896.
- Hoffman, J.S., Clark, P.U., Parnell, A.C., He, F., 2017. Regional and global sea-surface temperatures during the last interglaciation. *Science* 355, 276–279. doi:10.1126/science.aai8464.

- Holgate, S.J., 2007. On the decadal rates of sea level change during the twentieth century. *Geophysical Research Letters* 34. doi:10.1029/2006GL028492.
- Holgate, S.J., Matthews, A., Woodworth, P.L., Rickards, L.J., Tamisiea, M.E., Bradshaw, E., Foden, P.R., Gordon, K.M., Jevrejeva, S., Pugh, J., 2013. New Data Systems and Products at the Permanent Service for Mean Sea Level. *Journal of Coastal Research* 29, 493–504.
- Hopley, D., 1982. *The Geomorphology of the Great Barrier Reef: Quaternary Development of Coral Reefs*. Wiley.
- Horton, B.P., Engelhart, S.E., Hill, D.F., Kemp, A.C., Nikitina, D., Miller, K.G., Peltier, W.R., 2013. Influence of tidal-range change and sediment compaction on Holocene relative sea-level change in New Jersey, USA. *Journal of Quaternary Science* 28, 403–411. doi:10.1002/jqs.2634.
- Horton, B.P., Gibbard, P., Milne, G.A., Morley, R.J., Purintavaragul, C., Stargardt, J.M., 2005. Holocene sea levels and palaeoenvironments, Malay-Thai Peninsula, southeast Asia. *The Holocene* 15, 1199–1213. doi:10.1191/0959683605h1891rp.
- Horton, B.P., Shennan, I., 2009. Compaction of Holocene strata and the implications for relative sealevel change on the east coast of England. *Geology* 37, 1083–1086. doi:10.1130/G30042A.1.
- Hu, P., 2010. Developing a quality-controlled postglacial sea-level database for coastal Louisiana to assess conflicting hypotheses of Gulf Coast sea-level change (MSc Thesis). Tulane University, New Orleans. Master's thesis. Tulane University.
- Hubbard, D., 2013. Holocene accretion rates and styles for Caribbean coral reefs: Lessons for the past and future. chapter Deposits, Architecture, and Controls of Carbonate Margin, Slope and Basinal Settings.
- Hubbard, D.K., 2009. Depth-Related and Species-Related Patterns of Holocene Reef Accretion in the Caribbean and Western Atlantic: A Critical Assessment of Existing Models. John Wiley & Sons, Ltd. pp. 1–18. doi:10.1002/9781444312065.ch1.
- Hubbard, D.K., Miller, A.I., Scaturro, D., 1990. Production and cycling of calcium carbonate in a shelf-edge reef system (St. Croix, U.S. Virgin Islands): applications to the nature of reef systems in the fossil record. *Journal of Sedim. Petrology* 60, 335–360.
- Hubbard, D.K., Zankl, H., Van Heerden, I., Gill, I.P., 2005. Holocene Reef Development Along the North-eastern St. Croix Shelf, Buck Island, U.S. Virgin Islands. *Journal of Sedimentary Research* 75, 97–113.

- Hughes, J.F., Mathewes, R.W., Clague, J.J., 2002. Use of pollen and vascular plants to estimate coseismic subsidence at a tidal marsh near Tofino, British Columbia. *Palaeogeography, Palaeoclimatology, Palaeoecology* 185, 145–161.
- Huston, M., 1985. Variation in coral growth rates with depth at Discovery Bay, Jamaica. *Coral Reefs* 4.
- Jaffey, A.H., Flynn, K.F., Glendenin, L.E., Bentley, W.C., Essling, A.M., 1971. Precision Measurement of Half-Lives and Specific Activities of ^{235}U and ^{238}U . *Physical Review C* 4, 1889–1906. doi:10.1103/PhysRevC.4.1889.
- Jay, A.D., Leffler, K., Degens, S., 2011. Long-Term Evolution of Columbia River Tides. *Journal of Waterway, Port, Coastal, and Ocean Engineering* 137, 182–191.
- Jelgersma, S., 1961. Holocene sea-level changes in the Netherlands. Ph.D. thesis. Leiden University.
- Jevrejeva, S., Grinsted, A., Moore, J.C., 2009. Anthropogenic forcing dominates sea level rise since 1850. *Geophysical Research Letters* 36. doi:10.1029/2009GL040216.
- Jevrejeva, S., Grinsted, A., Moore, J.C., Holgate, S.J., 2006. Nonlinear trends and multiyear cycles in sea level records. *Journal of Geophysical Research-Oceans* 111. doi:10.1029/2005JC003229.
- Jevrejeva, S., Jackson, L.P., Riva, R.E.M., Grinsted, A., Moore, J.C., 2016. Coastal sea level rise with warming above 2 °C. *Proceedings of the National Academy of Sciences* 113, 13342–13347.
- Jevrejeva, S., Moore, J.C., Grinsted, A., Woodworth, P.L., 2008. Recent global sea level acceleration started over 200 years ago? *Geophysical Research Letters* 35. doi:10.1029/2008GL033611.
- Johnson, G.C., Chambers, D.P., 2013. Ocean bottom pressure seasonal cycles and decadal trends from GRACE Release-05: ocean circulation implications. *Journal of Geophysical Research: Oceans* 118. doi:10.1002/jgrc.20307.
- Kalman, R., 1960. A new approach to linear filtering and prediction problems. *Transactions of the ASME - Journal of Basic Engineering* 82, 35–45.
- Kaye, A.C., Barghoorn, S.E., 1964. Late Quaternary Sea-Level Change and Crustal Rise at Boston, Massachusetts, with Notes on the Autocompaction of Peat. *Geological Society of America Bulletin* 75, 63–80. doi:10.1130/0016-7606(1964)75[63:LQSCAC]2.0.CO;2.
- Kelsey, H.M., Engelhart, S.E., Pilarczyk, J.E., Horton, B.P., Rubin, C.M., Daryono, M.R., Ismail, N., Hawkes, A.D., Bernhardt, C.E., Cahill, N., 2015. Accommodation space, relative sea level, and the archiving of paleo-earthquakes along subduction zones. *Geology* 43, 675–678. doi:10.1130/G36706.1.

- Kemp, A., Hawkes, A., Donnelly, J., Vane, C.H., Horton, B.P., Hill, T., Anisfeld, S., Parnell, A., Cahill, N., 2015. Relative sea-level change in Connecticut (USA) during the last 2200 years. *Earth and Planetary Science Letters* 428, 217–229.
- Kemp, A.C., Bernhardt, C.E., Horton, B.P., Kopp, R.E., Vane, C.H., Peltier, W.R., Hawkes, A.D., Donnelly, J.P., Parnell, A.C., Cahill, N., 2014. Late Holocene sea-and land-level change on the US southeastern Atlantic coast. *Marine Geology* 357, 90–100.
- Kemp, A.C., Hill, T.D., Vane, C.H., Cahill, N., Orton, P., Talke, S.A., Parnell, A., Sanborn, K., Hartig, E.K., 2017a. Relative sea-level trends in New York City during the past 1500 years. *The Holocene* 27, 1169–1186.
- Kemp, A.C., Horton, B., Donnelly, J.P., Mann, M.E., Vermeer, M., Rahmstorf, S., 2011. Climate related sea-level variations over the past two millennia. *Proceedings of the National Academy of Sciences* 108, 11017–11022.
- Kemp, A.C., Horton, B.P., Vane, C.H., Bernhardt, C., Corbett, D.R., Engelhart, S.E., Anisfeld, S.C., Parnell, A.C., Cahill, N., 2017b. Sea-level change during the last 2500 years in New Jersey, USA. *Quaternary Science Reviews* 81, 91–104.
- Kemp, A.C., Horton, B.P., Vane, C.H., Corbett, D.R., Bernhardt, C., Engelhart, S.E., Anisfeld, S.C., Parnell, A.C., Cahill, N., 2013. Sea-level change during the last 2500 years in New Jersey, USA. *Quaternary Science Reviews* 81, 90–104.
- Kemp, A.C., Kegel, J.J., Culver, S.J., Barber, D.C., Mallinson, D.J., Leorri, E., Bernhardt, C.E., Cahill, N., Riggs, S.R., Woodson, A.L., Mulligan, R.P., Horton, B.P., 2017c. Extended late Holocene relative sea-level histories for North Carolina, USA. *Quaternary Science Reviews* 160, 13–30.
- Khan, N.S., Ashe, E.L., Horton, B.P., Dutton, A., Kopp, R.E., Brocard, G., Engelhart, S.E., Hill, D.F., Peltier, W., Vane, C.H., Scatena, F.N., 2017. Drivers of Holocene sea-level change in the Caribbean. *Quaternary Science Reviews* 155, 13 – 36.
- Khan, N.S., Ashe, E.L., Shaw, T.A., Vacchi, M., Walker, J., Peltier, W., Kopp, R.E., Horton, B.P., 2015. Holocene relative sea-level changes from near-, intermediate-, and far-field locations. *Current Climate Change Reports* 1, 247–262.
- Kleypas, J.A., McManus, J.W., Lambert, A.B., Meñez, A.B., 1999. Environmental Limits to Coral Reef Development: Where Do We Draw the Line? *American Zoologist* 39, 146–159.

- Kohl, A., 2014. Detecting processes contributing to interannual halosteric and thermosteric sea level variability. *Journal of Climate* 27, 2417–2426.
- Komar, P.D., Allan, J.C., 2008. Increasing Hurricane-Generated Wave Heights along the U.S. East Coast and Their Climate Controls. *Journal of Coastal Research* 24, 479–488.
- Kopp, R.E., 2013. Does the mid-Atlantic United States sea level acceleration hot spot reflect ocean dynamic variability? *Geophysical Research Letters* 40, 3981–3985. doi:10.1002/grl.50781.
- Kopp, R.E., 2016. CESL-STEHM-GP (Version 1.0) [Computer software]. Retrieved February 25, 2018 from <http://github.com/bobkopp/CESL-STEHM-GP>.
- Kopp, R.E., Hay, C.C., Little, C.M., Mitrovica, J.X., 2015a. Geographic Variability of Sea-Level Change. *Current Climate Change Reports* 1, 192–204. doi:10.1007/s40641-015-0015-5.
- Kopp, R.E., Horton, B.P., Kemp, A.C., Tebaldi, C., 2015b. Past and future sea-level rise along the coast of North Carolina, United States. *Climatic Change* 132, 693–707. doi:10.1007/s10584-015-1451-x.
- Kopp, R.E., Horton, R.M., Little, C.M., Mitrovica, J.X., Oppenheimer, M., Rasmussen, D.J., Strauss, B.H., Tebaldi, C., 2014. Probabilistic 21st and 22nd century sea-level projections at a global network of tide-gauge sites. *Earth's Future* 2, 383–406. doi:10.1002/2014EF000239.
- Kopp, R.E., Kemp, A.C., Bittermann, K., Horton, B.P., Donnelly, J.P., Gehrels, W.R., Hay, C.C., Mitrovica, J.X., Morrow, E.D., Rahmstorf, S., 2016. Temperature-driven global sea-level variability in the Common Era. *Proceedings of the National Academy of Sciences* 113, E1434–E1441. doi:10.1073/pnas.1517056113.
- Kopp, R.E., Simons, F.J., Mitrovica, J.X., Maloof, A.C., Oppenheimer, M., 2009. Probabilistic assessment of sea level during the last interglacial stage. *Nature* 462, 863–867. doi:10.1038/nature08686.
- Kuffner, I.B., Toth, L.T., 2017. A geological perspective on the degradation and conservation of western Atlantic coral reefs. *Conservation Biology* 30, 706–715.
- Lambeck, K., Rouby, H., Purcell, A., Sun, Y., Sambridge, M., 2014. Sea level and global ice volumes from the Last Glacial Maximum to the Holocene. *Proceedings of the National Academy of Sciences* 111, 15296–15303. doi:10.1073/pnas.1411762111.
- Legendre, A.M., 1805. *On the Method of Least Squares* .
- Leonard, N.D., 2016. Holocene sea level instability in the southern Great Barrier Reef, Australia: high-precision U–Th dating of fossil microatolls. *Coral Reefs* 35, 625–639.

- Lewis, S.E., Wüst, R.A.J., Webster, J.M., Shields, G.A., 2008. Mid-late Holocene sea-level variability in eastern Australia. *Terra Nova* 20, 74–81.
- Li, X., Rowley, R.J., Kostelnick, J.C., Braaten, D., Meisel, J., Hulbutta, K., 2009. GIS analysis of global impacts from sea level rise. *Photogrammetric Engineering & Remote Sensing* 75, 807–818.
- Lidz, B.H., Reich, C.D., Shinn, 2003. Regional Quaternary submarine geomorphology in the Florida Keys. *Geological Society of America Bulletin* 115, 845–866.
- Lidz, B.H., Shinn, E.A., 1991. Paleoshorelines, reefs, and a rising sea: south Florida, USA. *Journal of Coastal Research* 7, 203–229.
- Lighty, R.G., Macintyre, I.G., Stuckenrath, R., 1982. *Acropora palmata* reef framework: A reliable indicator of sea level in the western atlantic for the past 10,000 years. *Coral Reefs* 1, 125–130. doi:10.1007/BF00301694.
- Long, A., Barlow, N., Gehrels, W., Saher, M., Woodworth, P., Scaife, R., Brain, M., Cahill, N., 2014. Contrasting records of sea-level change in the eastern and western North Atlantic during the last 300 years. *Earth and Planetary Science Letters* 388, 110–122.
- Mallinson, D., Hilne, A., Hallock, P., Locker, S., Shinn, E.A., Naar, D., Donahue, B., Weaver, D., 2003. Development of small carbonate banks on the south Florida platform margin: response to sea level and climate change. *Marine Geology* 199, 45–63.
- Mann, M.E., Bradley, R.S., Hughes, M.K., 1998. Global-scale temperature patterns and climate forcing over the past six centuries. *Nature* 392, 779–787.
- McHutchon, A., Rasmussen, C.E., 2011. Gaussian Process Training with Input Noise, in: Shawe-Taylor, J., Zemel, R.S., Bartlett, P.L., Pereira, F., Weinberger, K.Q. (Eds.), *Advances in Neural Information Processing Systems* 24. Curran Associates, Inc., pp. 1341–1349.
- McLean, R., Kench, P., 2015. Destruction or persistence of coral atoll islands in the face of 20th and 21st century sea-level rise? *Wiley Interdisciplinary Reviews: Climate Change* 6, 445–463.
- Meltzner, A.J., Sieh, K., Chiang, H.W., Shen, C.C., Suwargadi, B.W., Natawidjaja, D.H., Philiposian, B., Briggs, R.W., 2012. Persistent termini of 2004- and 2005-like ruptures of the Sunda megathrust. *Journal of Geophysical Research: Solid Earth* 117. doi:10.1029/2011JB008888.
- Meltzner, A.J., Sieh, K., Chiang, H.W., Shen, C.C., Suwargadi, B.W., Natawidjaja, D.H., Philiposian, B.E., Briggs, R.W., Galetzka, J., 2010. Coral evidence for earthquake recurrence and an A.D. 1390–1455 cluster

- at the south end of the 2004 Aceh–Andaman rupture. *Journal of Geophysical Research: Solid Earth* 115. doi:10.1029/2010JB007499.
- Meltzner, A.J., Sieh, K., Chiang, H.W., Wu, C.C., Tsang, L.L., Shen, C.C., Hill, E.M., Suwargadi, B.W., Natawidjaja, D.H., Philibosian, B., Briggs, R.W., 2015. Time-varying interseismic strain rates and similar seismic ruptures on the Nias–Simeulue patch of the Sunda megathrust. *Quaternary Science Reviews* 122, 258–281.
- Meltzner, A.J., Switzer, A.D., Horton, B.P., Ashe, E.L., Qiu, Q., Hill, D.F., Bradley, S.L., Kopp, R.E., Hill, E.M., Majewski, J.M., Natawidjaja, D.H., Suwargadi, B.W., 2017. Half-metre sea-level fluctuations on centennial timescales from mid-Holocene corals of Southeast Asia. *Nature Communications* 8. doi:10.1038/ncomms14387.
- Meltzner, A.J., Woodroffe, C.D., 2015. *Handbook of Sea-Level Research*. John Wiley & Sons, Ltd. chapter Coral microatolls.
- members, N.G.I.C.P., 2004. High-resolution record of Northern Hemisphere climate extending into the last interglacial period. *Nature* 431, 147–151.
- Miller, K.G., Kopp, R.E.E., Horton, B.P., Browning, J.V., Kemp, A.C., 2013. A geological perspective on sea-level rise and its impacts along the U.S. mid-Atlantic coast. *Earth's Future* 1, 3–18.
- Milne, G.A., Gehrels, W.R., Hughes, C.W., Tamisiea, M.E., 2009. Identifying the causes of sea-level change. *Nature Geoscience* 2, 471–478. doi:10.1038/ngeo544.
- Milne, G.A., Long, A.J., Bassett, S.E., 2005. Modelling Holocene relative sea-level observations from the Caribbean and South America. *Quaternary Science Reviews* 24, 1183–1202. doi:10.1016/J.Quascirev.2004.10.005.
- Mitrovica, J.X., Gomez, N., Morrow, E., Hay, C., Latychev, K., Tamisiea, M.E., 2011. On the robustness of predictions of sea level fingerprints. *Geophysical Journal International* 187, 729–742. doi:10.1111/j.1365-246X.2011.05090.x.
- Mitrovica, J.X., Milne, G.A., 2002. On the origin of late Holocene sea-level highstands within equatorial ocean basins. *Quaternary Science Reviews* 21, 2179–2190. doi:10.1016/S0277-3791(02)00080-X.
- Mitrovica, J.X., Milne, G.A., 2003. On postglacial sea level: 1. General theory. *Geophysical Journal International* 154, 253–267.

- Mitrovica, J.X., Peltier, W.R., 1991. On postglacial geoid subsidence over the equatorial oceans. *Journal of Geophysical Research: Solid Earth* 96, 20053–20071.
- Mitrovica, J.X., Tamisiea, M.E., Davis, J.L., Milne, G.A., 2001. Recent mass balance of polar ice sheets inferred from patterns of global sea-level change. *Nature* 409. doi:10.1038/35059054.
- Morrow, E.D., 2014. Estimates of land ice changes from sea level and gravity observations. Ph.D. thesis. Harvard University.
- National Ocean and Atmospheric Administration, 2017. National Ocean and Atmospheric Administration. National Oceanic & Atmospheric Administration URL: <http://www.noaa.gov/>.
- Neumann, A.C., Macintyre, I.G., 1985. Reef response to sea level rise: Keep-up, catch-up, or give-up. *Proceedings of the Fifth International Coral Reef Congress*. volume 3.
- OBIS, 2017. Data from the Ocean Biogeographic Information System. Intergovernmental Oceanographic Commission of UNESCO .
- Ohlwein, C., Wahl, E.R., 2012. Review of probabilistic pollen-climate transfer methods. *Quaternary Science Reviews* 31, 17–29.
- Otvos, E.G., 1995. Multiple Pliocene-Quaternary Marine Highstands, Northeast Gulf Coastal Plain: Fallacies and Facts. *Journal of Coastal Research* 11, 984–1002.
- Otvos, E.G., 2000. Beach ridges – definitions and significance. *Geomorphology* 32, 83–108.
- Pandolfi, J.M., Jackson, J.B., 2006. Ecological persistence interrupted in Caribbean coral reefs. *Ecology Letters* 9, 818–826.
- Parnell, A., Haslett, J., Allen, J., Buck, C., Huntley, B., 2008. A flexible approach to assessing synchronicity of past events using Bayesian reconstructions of sedimentation history. *Quaternary Science Reviews* 27, 1872–1885.
- Parnell, A.C., 2005. The statistical analysis of former sea level. Ph.D. thesis. University of Sheffield.
- Parnell, A.C., Doan, T.K., Salter-Townshend, M., Allen, J.R.M., Huntley, B., Haslett, J., 2015. Bayesian inference for palaeoclimate with time uncertainty and stochastic volatility. *Journal of the Royal Statistical Society. Series C (Applied Statistics)* 64. doi:10.1111/rssc.12065.
- Parrenin, F., Barnola, J.M., Beer, J., Blunier, T., Castellano, E., Chappellaz, J., Dreyfus, G., Fischer, H., Fujita, S., Jouzel, J., Kawamura, K., Lemieux-Dudon, B., Loulergue, L., Masson-Delmotte, V., Narcisi,

- B., Petit, J.R., Raisbeck, G., Raynaud, D., Ruth, U., Schwander, J., Severi, M., Spahni, R., Steffensen, J.P., Svensson, A., Udisti, R., Waelbroeck, C., Wolff, E., 2007. The EDC3 chronology for the EPICA Dome C ice core. *Climate of the Past* 3, 485–497.
- Pattengill-Semmens, C., Gittings, S.R., Shyka, T., 2000. Flower Garden Banks National Marine Sanctuary: A rapid assessment of coral, fish, and algae using the AGRRA Protocol. NOAA/National Ocean Service/Marine Sanctuaries Division, (Marine Sanctuaries Conservation Series).
- Paul, M.A., Barras, B.F., 1998. A geotechnical correction for post-depositional sediment compression: examples from the Forth valley, Scotland. *Journal of Quaternary Science* 13, 171–176.
- Peltier, W., 2009. Closure of the budget of global sea level rise over the GRACE era: the importance and magnitudes of the required corrections for global glacial isostatic adjustment. *Quaternary Science Reviews* 28, 1658–1674.
- Peltier, W., Fairbanks, R., 2006. Global glacial ice volume and Last Glacial Maximum duration from an extended Barbados sea level record. *Quaternary Science Reviews* 25, 3322–3337. doi:10.1016/j.quascirev.2006.04.010.
- Peltier, W.R., Argus, D.F., Drummond, R., 2015. Space geodesy constrains ice age terminal deglaciation: The global ICE 6G C (VM5a) model. *Journal of Geophysical Research: Solid Earth* 120, 450–487.
- Perry, C., Hepburn, L.J., 2008. Syn-depositional alteration of coral reef framework through bioerosion, encrustation and cementation: Taphonomic signatures of reef accretion and reef depositional events. *Earth-Science Reviews* 86, 106–144.
- Philibosian, B., Sieh, K., Avouac, J.P., Natawidjaja, D.H., Chiang, H.W., Wu, C.C., Perfettini, H., Shen, C.C., Daryono, M.R., Suwargadi, B.W., 2014. Rupture and variable coupling behavior of the mentawai segment of the sunda megathrust during the supercycle culmination of 1797 to 1833. *Journal of Geophysical Research: Solid Earth* 119, 7258–7287.
- Piecuch, C.G., Huybers, P., Tingley, M.P., 2017. Comparison of full and empirical Bayes approaches for inferring sea-level changes from tide-gauge data. *Journal of Geophysical Research: Oceans* 122, 2243–2258.
- Piecuch, C.G., Quinn, K.J., Ponte, R.M., 2013. Satellite-derived interannual ocean bottom pressure variability and its relation to sea level. *Geophysical Research Letters* 18, 1146–1163.
- van de Plassche, O., 1986. Sea-level research: a manual for the collection and evaluation of data. Geobooks, Norwich.

- Polach, H. (Ed.), 1976. Radiocarbon dating as a research tool in archaeology - hopes and limitations, symposium on scientific methods of research in the study of ancient Chinese Bronzes and South East Asian metal and other archaeological artifacts., Australian National University.
- Precht, W.F., Miller, S.L., 2007. Geological Approaches to Coral Reef Ecology. Springer New York. chapter Ecological Shifts along the Florida Reef Tract: The Past as a Key to the Future.
- PSMSL, 2017. Tide Gauge Data, in: Permanent Service for Mean Sea Level (PSMSL). URL: <http://www.psmsl.org/data/obtaining/>.
- Pugh, D., 1987. Tides, surges and mean sea-level: a handbook for engineers and scientists. Wiley, Chichester.
- Quinlan, G., Beaumont, C., 1981. A comparison of observed and theoretical postglacial relative sea level in Atlantic Canada. Canadian Journal of Earth Science 18, 1146–1163.
- Ramsey, C.B., 2008. Deposition models for chronological records. Quaternary Science Reviews 27, 42–60.
- Rasmussen, C.E., Williams, C.K.I., 2006. Gaussian Processes for Machine Learning. MIT Press.
- Ray, R.D., Douglas, B.C., 2011. Experiments in reconstructing twentieth-century sea levels. Progress in Oceanography 91, 496–515. doi:10.1016/j.pocean.2011.07.021.
- Reich, C.D., Halley, R.B., Hickey, T., Swarzenski, P., 2006. Groundwater characterization and assesment of contaminants in marine areas of Biscayne National Park. U.S. Geological Survey Technical Report 289.
- Reich, C.D., Hickey, T.D., DeLong, K.L., Poore, R.Z., Brock, J., 2009. Holocene core logs and site statistics for modern patch-reef cores: Biscayne National Park, Florida. U.S. Geological Survey Open-File Report 1246.
- Reich, C.D., Streuebert, M., Dwyer, B., Godbout, M., Muslic, A., Umberger, D., 2012. St. Petersburg Coastal and Marine Science Center's core archive portal. U.S. Geological Survey Data Series 626.
- Reimer, P., Baillie, M., Bard, E., Bayliss, A., Beck, J., Blackwell, P., Ramsey, C., Buck, C., Burr, G., Edwards, R., Friedrich, M., Grootes, P., Guilderson, T., Hajdas, I., Heaton, T., Hogg, A., Hughen, K., Kaiser, K., Kromer, B., McCorman, F., Manning, S., Reimer, R., Richards, D., Southon, J., Talamo, S., Turney, C., van der Plicht, J., Weyhenmeyer, C., 2009. IntCal09 and Marine09 Radiocarbon Age Calibration Curves, 0-50,000 Years cal BP. Radiocarbon 51, 1111–1150.
- Reimer, P., Bard, E., Bayliss, A., Beck, J., Blackwell, P., Ramsey, C., Buck, C., Cheng, H., Edwards, R., Friedrich, M., Grootes, P., Guilderson, T., Hafliadason, H., Hajdas, I., Hatté, C., Heaton, T., Hoffmann,

- D., Hogg, A., Hughen, K., Kaiser, K., Kromer, B., Manning, S., Niu, M., Reimer, R., Richards, D., Scott, E., Southon, J., Staff, R., Turney, C., van der Plicht, J., 2013. IntCal13 and Marine13 radiocarbon age calibration curves 0–50,000 years BP. *Radiocarbon* 55, 1869–1887.
- Renema, W., Pandolfi, J.M., Kiessling, W., Bosellini, F.R., Klaus, J.S., Korpanty, C., Rosen, B.R., Santodomingo, N., Wallace, C.C., Webster, J.M., Johnson, K.G., 2016. Are coral reefs victims of their own past success? *Science Advances* 2. doi:10.1126/sciadv.1500850.
- Robbin, D., 1984. *Environments of South Florida: Present and Past*. Miami Geol Soc.. chapter A New Holocene sea level curve for the upper Florida Keys and Florida reef tract. pp. 437–458.
- Rohling, E.J., Grant, K., Hemleben, C., Siddall, M., Hoogakker, B.A.A., Bolshaw, M., Kucera, M., 2008. High rates of sea-level rise during the last interglacial period. *Nature Geoscience* 1, 38–42.
- Rovere, A., Stocchi, P., Vacchi, M., 2016. Eustatic and Relative Sea Level Changes. *Current Climate Change Reports* 2, 221–231.
- Rye, C.D., Naveira Garbato, A.C., Holland, P.R., Meredith, M.P., George Nurser, A.J., Hughes, C.W., 2014. Rapid sea-level rise along the Antarctic margins in response to increased glacial discharge. *Nature Geoscience* 7, 732–735.
- Schwartz, M.L. (Ed.), 2005. *Encyclopedia of Coastal Sciences*. Springer.
- Scoffin, T.P., Stoddart, D., Rosen, B., 1978. The nature and significance of microatolls. *Philos Trans R Soc Lond B Biol Sci* 284, 99–122.
- Shennan, I., 2015. *Handbook of Sea-Level Research*. John Wiley & Sons, Ltd. chapter Handbook of sea-level research: framing research questions.
- Shennan, I., Horton, B., 2002. Holocene land-and sea-level changes in Great Britain. *Journal of Quaternary Science* 17, 511–526.
- Shennan, I., Lambeck, K., Horton, B., Innes, J., Lloyd, J., McArthur, J., Rutherford, M., 2000. Holocene isostasy and relative sea-level changes on the east coast of England. *Geological Society, London, Special Publications* 166, 275–298.
- Shennan, I., Long, A.J., Rutherford, M.M., Green, F.M., Innes, J.B., Lloyd, J.M., Zong, Y., Walker, K.J., 1996. Tidal marsh stratigraphy, sea-level change and large earthquakes, i: a 5000 year record in washington, U.S.A. *Quaternary Science Reviews* 15, 1023–1059.

- Shennan, I., Milne, G., Bradley, S., 2012. Late Holocene vertical land motion and relative sea-level changes: lessons from the British Isles. *Journal of Quaternary Science* 27, 64–70.
- Shennan, I., Peltier, W.R., Drummond, R., Horton, B., 2002. Global to local scale parameters determining relative sea-level changes and the post-glacial isostatic adjustment of Great Britain. *Quaternary Science Reviews* 21, 397–408.
- Shennan, I., Woodworth, P.L., 1992. A comparison of late Holocene and twentieth-century sea-level trends from the UK and North Sea region. *Geophysical Journal International* 109, 96–105.
- Shinn, E.A., 1980. Geologic history of Grecian Rocks, Key Largo coral reef marine sanctuary. *Bulletin of Marine Science* 30, 646–656.
- Shinn, E.A., Hudson, J.H., Halley, R.B., Lidz, B.H., 1977. Topographic control and accumulation rate of some Holocene coral reefs: South Florida and Dry Tortugas, in: 3rd International Coral Reef Symposium, pp. 1–7.
- Shinn, E.A., Hudson, J.H., Robbin, D., Lidz, B.H., 1981. Spurs and grooves revisited: construction versus erosion Looe Key reef, Florida, in: Fourth International Coral Reef Symposium, Manila, pp. 475–483.
- Shinn, E.A., Reich, C.D., Hickey, T.D., Lidz, B.H., 2003. Staghorn tempestites in the Florida Keys 22, 91–97.
- Simons, W.J.F., Socquet, A., Vigny, C., Ambrosius, B.A.C., Haji Abu, S., Promthong, C., Subarya, C., Sarsito, D.A., Matheussen, S., Morgan, P., Spakman, W., 2007. A decade of gps in southeast asia: Resolving sundaland motion and boundaries. *Journal of Geophysical Research: Solid Earth* 112. doi:10.1029/2005JB003868.
- Smith, D., Harrison, S., Firth, C., Jordan, J., 2011. The early Holocene sea level rise. *Quaternary Science Reviews* 30, 1846–1860.
- Smith, T.B., Blondeau, J., Nemeth, R.S., Pittman, S.J., Calnan, J.M., Kadison, E., Gass, J., 2010. Benthic structure and cryptic mortality in a Caribbean mesophotic coral reef bank system, the Hind Bank Marine Conservation District, U.S. Virgin Islands. *Coral Reefs* 29, 289–308.
- Smith, T.M., Reynolds, R.W., Livezey, R.E., Stokes, D.C., 1996. Reconstruction of Historical Sea Surface Temperatures Using Empirical Orthogonal Functions. *Journal of Climate* 9, 1403–1420.
- Smithers, S.G., Woodroffe, C.D., 2000. Microatolls as sea-level indicators on a mid-ocean atoll. *Marine Geology* 168, 61–78.

- Southon, J., Kashgarian, M., Fontugne, M., Metivier, B., Yim, W., 2002. Marine reservoir corrections for the Indian Ocean and Southeast Asia. *Radiocarbon* 44, 167–180.
- Stammer, D., Cazenave, A., Ponte, R.M., Tamisiea, M.E., 2013. Causes for Contemporary Regional Sea Level Changes. *Annual Review of Marine Science* 5, 21–46.
- Stanford, J., Hemingway, R., Rohling, E., Challenor, P., Medina-Elizalde, M., Lester, A., 2011. Sea-level probability for the last deglaciation: A statistical analysis of far-field records. *Global and Planetary Change* 79, 193–203.
- Stathakopoulos, A., Riegl, B.M., 2014. Accretion history of mid-Holocene reefs from the southeast Florida continental reef tract, USA. *Coral Reefs* 34, 173–187.
- Stout, S., Spackman, W., 1989. Notes on the compaction of a Florida peat and the Brandon lignite as deduced from the study of compressed wood. *International Journal of Coal Geology* 11, 247–256.
- Strassburg, M.W., Hamlington, B.D., Leben, R.R., Manurung, P., Lumban Gaol, J., Nababan, B., Vignudelli, S., Kim, K.Y., 2015. Sea level trends in Southeast Asian seas. *Climate of the Past* 11, 743–750.
- Stuiver, M., Polach, H., 1977. Reporting of ^{14}C data - discussion. *Radiocarbon* 19, 355–363.
- Syvitski, J.P.M., Kettner, A.J., Overeem, I., Hutton, E.W.H., Hannon, M.T., Brakenridge, G.R., Day, J., Vörösmarty, C., Saito, Y., Giosan, L., Nicholls, R.J., 2009. Sinking deltas due to human activities. *Nature Geoscience* 2. doi:10.1038/ngeo629.
- Tamisiea, M.E., Mitrovica, J.X., 2011. The Moving Boundaries of Sea Level Change: Understanding the Origins of Geographic Variability. *Oceanography* 24, 24–39. doi:10.1111/j.1365-246X.2011.05116.x.
- Taylor, F.W., Frohlich, C., Lecolle, J., Strecker, M., 1987. Analysis of partially emerged corals and reef terraces in the central vanuatu arc: Comparison of contemporary coseismic and nonseismic with quaternary vertical movements. *Journal of Geophysical Research: Solid Earth* 92, 4905–4933.
- Tingley, M.P., Craigmile, P.F., Haran, M., Li, B., Mannshardt, E., Rajaratnam, B., 2012. Piecing together the past: statistical insights into paleoclimatic reconstructions. *Quaternary Science Reviews* 35, 1–22.
- Tolwinski-Ward, S.E., Evans, M.N., Hughes, M.K., Anchukaitis, K.J., 2011. An efficient forward model of the climate controls on interannual variation in tree-ring width. *Climate Dynamics* 36, 2419–2439.
- Törnqvist, T.E., Bick, S.J., González, J.L., van der Borg, K., de Jong, A.F.M., 2004. Tracking the sea-level signature of the 8.2 ka cooling event: New constraints from the Mississippi Delta. *Geophysical Research Letters* 31. doi:10.1130/b2525478.1.

- Törnqvist, T.E., González, J.L., Newsom, L.A., Borg, K., Jong, A.F., 2002. Reconstructing “background” Rates of sealevel rise as a tool for forecasting coastal wetland loss, Mississippi Delta. *Eos, Transactions American Geophysical Union* 83, 525–531.
- Törnqvist, T.E., Rosenheim, B.E., Hu, P., Fernandez, A.B., 2015. Handbook of Sea-Level Research. John Wiley & Sons, Ltd. chapter Dating Methods: Radiocarbon dating and calibration. pp. 347–360. doi:10.1002/9781118452547.
- Törnqvist, T.E., Wallace, D.J., Storms, J.E.A., Wallinga, J., van Dam, R.L., Blaauw, M., Derksen, M.S., Klerks, C.J.W., Meijneken, C., Snijders, E.M.A., 2008. Mississippi Delta subsidence primarily caused by compaction of Holocene strata. *Nature Geoscience* 1, 173–176.
- Toscano, M.A., Macintyre, I.G., 2003. Corrected western Atlantic sea-level curve for the last 11,000 years based on calibrated ¹⁴C dates from *Acropora palmata* framework and intertidal mangrove peat. *Coral Reefs* 22, 257–270. doi:10.1007/s00338-003-0315-4.
- Toscano, M.A., Peltier, W.R., Drummond, R., 2011. Ice-5g and ice-6g models of postglacial relative sea-level history applied to the holocene coral reef record of northeastern st croix, u.s.v.i.: investigating the influence of rotational feedback on gia processes at tropical latitudes. *Quaternary Science Reviews* 30, 3032–3042. doi:10.1016/j.quascirev.2011.07.018.
- Toth, L.T., Cheng, H., Edwards, R.L., Ashe, E.L., Richey, J.N., 2017. Millennial-scale variability in the local radiocarbon reservoir age of south Florida during the Holocene. *Quaternary Geochronology* 42, 130–143.
- Toth, L.T., Kuffner, I.B., Edwards, R.L., 2015. A new record of the late Pleistocene coral *Pocillopora palmata* from the Dry Tortugas, Florida, USA. *PALAIOS* 30, 827–835.
- Uehara, K., Scourse, J.D., Horsburgh, K.J., Lambeck, K., Purcell, A., 2006. Tidal evolution of the northwest European shelf seas from the Last Glacial Maximum to present. *Journal of Geophysical Research* 111. doi:10.1029/2006JC003531.
- Vacchi, M., Engelhart, S.E., Nikitina, D., Ashe, E.L., Peltier, W.R., Roy, K., Kopp, R.E., Horton, B.P., in review. Postglacial relative sea-level histories along the Northeastern Canadian coastline. *Quaternary Science Reviews* .
- Vacchi, M., Rovere, A., Zouros, N., Desruelles, S., Caron, V., Firpo, M., 2012. Spatial distribution of sea-level markers on Lesbos Island (NE Aegean Sea): Evidence of differential relative sea-level changes and the neotectonic implications. *Geomorphology* 159-160, 50–62.

- Van Veen, J., 1945. Bestaat er een geologische bodemdaling te Amsterdam sedert 1700? *Tijdschrift Koninklijk Nederlandsch Aardrijkskundig Genootschap* 1.
- Vane, C.H., Kim, A.W., Moss-Hayes, V., Snape, C.E., Diaz, M.C., Khan, N.S., Engelhart, S.E., Horton, B.P., 2013. Degradation of mangrove tissues by arboreal termites (*Nasutitermes acajutlae*) and their role in the mangrove C cycle (Puerto Rico): Chemical characterization and organic matter provenance using bulk ^{13}C , C/N, alkaline CuO oxidation-GC/MS, and solid-state ^{13}C NMR. *Geochemistry, Geophysics, Geosystems* 14, 3176–3191. doi:10.1002/ggge.20194.
- Varekamp, J., Thomas, E., Van de Plassche, O., 1992. Relative sea-level rise and climate change over the last 1500 years. *Terra Nova* 4, 293–304.
- Visser, H., Molenaar, J., 1988. Kalman Filter Analysis in Dendroclimatology. *Biometrics* 44, 929–940.
- Walker, M., Johnsen, S., Rasmussen, S.O., Popp, T., Steffensen, J.P., Gibbard, P., Hoek, W., Lowe, J., Andrews, J., Björck, S., Cwynar, L.C., Hughen, K., Kershaw, P., Kromer, B., Litt, T., Lowe, D.J., Nakagawa, T., Newnham, R., Schwander, J., 2009. Formal definition and dating of the gssp (global stratotype section and point) for the base of the holocene using the greenland ngrip ice core, and selected auxiliary records. *Journal of Quaternary Science* 24, 3–17.
- White, N.J., Haigh, I.D., Church, J.A., Koen, T., Watson, C.S., Pritchard, T.R., Watson, P.J., Burgette, R.J., McInnes, K.L., You, Z.J., Zhang, X., Tregoning, P., 2014. Australian sea levels—Trends, regional variability and influencing factors. *Earth-Science Reviews* 136, 155–174.
- Widlansky, M.J., Timmermann, A., Cai, W., 2015. Future extreme sea level seesaws in the tropical Pacific. *Science Advances* 1. doi:10.1126/sciadv.1500560.
- Wilks, S.S., 1938. The large-sample distribution of the likelihood ratio for testing composite hypotheses. *Annals of Mathematical Statistics* 9, 60–62.
- Woodroffe, S.A., Horton, B.P., 2005. Holocene sea-level changes in the Indo-Pacific. *Journal of Asian Earth Sciences* 25, 29–43. doi:10.1016/j.jseaes.2004.01.009.
- Woodroffe, S.A., Long, A.J., Punwong, P., Selby, K., Bryant, C.L., Marchant, R., 2015. Radiocarbon dating of mangrove sediments to constrain Holocene relative sea-level change on Zanzibar in the southwest Indian Ocean. *The Holocene* 25, 820–831. doi:10.1177/0959683615571422.
- Woodworth, P.L., 1999. High waters at Liverpool since 1768: the UK's longest sea level record. *Geophysical Research Letters* 26, 1589–1592.

- Yokoyama, Y., Lambeck, K., De Dekkar, P., Johnston, P., Fifield, L.K., 2000. Timing of Last Glacial Maximum from observed sea level minima. *Nature* 406, 713–716.
- Yu, K., Hua, Q., Zhao, J.x., Hodge, E., Fink, D., Barbetti, M., 2010. Holocene marine ^{14}C reservoir age variability: Evidence from ^{230}Th -dated corals in the South China Sea. *Paleoceanography* 25. doi:10.1029/2009PA001831.
- Yu, K.F., Zhao, J.X., Done, T., Chen, T.G., 2009. Microatoll record for large century-scale sea-level fluctuations in the mid-Holocene. *Quaternary Research* 71, 354–360.
- Zachariasen, J., Sieh, K., Taylor, F.W., Hantoro, W.S., 2000. Modern Vertical Deformation above the Sumatran Subduction Zone: Paleogeodetic Insights from Coral Microatolls. *Bulletin of the Seismological Society of America* 90, 897–913.
- Zhang, X., Church, J.A., 2012. Sea level trends, interannual and decadal variability in the Pacific Ocean. *Geophysical Research Letters* 39.
- Zong, Y., 2004. Mid-Holocene sea-level highstand along the Southeast Coast of China. *Quaternary International* 117, 55–67. doi:10.1016/S1040-6182(03)00116-2.
- Zong, Y., Horton, B.P., 1999. Diatom-based tidal-level transfer functions as an aid in reconstructing Quaternary history of sea-level movements in the UK. *Journal of Quaternary Science* 14, 1099–1417.

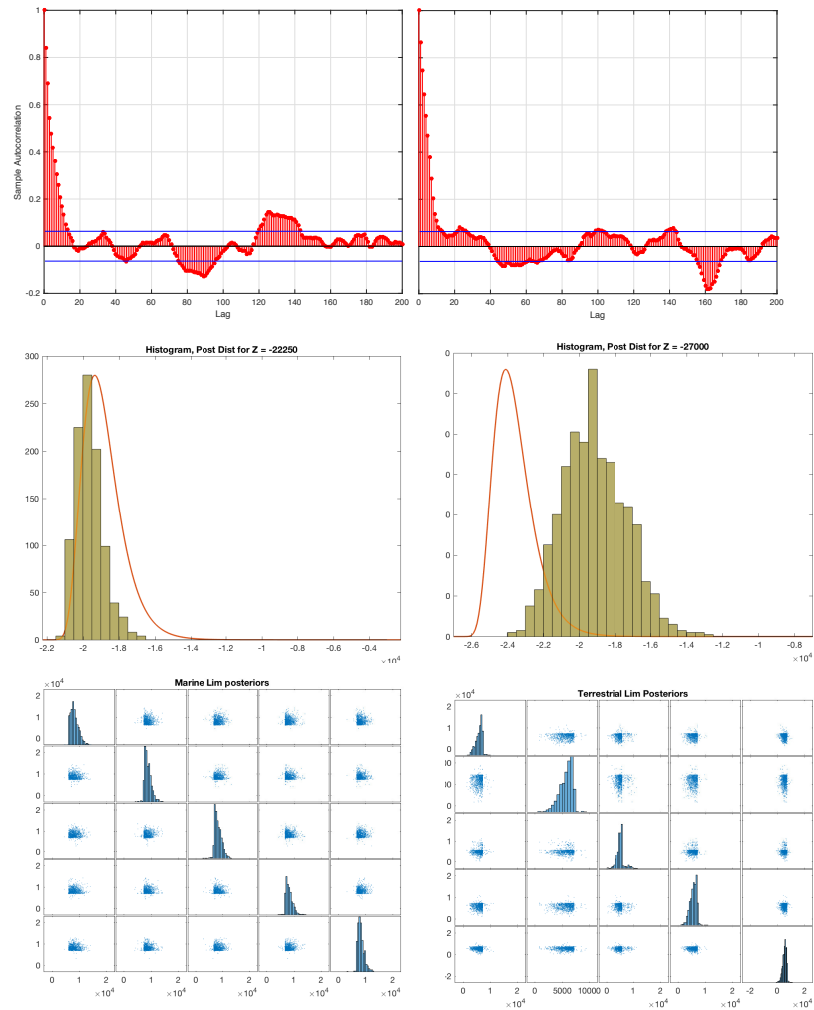


Figure B.8: Diagnostics: Some examples of monitoring convergence and autocorrelation, in addition to using a form of adaptive MH, evaluating and tuning the jump size for optimal acceptance ratios ($\sim 25\%$). The first row of figures are autocorrelations, which lead us to choose a thinning of every 40th sample. The second row of figures demonstrates the posterior distributions of a few of the log-normally distributed data, where other data may have influenced positioning, but where the original log-normal likelihood (independent of the other data) is shown in red. The third row is posterior distributions of marine- and terrestrial- limiting data and their correlations with one another.

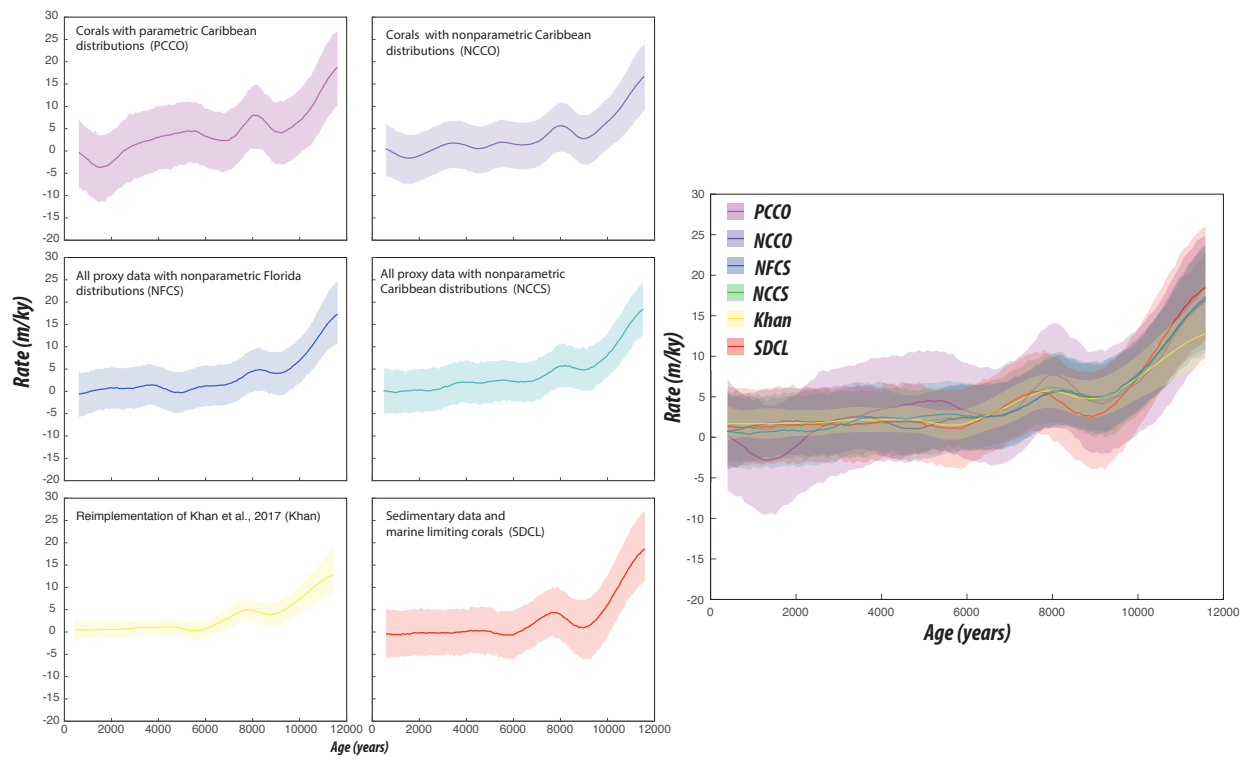


Figure B.9: Rates for models PCCO, NCCO, NFCS, NCCS, Khan, and SDCL.